Solar tracking of perovskite-silicon tandem PV modules under real-world conditions

Orestis Chatzilampos

TU Delft

DELFT UNIVERSITY OF TECHNOLOGY

FACULTY OF ELECTRICAL ENGINEERING, MATHEMATICS AND COMPUTER SCIENCE

Solar tracking of perovskite-silicon tandem PV modules under real-world conditions

by

Orestis Chatzilampos

Student number: 5569990

In partial fulfillment of the requirements for the degree of

Master of Science
Sustainable Energy Technology

To be defended publicly on Wednesday, October 4th, 2023 at 13:00

Thesis Committee
Prof.Dr.ir Olindo Isabella (Chair)
Dr.ir Rudi Santbergen (Supervisor)
Dr. J.L. (Jochen) Cremer (External member)
Youri Blom (Daily supervisor)

An electronic version of this report is available at `http://repository.tudelft.nl/`.

TU Delft

PVMD
Delft University of Technology

Abstract

Increasing the energy yield per unit area of Photovoltaic (PV) modules is one of the main challenges the PV technology is currently facing. In search of ways to address this issue, solar tracking systems are a favorable solution, which according to literature can enhance the energy yield by up to 45%. Another way is to opt for high-efficiency solar cells. Tandem cells have emerged as a promising technology, achieving efficiencies of over 30%. The integration of these tandem cells with sun-tracking techniques suggests high-performing solar modules.

The present work develops a solar tracking model to simulate the performance of tracking PV systems equipped with tandem modules. The model will be incorporated into the PVMD toolbox, a PV modeling software developed within the PVMD group. This software can predict the energy yield of PV systems using self-consistent models for each aspect of the energy conversion.

The current version of the toolbox makes it impractical to include solar tracking due to the time-consuming nature of ray tracing used to compute the irradiance. Ray tracing generates sensitivity values that illustrate how sensitive is the module to incoming irradiance from any direction in the skydome. Initially, this work focuses on substituting ray tracing with an alternative faster approach to express sensitivity based on view factors. The view factor and ray tracing method are compared with respect to computational time and extent of agreement. It was found that the view factor can significantly reduce the computational time from over 12 minutes, as required in ray tracing, to a few milliseconds for a single module orientation. Additionally, the view factor method generates sensitivity values closely matching those from ray tracing. For instance, a mean RMSE of 1.2% between the two methods is achieved, for an albedo of 0.2 and module tilt of 30 degrees.

Sun tracking aims to locate the module orientation that maximizes the in-plane irradiance. Directly calculating the irradiance for every orientation to identify the optimal, is not a viable option, as it requires substantial time. Thus, sun tracking was expressed as an optimization problem and algorithms were employed to address it. Based on the prevailing sky conditions three optimization case studies were defined on an hourly basis: sunny, cloudy, and intermediate hours. Multiple algorithms were compared across the three cases with selected criteria the convergence to the optimum and runtime. Matlab's surrogate solver and an author-developed algorithm were selected, as a satisfying solution, compromising those two criteria.

Finally, energy yield simulations were performed on perovskite-silicon tandem modules mounted on a dual-axis tracking system. Four locations were selected, representing different real-world conditions: Stockholm, Athens, Bombay and Bogota. Results show the module's tilt dynamic adaptability to sky conditions: increasing nearly to the sun's zenith when direct light dominates, and lowering when diffuse light is prevalent. Furthermore, the seasonal fluctuations of the energy gain of tracking systems are explored, with locations further from the equator such as Stockholm exhibiting the highest variability of 19% in winter to 36.9% in summer. In addition, the annual energy gained among the locations was found to span between 24.8% (Bogota) and 34.1% (Bombay). An important finding is the direct proportionality in gains from absorbed irradiance to DC and AC yields, illustrating a 1:1:1 ratio. Then, the effect of tracking technology on mismatch losses of tandem modules was examined. Results indicated that tracking has little impact on both the current and power mismatch. For example, the power mismatch losses slightly increased from 1.10-1.46% in static PV systems to 1.29-1.77% for tracking topologies in the locations examined. Moreover, the tandem's annual energy gain is compared to silicon heterojunction modules. The analysis showed similar gains across locations for both cell technologies.

Acknowledgements

Before you start reading my work, thank you for trying so. For those who make it until the end, I hope you enjoy it. I've spent nine months on a topic that I proposed myself but carried out with the help of numerous people. So, let's start counting them down.

I am grateful to Dr.ir. Rudi Santbergen, for his guidance, enormous and good feedback, encouragement, knowledge, and insights. His critical comments on parts of my work helped me a lot to obtain a critical attitude on my results, and also discover things that I hadn't thought of. Rudi once told me that thesis is not a sprint but looks more like a marathon that requires stamina to finish, but you should also take care of yourself in the run. I kept this word, for more marathons to come.

I especially want to thank Youri Blom, with whom I worked closest all these months, for multiple reasons. First, for him being always there to answer my questions, discuss new ideas, give valuable feedback, and push me to think out of the box and develop my own methods. Apart from the technical stuff, he was there to help me when results didn't make sense or algorithms didn't work with his good, optimistic words, giving me the courage to continue. Without him, things would have been harder. Well, I consider myself not an easy person to handle, so thanks Youri! Lastly, I want to thank Prof.dr.ir. Olindo Isabella and Dr. Jochen Cremer for taking the time to assess my work.

The end of my thesis, brings an end to my student life in Delft. I have a lot of memories from the last two years. Yes, I and any other student spend endless hours studying, but it wasn't just that. All these memories wouldn't mean something if were not shared with friends. I am grateful to all my friends for their support during these two years and all the experiences we've shared.

To my family, thanks for your enormous support all these years. Thanks for being next to me, and helping me find the light at the end of the tunnel when I couldn't see it.

Lastly, a message to Xanthippi: You endured the most all these years. I shared with you my anxiety, happiness, problems, and sadness. You have always been present for me to calm me down, discuss, and overcome the burdens. It's hard to put it in words at the moment, but thank you for everything you've done for me!

Orestis Chatzilampos,

Delft, September 2023

Contents

Abstract ii

Acknowledgements iv

List of Figures viii

List of Tables x

Nomenclature xi

1 Introduction 1
1.1 Background . . . 1
1.2 The perovskite-silicon tandem cells . . . 2
1.2.1 Tandem cells working principle: the perovskite-silicon advantage . . . 2
1.2.2 Tandem cell architecture . . . 3
1.2.3 EQE of a perovskite-silicon tandem cell . . . 4
1.3 Solar tracking technologies . . . 5
1.3.1 Based on the control strategy . . . 5
1.3.2 Based on the nature of motion . . . 5
1.3.3 Based on the motion's degrees of freedom . . . 6
1.4 Solar tracking and cell technologies . . . 7
1.5 The PVMD Toolbox . . . 8
1.5.1 PVMD Toolbox structure . . . 8
1.5.2 PVMD Toolbox limitations . . . 12
1.6 Research gap and thesis objectives . . . 13
1.6.1 Research Gap - motivation . . . 13
1.6.2 Thesis objectives . . . 13
1.7 Thesis outline . . . 14

2 Irradiance Calculation: A View Factor Model 15
2.1 The current irradiance model in the PVMD toolbox . . . 15
2.1.1 Limitations of ray tracing . . . 16
2.2 The proposed simulation approach . . . 16
2.3 New approach on sensitivity: a view factor model . . . 17
2.3.1 Sensitivity of the direct/diffuse irradiance . . . 17
2.3.2 Sensitivity of the reflected irradiance . . . 19
2.3.3 Sensitivity of the total irradiance . . . 20
2.4 Comparative analysis: view factor against ray tracing . . . 21
2.4.1 Computational time comparison . . . 21
2.4.2 Results comparison . . . 21
2.4.3 Effect of albedo and module tilt angle . . . 25
2.5 Conclusion . . . 27

3 Maximizing the Absorbed Irradiance: An Optimization Model 29
3.1 Problem formulation . . . 29
3.2 Optimization case studies . . . 29
3.2.1 Sunny hour - clear maximum . . . 30
3.2.2 Overcast hour - not clear maximum . . . 31
3.2.3 Partially overcast hour - intermediate cases . . . 32
3.3 Optimization algorithms . . . 32

3.3.1 Surrogate optimization . . . 33
3.3.2 Cross method . . . 34
3.4 Comparative algorithm analysis over an annual simulation . . . 36
3.5 Solar tracker self-consumption . . . 36
3.6 Control strategy . . . 37
3.7 Conclusion . . . 38

4 Solar Tracking Under Real-World Conditions 39
4.1 Input for toolbox simulations . . . 39
4.1.1 Modelled solar cell specifications . . . 39
4.1.2 Toolbox models input parameters . . . 40
4.2 Locations selection . . . 41
4.3 Results: daily PV system performance . . . 42
4.3.1 Daily optimal orientations . . . 42
4.3.2 Daily AC yield . . . 44
4.4 Results: seasonal PV system performance . . . 46
4.5 Results: annual PV system performance . . . 47
4.5.1 Annual energy yield . . . 47
4.5.2 Effect of tracking on cell temperature . . . 48
4.5.3 Annual irradiance gain - DC Gain - AC gain ratio . . . 49
4.5.4 Effect of tracking on mismatch losses . . . 51
4.6 Comparison with the SHJ modules annual energy gain . . . 52
4.7 Conclusion . . . 54

5 Conclusions and Recommendations 55
5.1 Conclusions . . . 55
5.2 Recommendations . . . 56
5.2.1 The PVMD Toolbox . . . 57
5.2.2 The designed model . . . 57
5.2.3 The performed simulations . . . 59

A DC Motor Selection 61

B Global Climate Classsifcation 62

C PV system performance 63
C.1 Daily AC yield results . . . 63
C.2 Monthly AC yield results . . . 64
C.3 Energy gain ratio . . . 65
C.4 Hourly optimum tilt angle histogram . . . 66
C.5 Fill factor gain effect . . . 67

D Spectral Irradiance 68

List of Figures

1.1 Cumulative installed PV power by region as obtained by [4]. . . . 2
1.2 Illustration of perovskite-silicon tandem cells configurations. . . . 3
1.3 Representation of pn-np and np-np 3T IBC tandem cell configurations as proposed by [19]. . . 4
1.4 Examples of the EQE of a Perovskite-Silicon Tandem (PST) cell, for an AOI: (a) of 45°, (b) of 81°. 4
1.5 PV tracking technologies classifiacation 5
1.6 Tracking configurations on the basis of the motion's degrees of freedom. . . . 6
1.7 Selective results from the work of Babics et al. [43] 7
1.8 Selective results from the work of Horantner and Snaith [42]. . . . 8
1.9 Mounting illustration of a module facing south with tilt 27°. . . . 9
1.10 Sensitivity map for calculated for individual cells (Ray-tracing for 25000 rays). . . . 9
1.11 Schematic overview of the PVMD toolbox structure. . . . 11
1.12 Spectral composition approach applied in the toolbox 12

2.1 Modification of the toolbox structure in relation to the current version. . . . 17
2.2 Angle of Incidence between the incoming light from a vertex and the module's surface normal. 18
2.3 Vertices that contribute or not in the $S_{Dir/Dif}$ calculation. . . . 19
2.4 Assumptions for the $S_{reflected}$ calculation of a vertex A in the skydome. . . . 20
2.5 Schematic illustration of the S_{VF} calculation. . . . 21
2.6 Sensitivity values against the wavelength of multiple vertices computed with ray tracing and view factor method. . . . 22
2.7 RMSE values of the important vertices for the three layers for the same example discussed in Figure 2.6. . . . 24
2.8 Illustration of light coming from high-and low-altitude vertices in the skydome 25
2.9 Effect of the module tilt in the mean Root Mean Square Error (RMSE) for sensitivity values calculated with the two methods 25
2.10 Effect of albedo in the mean RMSE for sensitivity values calculated with the two methods. . . . 26

3.1 Absorbed irradiance profile in Delft July 1st. . . . 30
3.2 Absorbed irradiance profile in a sunny hour in Delft. . . . 31
3.3 Absorbed irradiance profile in an overcast hour in Delft. . . . 31
3.4 Surrogate optimization: phase visualization graphs. . . . 33
3.5 Example of the cross method convergence to the optimum. . . . 34
3.6 Flowchart of the control strategy of the optimization process. . . . 38

4.1 Sun paths of the four locations 41
4.2 Optimal azimuth and tilt angle of 2T-tandem module for a day in Athens. . . . 42
4.3 Optimal tilt angles and irradiance components of a 2T tandem module for a partly cloudy day in Athens (January 6). . . . 43
4.4 Optimal tilt angles and irradiance components of a 2T tandem module for a day with variable sky conditions in Athens (May 13). . . . 44
4.5 Comparison of the hourly AC yield and energy gain for the fixed and tracking PV system for the sunniest day in Athens (May 26). . . . 44
4.6 Seasonal AC gain for the two tracking systems in the four locations 46
4.7 Annual AC yield produced for a 2T tandem module in the four locations. . . . 47
4.8 Annual weighted temperature of a 2T tandem module in the four locations for a static and tracking topology. . . . 49
4.9 Annual gain in irradiance, DC and AC yield for the 2T tandem tracking system in Athens. . . . 49
4.10 Selected results from the work of Blom et al. [73] 50
4.11 Annual AC yield for a SHJ module in the four locations 53

4.12 Annual spectral composition of the absorbed irradiance for a 2T tandem module in Athens (example location). 54

5.1 Adapted cross method search pattern for single-axis tracking 60

B.1 Climate zone classification map of the Koppen Geiger Photovoltaic (KGPV) scheme [66]. 62

C.1 Comparison of the hourly energy output and gain for the fixed and tracking 2T tandem PV system across the locations 63
C.2 Monthly AC yield of the 2T tandem PV system in the four locations 64
C.3 Energy gain ratio of irradiance-DC yield-AC yield for the tandem tracking PV system 65
C.4 Optimum tilt angle histogram of the tandem tracking PV system 66
C.5 The FF gain effect explanation 67

D.1 Spectral distribution of the irradiance components [76]. 68

List of Tables

2.1 Average computational time of ray tracing for various tilts on a PSTC. 16
2.2 RMSE values per layer for the vertices discusses in Figure 2.6. 23
2.3 Mean RMSE values of all vertices for the three layers of a single module orientation. 24

3.1 Matlab's built-in optimization algorithms qualitative comparison. 32
3.2 Performance of the surrogate optimization for the three hour-cases. 34
3.3 Performance of the cross method for the three hour-cases 35
3.4 Annual simulation comparison: cross method against surrogate optimization. 36

4.1 2T perovskite-silicon tandem cell specifications 40
4.2 Input specifications for the Toolbox models 40
4.3 Locations data 42
4.4 Daily AC energy output of the two PV systems in Athens (Figure 4.5). 45
4.5 Annual AC gain (%) for 2T tandem module in the four locations. 47
4.6 Current and power mismatch losses 51
4.7 Single junction silicon cell specifications 52
4.8 SHJ and 2T tandem relative AC gain 53

A.1 Input parameters of the solar module used in toolbox simulations 61

Nomenclature

Acronyms

AADAT Azimuth-Altitude Dual Axis Tracker

AOI Angle of Incidence

ASA Advanced Semiconductor Analysis

CLEM Calibrated Lumped Element Model

DHI Diffuse Horizontal Irradiance

DNI Direct Normal Irradiance

EQE External Quantum Efficiency

GHI Global Horizontal Irradiance

GUI Graphical User Interface

HSAT Horizontal Single axis tracker

IBC Interdigitated Back Contacts

IEA International Energy Agency

KGPV Koppen Geiger Photovoltaic

LCOE Levelized Cost of Electricity

PST Perovskite-Silicon Tandem

PVMD Photovoltaic Material and Devices

RMSE Root Mean Square Error

SHJ Silicon Heterojunction

SM Sensitivity Map

STC Standard Test Conditions

TCO Transparent Conductive Oxide

TSAT Tilted Single Axis Tracker

TTDAT Tip-Tilt Dual Axis Tracker

VSAT Vertical Single axis tracker

Symbols

A Absorptance

A_M Module azimuth

A_v Vertex azimuth

Abs Absorbed irradiance

AOI_D Angle of incidence for direct/diffuse radiance

AOI_R Angle of incidence for ground reflected irradiance

B_i Spectrally resolved incoming irradiance

lay cell layer

$S_{Dir/Diff}$ Sensitivity related to the direct/diffuse irradiance

S_R Ray tracing sensitivity

S_{VF} View factor sensitivity

T Transmittance

R Reflectance

α_M Module altitude

α_v Vertex altitude

θ_M Module tilt

λ Wavelength

Chapter 1

Introduction

This chapter addresses the theoretical concepts associated with this study as explored during the literature review. Section 1.1 provides background information on the trends in the energy transition and photovoltaic technology. Section 1.2 introduces the perovskite-silicon tandem technology along with the tandem cell configurations. Next, the PV tracking mechanisms are discussed in Section 1.3. Bridging these two subjects, Section 1.4 highlights studies that integrate tracking systems with perovskite-silicon tandem modules. The concept of PV modeling is introduced in Section 1.5 by presenting the PVMD toolbox software. Once the research gap is determined, the thesis objectives are formulated in Section 1.6. Finally, the report structure is outlined in Section 1.7.

1.1 Background

Nowadays, the future of the energy sector is shaped worldwide by one leading trend: the energy transition, that is, the change from one fossil-based energy mix to a system relying on renewable sources. A growing number of countries that declare pledges to accomplish net zero emissions by 2050 or earlier, drive this transition. Strategic roadmaps are designed by governments to meet energy-related targets on a national level on top of international treaties such as the Paris Agreement [1]. Considering that the energy demand is projected to increase nearly 50% by 2050 compared to 2020 [2], the current global energy infrastructure has to be transformed at an unprecedented rate. However, the vast deployment of renewables should be made in a cost-effective way, ensuring the security of supply.

A player of major significance in the energy transition is photovoltaic technology. So far, the rapid development of PV technology and accumulated experience have led to low PV module prices [3]. This enabled an exponential increase in PV power installed capacity over the last decades, as depicted in Figure 1.1. According to the International Energy Agency (IEA) [4], the cumulative installed PV power reached 945.54 GWp worldwide in 2021, growing by 22% from 2020. By far the largest share is installed in the Asia-pacific region, with China being the leader, accounting for almost one-third of global cumulative capacity [4]. Although enormous progressive steps have been made in PV installation, the annual growth rate has to be increased in order to meet the net zero emissions scenario by 2050. Recent IEA's studies suggest an average annual growth of 26% in PV electricity generation for the years 2023-2030 [5]. This is translated to a cumulative installed PV capacity of around 6 TWp in 2030, following the net zero emission scenario.

For such a large-scale solar power integration to be successful, the full potential of the PV technologies should be uncovered. Enhancing solar modules' energy performance is essential as it reduces the installed capacity needed to meet the energy requirements. There are several ways to improve PV power output. This can be realized either by improving the cell's efficiency or by applying techniques that increase the amount of incoming irradiance and lead to higher PV output.

As PV implementation expands, the precise estimation of the energy output becomes equally important. PV panels are mostly tested under Standard Test Conditions (STC), which defines a standard ambient temperature, irradiance, and spectrum. However, the operational conditions are considerably different than STC and have an immense impact on the energy produced. Predicting the energy yield under real-world conditions constitutes a crucial element that can boost the commissioning rate of solar power. This task, along with enhancing module performance, represent two important challenges that the PV community is currently facing.

Given the challenges outlined, this work aims to address these issues. In the following pages, new cell

technologies are explored, as well as methods that enhance sunlight capture. Moreover, emphasis is placed on examining the energy performance of these technologies under realistic conditions.

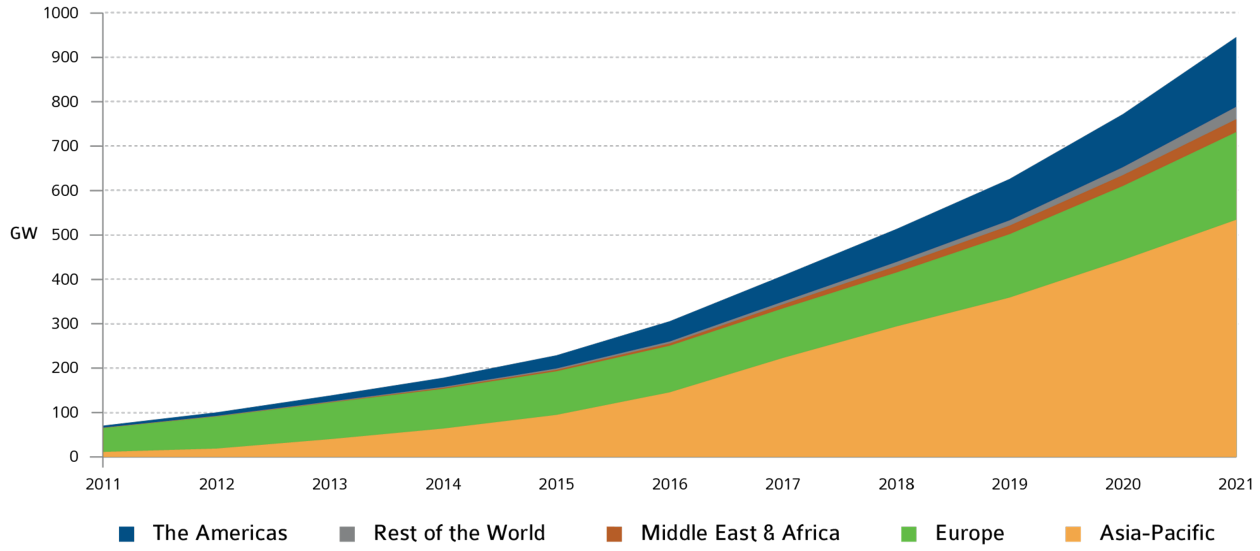

Figure 1.1: Cumulative installed PV power by region as obtained by [4].

1.2 The perovskite-silicon tandem cells

One way to enhance the energy output is by utilizing innovative cell technologies, such as Perovskite-Silicon Tandem (PST) cells, which have demonstrated high efficiencies [6]. The novel and promising nature of PST, renders this technology one of the top emerging technologies in the area.

1.2.1 Tandem cells working principle: the perovskite-silicon advantage

The theoretically limited efficiency of a single junction solar cell is determined by the Schockley-Queisser limit at 29.42% [7]. The majority of the losses are ascribed to non-absorbed photons with energy less than the bandgap and thermalized photons with energies greater than the bandgap. The most effective way to mitigate spectral mismatch losses is by combining materials with different bandgaps in a multijunction solar cell. The simplest multijunction structure consisting of two solar cells connected in series is called a tandem cell. On top, the higher bandgap material is placed so that the high-energy photons of solar irradiation are absorbed, allowing a reduction in thermalization losses. The remaining non-absorbed low-energy photons are transmitted through the top cell and absorbed by the bottom cell. Because a broad range of incident spectrum can be effectively converted into electric power, the tandem cells achieve high power conversion efficiencies. The theoretical efficiency's upper limit of a tandem with two cells is calculated at 42% [8].

A well-promising top-bottom cell pair is that of perovskite-silicon. Perovskite semiconductors are minerals with the general formula ABX_3, where X is an anion, B and A are cations. X is halogen atom or in the form of halide compound while B is usually Pb or Sn [9]. Silicon solar cells are in crystalline form.

There are multiple reasons that justify the selection of the two partners. On the one hand, the perovskite materials are characterized by properties such as high absorption coefficients, high defect tolerance, low non-radiative carrier recombination as well as an increasing performance over the recent years. [9, 10, 11]. Another key advantage is that perovskite bandgap can be easily tuned by altering the cell's composition so that its optical properties can be tailored for a specific tandem application [11]. On the other hand, crystalline Si cell is a good candidate for low bandgap cells mainly due to their bandgap suitability (1.12 eV). An additional argument is that Si, as being one of the most abundant elements on earth, has for long prevailed in the market, leading to a competitive price of c-Si solar cells for large-scale production [12]. All the benefits of the PST are being validated as their performance has exceeded 30% [6].

1.2.2 Tandem cell architecture

The perovskite-silicon tandem cells, based on their sub-cells interconnection, are categorized into three well-established configurations: two terminal (2T), four terminal (4T), and three terminal (3T) configurations. All three configurations are in demonstrated in Figure 1.2.

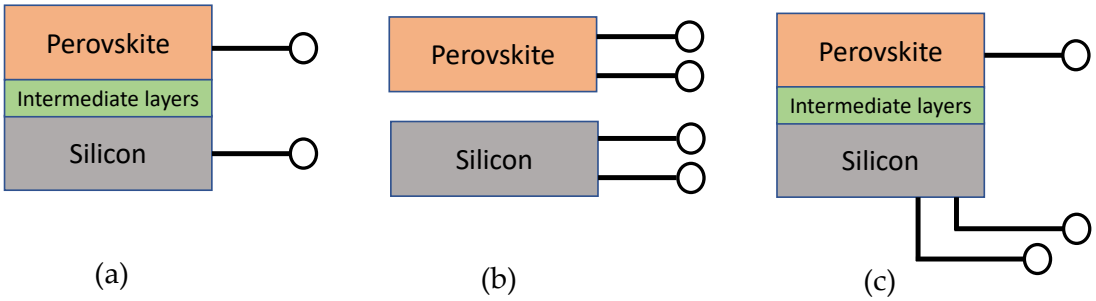

Figure 1.2: Illustration of perovskite-silicon tandem cells configurations: (a) 2 terminal, (b) 4 terminal, (c) Interdigitated back contact 3 terminal tandem solar cells.

In the 2T structure, the two sub-cells are electrically connected in series, and the tandem has two electrodes as the output of each terminal, one on each sub-cell. The incident spectrum is shared between the two cells: the perovskite top cell absorbs higher energy photons while the silicon bottom cell absorbs photons of lower energy. One advantage of 2T tandems is the ease of manufacturing process as they are monolithically fabricated. The perovskite top cell is fabricated directly on top of the silicon bottom cell [13]. In between them, a recombination contact layer is established. Another advantage is that only two Transparent Conductive Oxide (TCO) for lateral current collection are required, resulting in lower fabrication costs. However, the main drawback is that in order to operate at maximum power for the tandem, current matching between the two sub-cells must be achieved. A way to tackle the current matching problem is by bandgap tuning of the perovskite cell [11]. The ideal bandgap range for the perovskite cell is 1.7-1.8 eV [14]. Alternatively, current matching can be achieved by adjusting the absorber's thickness.

In the 4T configuration, the subcells are mechanically stacked but electrically independent. One terminal is present in the front and at the rear of each sub-cell, respectively. In that way, each cell can operate at its own maximum power point, such that the current matching requirement is lifted. This allows the selection of the perovskite top cell from a wider bandgap range of 1.6 to 2.0 [12]. In addition, the 4T terminals are less sensitive to spectral variations. The light absorption principle remains the same with the 2T tandem, i.e. short wavelength light is absorbed by the perovskite, and lower wavelength light from the silicon sub-cell. Nevertheless, a pair of TCO layers per sub-cell is needed, which may increase parasitic absorption. Although 4T tandems can have higher efficiencies than 2T tandems [15], they come at a higher manufacturing cost [16].

Finally, the 3T structure has been recently introduced with the intention of combining the advantages of 2T and 4T tandems. Two different internal interconnections have been proposed for 3T tandems, depending on the position of the third electrode: the middle contact and the Interdigitated Back Contacts (IBC) 3T tandems [17]. By placing the third electrode in the middle, the tandem cell can be fabricated monolithically; however, this option can reduce the cell's active area and is not preferred [18]. The IBC 3T architecture will be described in more detail below.

An IBC 3T design proposed by Santbergen et al. [19] involves a conventional n-type silicon heterojunction bottom cell with interdigitated back contacts at the rear that form the two terminals (base and emitter contact). The third terminal is on the front side of the perovskite cell, which is deposited on top. Moreover, this 3T IBC architecture can be further distinguished into two types, namely the pn-np and the np-np configuration. Their difference lies in the order that the layers are deposited on top of the silicon cell, as illustrated in Figure 1.3. In the pn-np configuration, the electron-transporting material is deposited first, then the perovskite material, followed by the hole-transporting layer, while in pn-np configuration this order is inverted. In the pn-np type, the electrons generated either on the top or bottom cell are collected in the bottom cell's negative terminal and the current produced is the sum of the two currents. In np-np type, in case of a current-limiting bottom cell, the base contact provides electrons, whereas when the current is limited by the top cell, the base contact draws electrons.

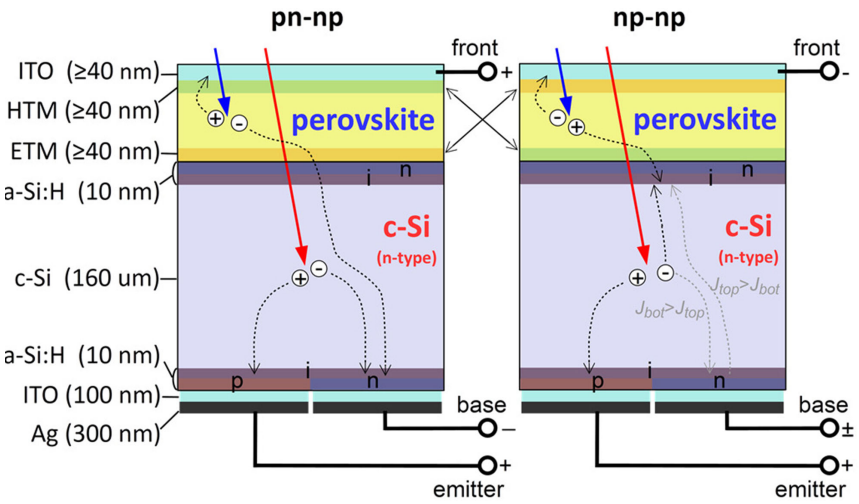

Figure 1.3: Representation of pn-np and np-np 3T IBC tandem cell configurations as proposed by [19].

Overall, energy yield simulations showed that 3T tandems perform better than 2T equivalent tandems as the current mismatch losses are eliminated. Furthermore, the optical losses are less compared to the 4T architecture. Conversely, all these advantages come at a cost due to increased interconnection complexity [20].

1.2.3 EQE of a perovskite-silicon tandem cell

The External Quantum Efficiency (EQE) is defined as the fraction of photons incident on a solar cell that gives carriers which are successfully collected. In other words, it measures the percentage of incident photons absorbed and converted into electrical current. An example of typical 2T PST cell EQE is illustrated in Figure 1.4.

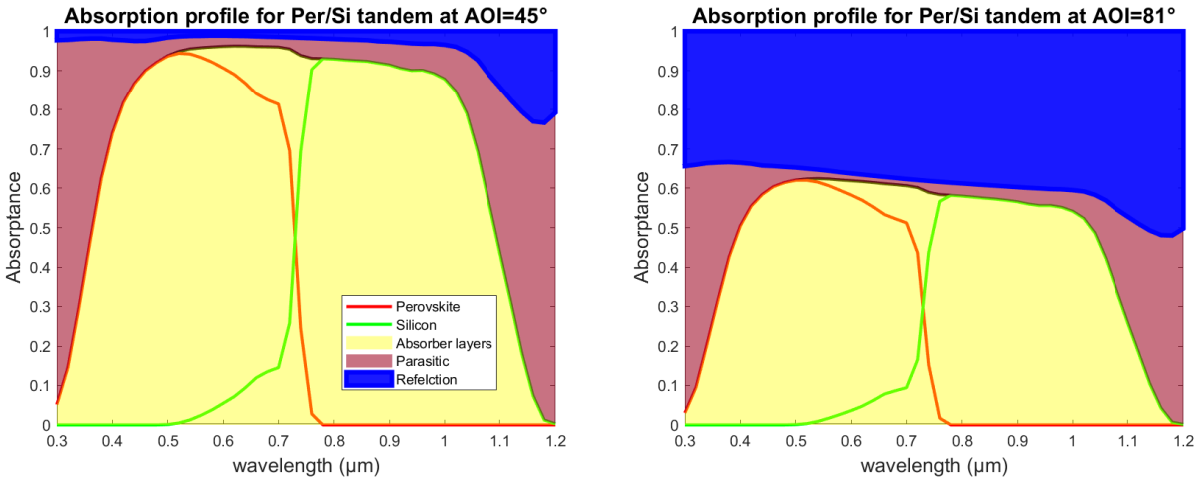

(a) (b)

Figure 1.4: Examples of the EQE of a PST cell, for an AOI: (a) of 45°, (b) of 81°.

As depicted in both figures, the perovskite absorbs high energy photons from the violet region and afterwards, while the silicon absorbs mainly in the infrared. In the tandem structure, there are multiple intermediate layers with different functionality, however, all of them contribute to the parasitic absorption, which is the area depicted by the purple colour. On top of the graph, the losses due to reflection (R) are shown. The graph is about a monofocial PST, which has a metal back reflector at the rear, so transmission (T) losses are set to zero. It should be noted, that the EQE is calculated for an Angle of Incidence (AOI) range from 0° (perpendicular to the cell) to 90° (parallel to the cell). The AOI refers to the angle between the normal to the cell's surface and incident light. By comparing Figure 1.4a and Figure 1.4b, the effect of AOI in the layers absorptance can be seen. A higher AOI leads to smaller absorptance for the tandem cell due to high reflection losses. In the figures above, an EQE plot is given from every layer, i.e. the perovskite on the left, the silicon

on the right, and the total cell on top (the borderline between parasitic and reflection losses) which includes the absorptance of both the absorber and intermediate layers.

1.3 Solar tracking technologies

In general, a solar tracking system is a mechanism that orients the panel towards the sun in order to maximize the energy yield production. To achieve this, tracking mechanisms aim to minimize the angle between the incident light and the module's surface normal, known as AOI. By lowering the AOI, more power from the direct irradiance component is extracted, and thus, the power output of the module is increased. According to literature, the tracking systems can be classified based on three criteria: the control strategies, the type of motion, and the motion's degrees of freedom [21, 22, 23]. In Figure 1.5 the tracking systems classification scheme is summarized.

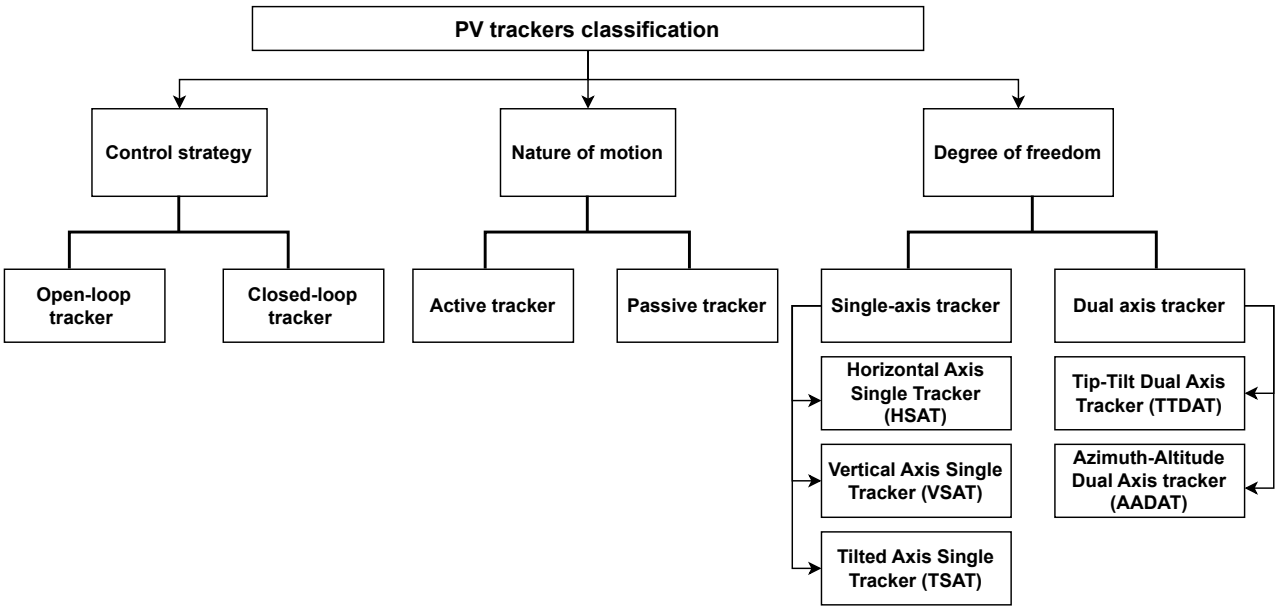

Figure 1.5: PV tracking technologies classifiacation

1.3.1 Based on the control strategy

With regard to the control system, trackers are distinguished into open and closed-loop. In the open-loop system, mathematical formulas are employed to predict the sun's position and move the panel accordingly. There are no components to observe the input and output data, such as sensors to sense the sunlight and evaluate the actual output with regard to the desired one. In essence, the orientation is determined by an algorithm that uses the panel's location and time as input data, without requiring any feedback. It is a low-cost system that does not have the ability to correct output errors [24]. On the contrary, closed-loop trackers, work on a feedback control system. They utilize optical sensors to estimate the real position of the sun, which are then feedbacked to the processor unit so it can detect the error and signal the motors and actuators to correct it. Such trackers provide high accuracy in sun tracking; however, this comes at a higher cost [25].

1.3.2 Based on the nature of motion

In this category, trackers are sorted into passive and active types. Active trackers operate based on the principle of materials thermal expansion. Materials like expandable gas or shape-memory alloys are placed on both sides of the panel. When the panels face the sun directly, both sides maintain equilibrium. Once the sun moves, the two sides receive unbalanced illumination, causing one side to heat more than the other. This induces thermal expansion of the material on one side and contraction to the other, causing the panel to rotate so that equilibrium is re-established. Although it is a simple and low-cost method, it fails to give high performance [26]. On the other hand, active trackers run on electricity. They integrate components such as sensors, electrical drives, gear trains, and microprocessors to track the sun with high precision, at the cost of some energy consumption [23].

1.3.3 Based on the motion's degrees of freedom

PV panels can rotate either around one axis (single-axis tracking) or two axes (dual-axis tracking). In the single-axis mode, the axis of rotation could be placed either in a vertical or horizontal direction with respect to the ground, providing a single degree of freedom to the module. In the first case, a Horizontal Single axis tracker (HSAT) is usually mounted in the North-to-South direction and follows the East-to-West movement of the sun over the course of a day. The tracker tries to align the altitude of the module to that of the sun. When the axis of rotation is vertical to the ground, the tracker is called Vertical Single axis tracker (VSAT). In this configuration, the module is placed on a fixed tilt, and moves vertically from east to west throughout the day, ensuring the module's azimuth matches the sun's azimuth (also called azimuth tracking). Finally, the last topology is the Tilted Single Axis Tracker (TSAT), where the axis of rotation is somewhere in between vertical and horizontal systems. The module's face is aligned parallel to the axis so that when the module tracks, it covers a cylindrical area [27].

The dual-axis system has two degrees of freedom: the module's rotation around two axes perpendicular to each other. This system can be broken down into two main variants: a Tip-Tilt Dual Axis Tracker (TTDAT) and a Azimuth-Altitude Dual Axis Tracker (AADAT). Their difference lies in the way modules are mounted on a structure. On a TTDAT modules are mounted on top of a pole, while on the AADAT they are mounted on a ring parallel to the ground [21]. In both cases, one axis alters the tilt and the other the azimuth of the module sensuring alignment with the sun's position over the day. Such a structure ensures that the module always aims at the direct component of light. Compared to a single axis, the dual axis system performs better; however, it requires a more complex control strategy and a complex mechanical system of rotating the module [28], leading to higher costs. Typically, dual-axis trackers are applied to solar concentrators. An illustration of various solar tracking configurations is shown in Figure 1.6.

(a) Horizontal Single Axis Tracker

(b) Vertical single axis tracker

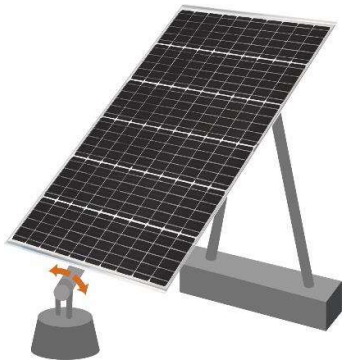

(c) Tilted axis single tracker

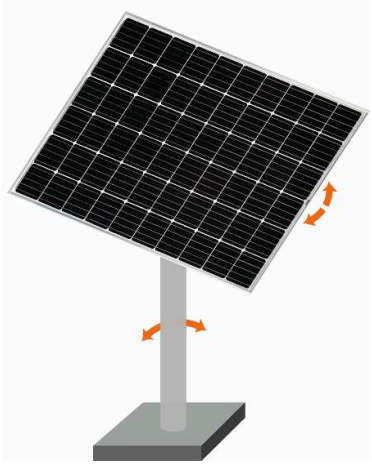

(d) Tip-tilt dual axis tracker

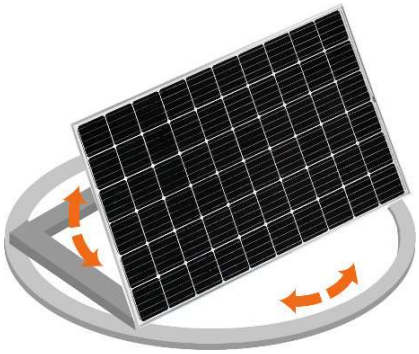

(e) Azimuth-altitude dual axis tracker

Figure 1.6: Tracking configurations on the basis of the motion's degrees of freedom. Figures sourced from [29].

Overall, the significant benefit of tracking systems is that they enhance the PV incoming irradiance, which in

turn leads to a higher energy output. Studies conclude that they can provide an increase in energy yield of about 12-25% for single-axis tracking and 30-45% for dual-axis compared to fixed-axis systems [30, 31, 32]. On the contrary, the major disadvantage is the energy consumption while the system is operational. In principle, the more complex the tracking system gets, the more the energy consumption. A challenge for an effective solar tracking system is to generate the maximum energy yield with the minimum tracker consumption.

1.4 Solar tracking and cell technologies

Solar tracking in PV applications is a well-established technology within the scientific community. That is explained by the diverse variety of solar trackers introduced in recent years in contrast to the traditional static panels [33]. The overwhelming majority of the commercial trackers are installed on c-Si modules since this is the most dominant technology, with a market share of over 95% as of 2021 [34]. From a research point of view, several studies examined the performance of tracking on c-Si modules [35, 36, 37, 38].

On the contrary, fewer researchers have tested the advantages of solar tracking on other cell technologies via modeling or experimental testing under real-world conditions. For instance, Lipovsek et al. predicted the energy yield of perovskite solar cells with varying tracking topologies using their own developed numerical model [39]. Similarly, the interest has increased for tandem structures. Steiner and Siefer experimentally studied the performance of triple junction cells (III-V on Silicon and III-V on Germanium) on dual-axis tracking at outdoor conditions [40]. Moreover, Ahangharnejhad et al. simulated the energy yield of tracking perovskite/CIGS tandem cells at specific locations [41].

However, to the best of the author's knowledge, the studies combining perovskite-silicon tandem cells and tracking systems so far are limited to the work of Horantner and Snaith and that of Babics et al. [42, 43]. The latter demonstrates, in an experimental setting, the performance of PST cell at an outdoor location. Babics, et al. investigated the effect of rear irradiance on the power output of a bifacial PST mounted on a HSAT and compared it with a fixed tilt module. Additional comparisons were made for a monofacial cell in the same tracking topologies as shown in Figure 1.7a . They showed a 55% energy yield gain for the bifacial PST on a single day between the two configurations. Although their findings underscore the high efficiency of bifacial PST, their results are limited to the daily output and concern a single module. In addition, the authors delivered annual results (Figure 1.7b) by modeling PST as silicon modules in PVsyst software, since it cannot simulate this cell technology [44]. This simplification may have an effect on the accuracy of the prediction.

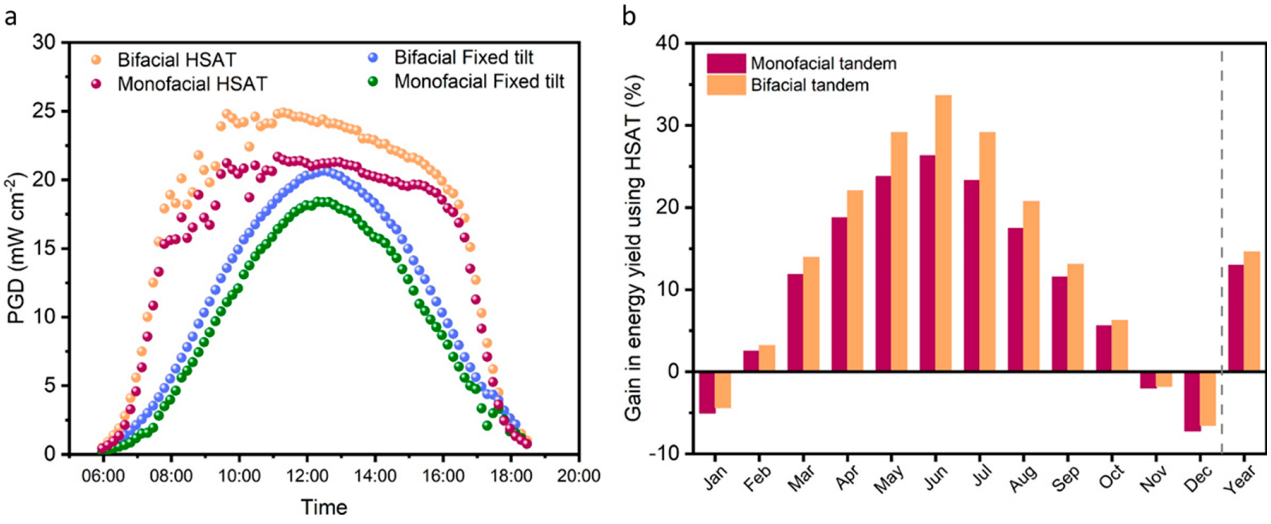

Figure 1.7: Selective results from the work of Babics et al. [43]. (a) Power generation density of a bifacial and monofacial PST module in two configurations. (b) Monthly results of the relative gain of a HSAT using PVsyst software. Authors observed a 15% more yield on bifacial modules annually. Negative values indicate the modules on fixed racks perform better in these months. Location: Thuwal, Saudi Arabia.

Horantner and Snaith conducted a more extensive modeling study [42]. They developed a rigorous optical model paired with an electrical model based on the one-diode equivalent circuit, to simulate PST modules with 2T, 4T architectures in realistic conditions and predict the energy yield for different tracking topologies. Some key results from their research are selected and illustrated in Figure 1.8. The study highlighted that

1-axis tracking systems are just as efficient as 2-axis trackers, especially for locations where the direct spectral distribution is more prominent. The authors also found that 4T tandem cells yield slightly more in contrast to 2T devices. Moreover, when optimizing materials and layer thickness of tandems for specific locations, tandem cells can produce 30% more yield than the Silicon Heterojunction (SHJ) cells. Despite the importance of this work, the authors overlooked significant parameters influencing the energy yield. First, they considered only planar structures in the c-Si absorber layers, which contradicts the industrial standards, where textured c-Si are typically used. This omission leads to an increase in the optical losses from reflection. Additionally, this study did not include the thermal behavior of the solar cells and its impact on the overall efficiency. Both constraints are taken into account in PVMD toolbox software presented below.

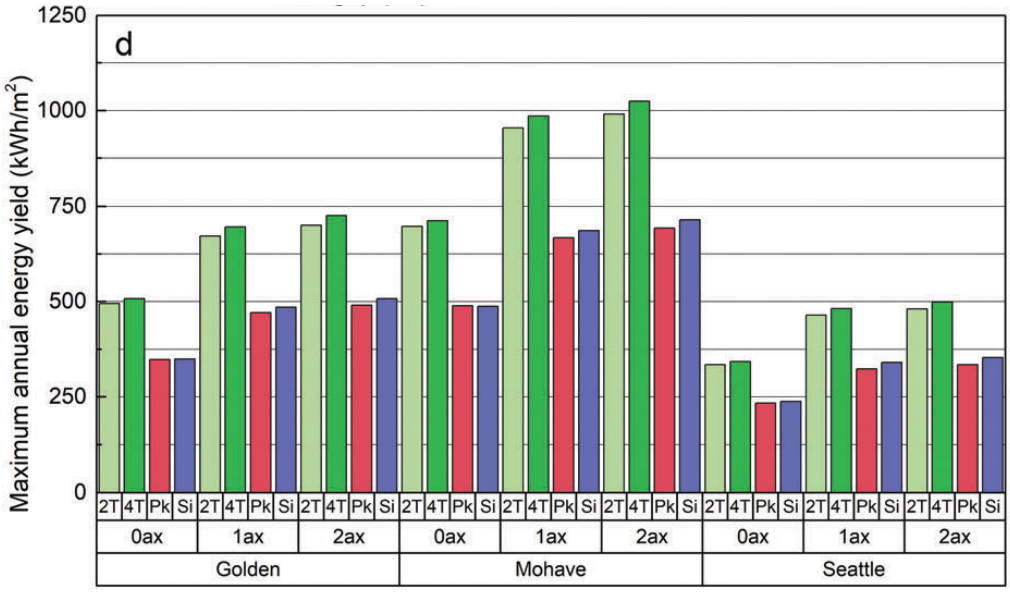

Figure 1.8: Selective results from the work of Horantner and Snaith [42]. The annual energy yield of cell technologies with varying tracking topologies for three U.S. locations: Golden, Mohave, and Seattle. In tandem cells, the perovskite bandgap is optimized per location.

1.5 The PVMD Toolbox

Researchers at the Photovoltaic Material and Devices (PVMD) group at Delft University of Technology have developed a Matlab-built software, the PVMD toolbox, able to simulate the energy yield of photovoltaic technologies from a cell to system level. From its initial creation, the toolbox has undergone many improvements by modeling new features, with the latest addition being a loss analysis model [45].

1.5.1 PVMD Toolbox structure

The toolbox is structured in self-consistent models that simulate the successive energy conversion steps, from calculating the incident irradiance to the final AC yield. These are the main building blocks of the simulation, namely the **cell, module, weather, thermal, electric, and conversion model**, briefly introduced below. Newly introduced are three models concerning the characterization of losses (**Loss Analysis model**), the degradation performance of solar cell or PV system (**Degradation model**) and the determination of Levelized Cost of Electricity (**Financial model**). Although the toolbox has been extended with new features, the description will be limited to the first six validated models. The description below follows the same structure as it is perceived by the user through the Graphical User Interface (GUI). An overview of the toolbox structure is given in Figure 1.11.

Compared to other PV softwares, the toolbox's uniqueness lies in the fact that it includes semiconductor device modeling, indicating that the simulation is based on fundamental material properties. Consequently, it can predict the energy yield of solar cells or modules that are not fabricated or are not yet available in the market, as is the case for PST. Finally, the integration of all the aforementioned models makes the toolbox a comprehensive modeling framework that can accurately predict the energy yield of PV systems.

Cell model

In this model, the optical properties of the cell are calculated by the use of GenPro4 software [46]. GenPro4 is an exclusively optical model that integrates wave and ray otpics to simulate light's interaction with a variety of cell technologies. GenPro4 approaches the cell as a 1D multilayer structure. Given as input the complex refractive index $\eta + ik$ (wavelength-dependent) and the thickness of each layer (d), the software implements the net radiation method [47] to calculate the reflectance (R), absorptance (A) and transmittance (T) of each layer as well as the overall cell. While computing, interference and scattering effects of light from flat or textured surfaces are considered. Reflection and transmittance are wavelength (λ) and angle (α) resolved while absorption is calculated as a function of λ, α, and d. In addition, the photogenerated current at STC is also determined.

Module model

At this level, the module's mounting conditions and surroundings are simulated. The toolbox assumes an infinite boundary condition and a free-horizon. Initially, the cells' geometrical characteristics are defined by the user, along with the number of cells in rows and columns. Likewise, properties such as azimuth, tilt angle, and height from the ground are the input to simulate mounting conditions. Albedo is also user-defined to account for surroundings. With the first parameters defined, the toolbox generates a simulation domain to visualize a PV module as part of a bigger PV plant, as shown in figure Figure 1.9. On top of the module, a hemisphere is created, where the so-called Sensitivity Map (SM) is computed. In essence, the sensitivity map illustrates the surface's sensitivity to the incoming rays and is expressed via the ratio of the number of absorbed rays from the module to the number of incoming rays for every solid angle of the skydome. It should be noted that generating the sensitivity maps is the most time-consuming step in toolbox simulations.

To determine the sensitivity map the LUX software is employed, performing forward Monte Carlo ray tracing. In this context, the skydome is discretized in 160 triangular sky elements (vertices), each corresponding to one light direction. The sensitivity for each vertex is calculated by ray-tracing simulation when the whole object is illuminated from this direction [48, 49]. Sensitivity maps are calculated for each junction material and one for the whole module as depicted in Figure 1.10. In addition, the toolbox computes the cell's average sensitivity. Individual cell sensitivity is an option for more accuracy, demanding though, more computational time.

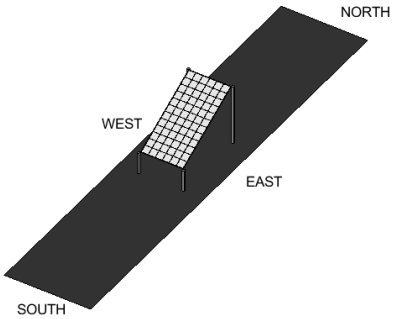

Figure 1.9: Mounting illustration of a module facing south with tilt 27°.

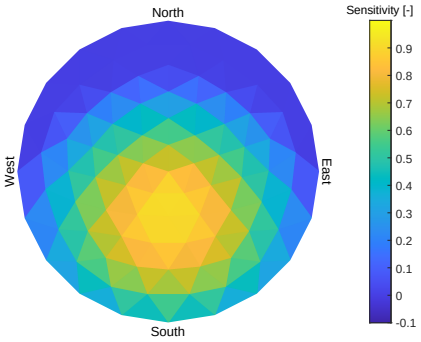

Figure 1.10: Sensitivity map for calculated for individual cells (Ray-tracing for 25000 rays).

Semiconductor model

Although the semiconductor model is not an explicit part of the GUI, it stands as an intermediate between the cell and electric models and, therefore, should be analyzed. The semiconductor model relies on the Advanced Semiconductor Analysis (ASA) software, developed within the PVMD group [50]. ASA is a one-dimensional semiconductor simulator that receives optoelectronic input for all layers and predicts the solar cell performance by solving Poisson and continuity equations. ASA's role as part of the toolbox is to generate each cell's I-V curve under varying temperatures and irradiances. Then an equivalent circuit based on the one-diode model is fitted to the I-V curves to obtain the Calibrated Lumped Element Model (CLEM). The five

parameters of the one-diode model are extracted subsequently as a function of temperature and irradiance. If a tandem cell is simulated, the parameters of both cells are extracted separately and later merged in an equivalent circuit for the tandem. These parameters are fed to the electric model discussed below.

Weather model

The toolbox extracts the weather dataset for the selected location from Meteonorm [51]. Having this input, the Perez model is applied to compute the sky luminance distribution across the sky elements at each time instance [52]. At this point, the effect of surrounding objects can be simulated in case a skyline profile of the location is available; otherwise, the toolbox assumes a free horizon [53]. The output of the Perez model is the irradiance sky map. Then, the toolbox employs SMARTS model to incorporate the spectral composition of the incident irradiance and photon flux [54]. By combining the sky map and the sensitivity map, the toolbox calculates the irradiance absorbed $G_{mod}(n_{cell}, t)$ as well as the generated photocurrent $I_{ph}(n_{cell}, t)$ at each cell and the module at any given time instance for the user-defined period.

Thermal model

By applying the fluid dynamics model, developed by Fuentes, the toolbox calculates the temperature of each cell at any time instance $T(n_{cell}, t)$ [55]. According to Fuentes' work, the module's temperature is obtained after solving the energy balance between the module itself and the surroundings. The balance comprises terms which express the types of heat transfer:

- Irradiance from the sun
- Convection between air and both sides of the module
- Convection between the module and mounting structure
- Radiative heat exchange between the module surface and the sky.

Input to the terms is irradiance, ambient and sky temperature, wind speed, mounting properties, and module's emissivity. As the above terms are also functions of the module's temperature, the energy balance is solved with iterative methods. It is essential to highlight that the model's mathematical framework is built on non-empirical parameters and thus allows to study the effect of various temperature-dependent properties on the module's temperature [49].

Electrical model

At this stage, three cell properties computed previously are now combined in the electrical model to calculate the DC yield and the module's I-V curve for all timesteps. First input is the photogenerated current J_{ph}, derived from the wheather model. Second input is the temperature T_{cell} of each cell as calculated in the thermal model. Thirdly, the five parameters of the one-diode model of each cell at various temperatures and irradiances are fed to the model (as obtained by the semiconductor model). All three properties are time-dependent, with a timestep usually of 1 hour. Throughout the examined period, the same J_{ph} and T_{cell} are frequently repeated, causing an excessive number of I-V curves calculated. Hence, these values are discretized in bins with 0.01 and 0.3 size for J_{ph} and T_{cell}, respectively. Then, only the discretized values are simulated to reduce computational time [49]. With this input, the toolbox combines the different calibrated lumped elements models and creates an extended equivalent circuit accounting also for the module's interconnections and bypass diodes. The module's I-V curve is calculated with the aid of the lambert W function [56]. The model generates the maximum power points of the module for all timesteps, which when added, give the total DC yield.

Conversion model

For the DC to AC conversion three types of inverters are simulated in the toolbox: central inverters, string inverters, and micro-inverters. The user has to define the number of modules in parallel and in series and select an inverter from a list of commercially available inverters. The conversion efficiency for all three types is calculated via the SNL-model [57]. Another converter topology available is power optimizers in which the efficiency is modeled with a software developed within the PVMD group [58].

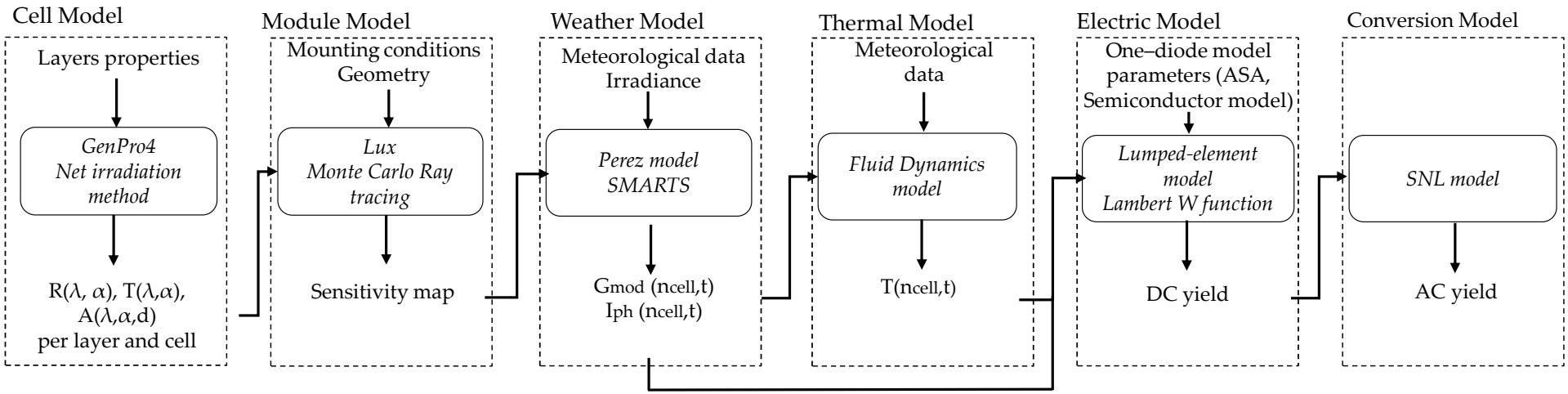

Figure 1.11: Schematic overview of the PVMD toolbox structure.

1.5.2 PVMD Toolbox limitations

One of the toolbox limitations, influencing the PST module simulations, lies in the method employed to spectrally resolve the irradiance. As briefly mentioned in Section 1.5.1, the Perez model constructs a distribution of the irradiance across the skydome (skymap). To spectrally resolve the irradiance coming from each sky element, the SMARTS model is applied. This process involves extracting spectra power data for ten air mass values from the SMARTS model, which are then normalized with respect to the total irradiance for each air mass. On an hourly basis, the air mass is calculated based on the sun's position. The spectrum corresponding to this air mass is interpolated from the SMARTS data. When applied to the absolute irradiance data derived from the Perez model, we obtain the spectrally resolved irradiance for any given time.

To better understand this concept, in Figure 1.12b, the normalized spectrum for an AM 1.2 is shown. On the left Figure 1.12a depicts the radiance for all vertices constituting the skydome at a time instance. The SMARTS model is meant to give the "spectrum shape" to irradiance data from the Perez model. As seen in the skymap, the vertices placed to the sun's position (yellow spot) have the highest irradiance values and thus appear brighter, since they represent the sun. On the contrary, vertices away from the sun have dramatically lower irradiance and appear darker [48]. Clearly, vertices at the sun's position are related to the direct spectrum of the irradiance, while those far from the sun are associated with the diffuse spectrum. However, toolbox does not differentiate between these and applies the same global irradiance spectrum (Figure 1.12b) to all vertices in the skydome. To visualize this, the vertices at the sun position (Figure 1.12c) and those away from the sun (Figure 1.12d), have the same spectral shape but way different irradiance values, seen on the scale of the y-axis. In reality, the Direct Normal Irradiance (DNI) and Diffuse Horizontal Irradiance (DHI) light components have a different spectral composition as indicated in Appendix D.

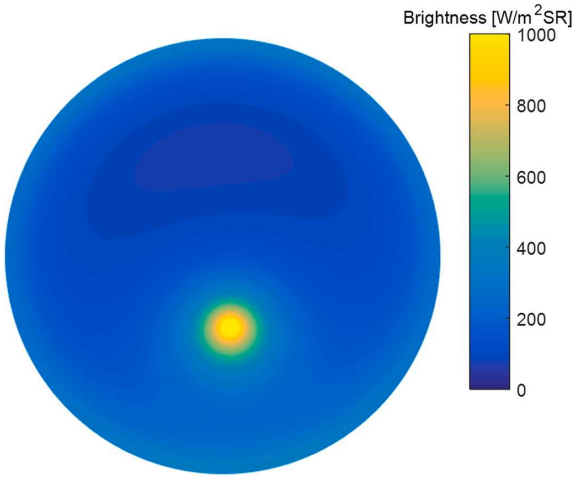

(a) Skymap for one-time instance

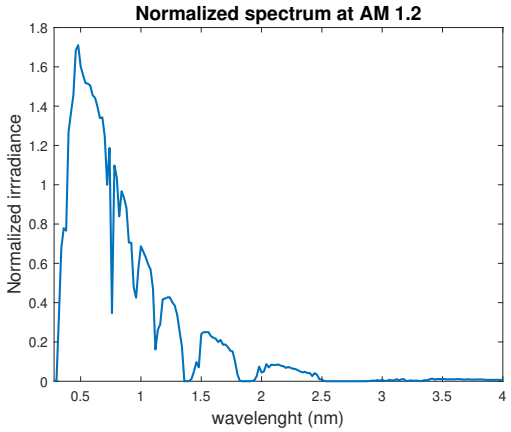

(b) SMARTS AM 1.2 spectrum (interpolated)

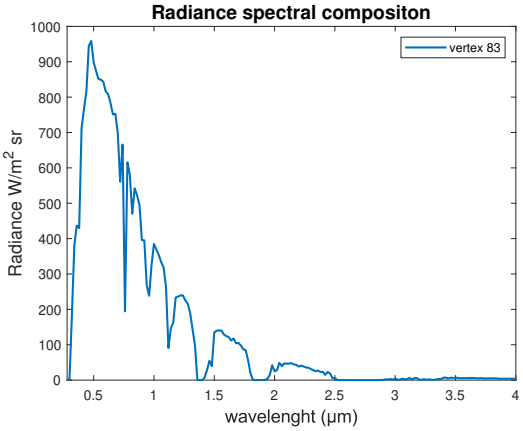

(c) Radiance composition for sun-verex

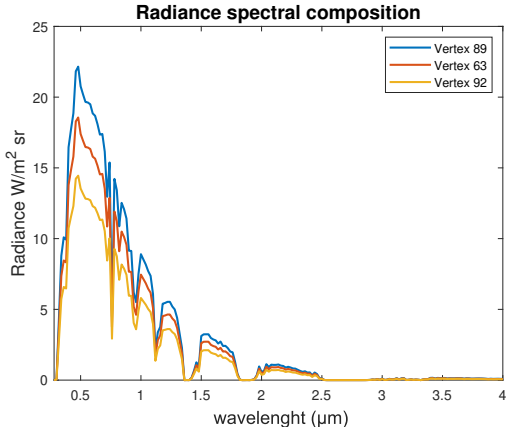

(d) Radiance composition for away from sun vertices

Figure 1.12: Spectral composition approach applied in the toolbox

1.6 Research gap and thesis objectives

As with any other scientific research, this study aims to uncover a knowledge gap and address it. In this section, the knowledge gap is identified first, followed by the thesis objectives.

1.6.1 Research Gap - motivation

The initial research gap addressed here concerns the toolbox limitations. The current version can simulate only cell technologies mounted on fixed racks, with the orientation determined by the user. In this regard, adding solar tracking features will be a significant enhancement to the toolbox.

As discussed in Section 1.3 and Section 1.2, solar tracking and perovskite-silicon tandem cells can individually enhance the module performance. It logically follows that coupling those two can boost the energy yield even more. To the best of the author's knowledge, there is limited research conducted on perovskite-silicon tracking modules [42, 43]. Furthermore, these studies are subject to fundamental limitations (see Section 1.4). Thus, the second research gap lies in providing comprehensive modeling of PST tracking modules, which can be realized utilizing the PVMD toolbox, enhanced with a tracking model.

In summary, this research is motivated by the dual need to upgrade the PVMD toolbox and uncover the full potential of solar tracking on perovskite-silicon tandem cells. Modeling solar tracking PST modules will provide insights into their behavior and energy yield, pointing the way for their commercial development.

1.6.2 Thesis objectives

It should be stated that this work acts as a continuation of several studies done before by TU Delft students on expanding the PVMD toolbox. The content of this work falls under the **main research objective:**

Optimize solar tracking strategy for maximum energy yield production of monofacial tandem modules

As already stated, the existing version of the toolbox does not feature solar tracking. To complete the above objective, a solar tracking model needs to be developed. Before conceptualizing such a model, we consider the dual goal of a solar tracker: first, the fast computation of incident irradiation in various module orientations and, secondly determination of the orientation capturing maximum irradiance. With these in mind, the main objective can be framed by the following sub-objectives:

1st sub-objective: Developing a method for faster determination of absorbed irradiance

Time serves as a significant bottleneck for irradiance calculation in the current version of the toolbox. This limitation arises primarily from the use of the ray-tracing method, as elaborated in Section 1.5.1. The goal is to overcome this barrier by introducing a new method based on a view factors. The new approach promises quicker determination of irradiance in multiple module positioning. Aim of the this report is to validate the new method by comparing it with the ray-tracing approach.

2nd sub-objective: Finding the optimum algorithm that maximizes the absorbed irradiance

As discussed before, the tracker should locate the orientation that maximizes the absorbed irradiance. This translates into an optimization problem that must be addressed at each interval set by the tracker's time resolution, for instance, every hour. For this sub-objective, the focus is on exploring or developing algorithms that locate the global optimum (accuracy) within a desired time (speed). The optimum algorithm, satisfying both criteria, should then be chosen. Once established, they should be integrated into the overall control strategy of a tracking system.

3rd sub-objective: Energy yield simulations of tracking tandem PV modules at real-world conditions

With the solar tracking model built in the 1st and 2nd sub-objectives, the last sub-objective involves the application of the model in tandem cells. The goal is to evaluate the impact of solar tracking on the energy yield performance of tandem structures at normal operating conditions. Essentially, the focus is on analyzing the energy gain of the tracking system on this technology in different locations, scattered around the globe, each representing a distinct climate.

1.7 Thesis outline

Having established the thesis objectives, the report is structured in a way that chapters 2 to 4 answer to the corresponding sub-objectives 1 to 3. Specifically, Chapter 2 demonstrates the implementation of a view factor model in calculating the irradiance. Next, Chapter 3 analyzes the optimization techniques followed to solve the irradiation maximization problem, which are part of the tracking control strategy described in Section 3.6. The models in Chapter 2 and Chapter 3 together constitute the total solar tracking model. In Chapter 4, results on the energy yield performance of tandem structures with a dual-axis tracking mechanism are presented and compared on different timescales to static module topologies. Finally, the conclusions of this study are provided in Chapter 5 along with recommendations for future research.

Chapter 2

Irradiance Calculation: A View Factor Model

The overall solar tracking model can be distinguished into two distinct parts: a model that computes the irradiance and a second model that identifies the optimal orientation for maximum absorbed irradiance. The overall simulation approach is presented in Section 2.2. This chapter delves into the irradiance calculation method. In Section 2.1, the current method the toolbox implements is discussed, while pinpointing its limitations. These limitations create the need for an alternative method to irradiance calculation, introduced in Section 2.3. Ultimately, a comparative analysis of the two methods is made in Section 2.4.

2.1 The current irradiance model in the PVMD toolbox

As already mentioned in Section 1.5.1, the toolbox computes the absorbed irradiance by dividing it into two parts: the sensitivity map, which is obtained through ray tracing, and the irradiance skymap, generated by applying Perez and SMARTS model [48]. Next, the absorbed irradiance at any given time is determined by integrating skymap times the sensitivity map across the entire skydome according to the equation:

$$Irradiance(n_{cell}, t) = \int_{sky} Sensitivity\, map(n_{cell}, \Omega), \cdot Skymap(\Omega, t)\, \mathrm{d}\Omega, \tag{2.1}$$

where t represents the time instance, Ω the position on the skydome and n_{cell} corresponds to the cell number for which the irradiance is being calculated. Bear in mind that the sensitivity map is generated once, irrespective of the weather data, while the skymap is produced for each specific time instance

The main concern in this work, centers around the sensitivity map, since that is the time-determining step not only for the irradiance calculation but also for the overall toolbox simulation. For this reason, ray tracing will be further discussed below.

The toolbox creates a sensitivity map to quantify the amount of absorbed light of each cell layer with respect to the incident light coming from different directions of the skydome. That is expressed via sensitivity values given by the equation :

$$Sensitivity = S_R = \frac{N_{\text{Rays absorbed}}}{N_{\text{Rays incident}}}, \tag{2.2}$$

where the R stands for Ray tracing. Sensitivity values are extracted from LUX software as a function of four parameters [49]:

$$S_R = f(vertex, n_{cells}, lay, \lambda), \tag{2.3}$$

where the vertex is the sky element in the skydome, n_{cells} is the cell for which the sensitivity values are calculated, lay is the cell layer, and λ the wavelength. There are 160 vertices while the cell number is user defined (typically 72). The layer parameter has two dimensions, one for the absorber(s) layer and another for the total cell, including all intermediate layers.

The LUX software, performs ray tracing for a declared number of rays per direction. To complete the sensitivity map, ray tracing is made for all directions of incoming light in the skydome. **It is important to highlight that sensitivity map is calculated for an already set module geometry with a fixed tilt angle and azimuth.**

Note that, an increased number of rays traced, leads to a more accurate result at the expense of computational time. A number of 25000 rays is considered sufficient. Moreover, taking into account the large number of rays traced for all vertices and each cell, it is concluded that generating the sensitivity map is the most time-consuming part of the simulation. Nevertheless, the sensitivity map is the key element in the calculation of the absorbed irradiance and is considerably changed when the azimuth or tilt angle of the module varies. Thus, it will act as the main point of interest when trying to track the sun.

2.1.1 Limitations of ray tracing

In ray tracing simulations, rays need to be traced from a source to a target surface or vice-versa, considering interactions with multiple surfaces in the scene. Ray tracing algorithms can be categorized into two main groups: forward and backward ray tracing [59]. Forward Ray tracing methods estimate the irradiance on the PV module by following rays starting from light sources (usually the sun), as they reach the PV module. In backward ray tracing, rays are traced in the reverse path from the PV module back to the light source. In the toolbox model, forward ray tracing is applied. This is a complex process that entails computationally intensive calculations. Additionally, a substantial number of rays (25.000-50.000) must be traced to obtain accurate results, resulting in increased computational time. As a consequence, the primary limitation of ray tracing methods lies in their inherent time-consuming nature.

In the context of the LUX software, the computational time required to generate the sensitivity map is influenced by the module's tilt and albedo choosen. Table 2.1 presents the average computational time for ray tracing in a PST using a laptop with a 2.8 GHz processor and 16 GB of RAM. It is evident that higher tilt angles correspond to longer computational times, indicating a clear trend.

Table 2.1: Average computational time of ray tracing for various tilts on a PST module. Numbers refer to average sensitivity values. Rays: 25000, albedo: 0.2.

Tilt angle (°)	Time (min)
0	12.2
10	14.2
20	15.9
30	17.3
40	18.9
50	19.6

In a simulation aimed to make the module trace the sun, the module's azimuth and/or tilt angle should be adjusted based on the corresponding values of the sun at any given time. As it is the current version of the toolbox, for a fixed module positioning, ray tracing is called once. This suggests that whenever there is an azimuth-tilt angle change, to align the module with the sun at any given time, the sensitivity map needs to be recalculated. This process has to be repeated for all time intervals over the simulation period when there is daylight. **Given the computation time shown in Table 2.1, the option of reperforming ray tracing for all module configurations is not a viable choice to include in a solar tracking model.** Notably, when the simulating period is a year, and tilt of a tracking module changes hourly, the computing time scales extremely. Therefore, an alternative solution should be searched, focusing on diminishing the computational effort to extract the sensitivity values.

2.2 The proposed simulation approach

This section introduces the structure of the proposed approach for a solar tracking model. The objective of solar tracking is to maximize the available irradiance, and thus, the designed model involves only the toolbox blocks, which serve as input in the irradiance calculation: the cell, module, and weather block.

The rationale behind this approach is to replace the time-consuming ray tracing step with a faster approach for sensitivity based on view factors. The irradiance skymap generated by Perez and SMARTS model remains unchanged, but an optimization model is introduced alongside it to ensure maximum absorbed irradiance. Essentially, with the proposed approach, a modification is made to the existing method of calculating irradiance, and algorithms are added to maximize it.

The proposed model comprises two building blocks: a view factor model, which is introduced in this Chapter, and an optimization model, which is covered in Chapter 3. Schematically, the modifications in the toolbox structure model, when applying this approach are displayed in Figure 2.1.

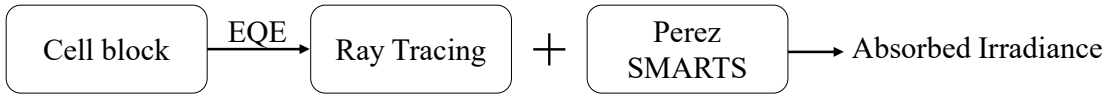

(a) Current version of toolbox

(b) Proposed structure of the solar tracking application

Figure 2.1: Modification of the toolbox structure in relation to the current version, following the implementation of the solar tracking model

2.3 New approach on sensitivity: a view factor model

This approach presents an alternative method for calculating and expressing the sensitivity values with an emphasis on reducing computational time. The approach is based on view factor models. **In this model, the skydome domain, divided into 160 discrete elements, remains unchanged**. Each sky element is treated as a surface from which irradiance leaves and strikes the surface of the module, a concept similar to the view factors. The aim is to quantify the fraction of irradiance coming from each vertex that reaches the module and can be absorbed. **This new quantity is called View Factor Sensitivity, represented as S_{VF}, and should not be confused with the sensitivity obtained through Ray-tracing, denoted as S_R.** The S_{VF} is decomposed in two terms: sensitivity related to direct/diffuse irradiance and sensitivity associated with reflected irradiance.

$$S_{VF} = S_{Direct/Diffuse} + S_{Reflected} \tag{2.4}$$

Additionally, the computation of S_{VF} for a module is made under the assumptions:

- Module is considered to stand alone. There is no effect from neighboring modules.
- Each cell within the module receives an equal amount of irradiance.
- The ground reflection for reflected sensitivity component is considered to be specular.
- The proposed model is designed only **for monofacial solar modules**. Thus, irradiance reaching the backside of the module is excluded.

The complete expression of S_{VF} along with the corresponding terms will be explained in the sections to follow.

2.3.1 Sensitivity of the direct/diffuse irradiance

This sensitivity component pertains to the vertices that directly "illuminate" the front side of the module, without considering the albedo effect. The expression of direct/diffused sensitivity component is given by the following formula:

$$S_{Dir/Dif} = EQE \cdot \cos(AOI_D), \tag{2.5}$$

where EQE is the solar cell's External Quantum Efficiency with its dependency parameters shown below. AOI_D is the angle of incidence between the light coming from each vertex and the module's surface normal. The subscript D indicates the correlation of AOI with direct/diffuse irradiance.

As stated in Section 1.5.1, the Cell block returns the R, A, T values of cell layers, utilizing GenPro4 software. These values are used to construct the EQE curves as discussed in Section 1.2.3. Subsequently, the EQE curves are incorporated into equation Equation 2.5. The EQE in the equation above is represented as a function of the AOI, layers, and wavelength.

$$EQE = f(AOI, lay, \lambda) \tag{2.6}$$

Since this work primarily focuses on tandem cells, the layers are defined as such: one layer corresponds to the Perovskite cell, another layer to the Silicon cell, and a third "layer", referred to as the total cell, includes the absorbers and parasitic absorptance values (specifically the 1-R-T values). The λ range is 300-1200nm with a step of 20nm while AOI spans from 0° to 90°. The number of angular intervals is set to 30, resulting in an angle step of 3°. The calculation of R,A,T values is repeated for every wavelength and AOI in the respective range to generate the EQE curves.

Angle of incidence calculation

Each vertex in the skydome is characterized by two coordinates: the azimuth A and the altitude α. Similarly, the module's position can be described by the coordinates of the surface normal, namely its azimuth and altitude. When considering a specific vertex in the skydome, as illustrated in Figure 2.2, the angle between the light originating from this vertex and the normal to cell/module surface is determined by Equation 2.7.

$$cos(AOI) = cos\alpha_M \, cos\alpha_v \, cos(A_M - A_v) + sin\alpha_M \, sin\alpha_v \tag{2.7}$$

where A_M and α_M are the azimuth and the altitude of the module, respectively, and A_v is the azimuth and α_v is the altitude of each vertex.

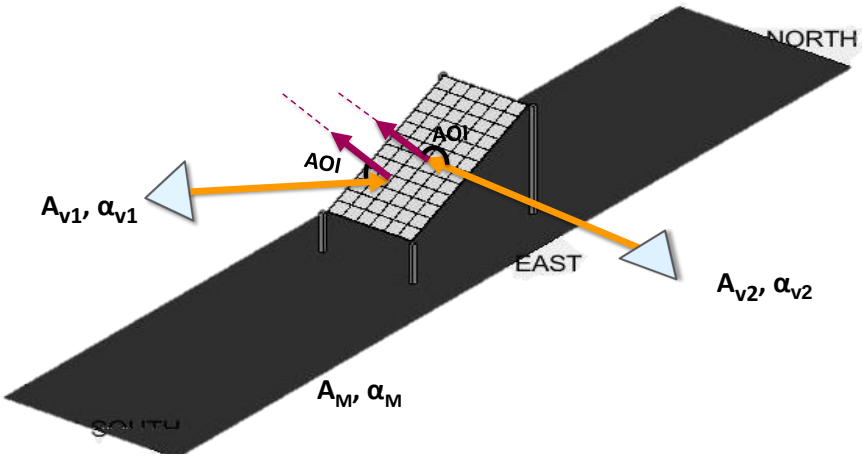

Figure 2.2: Angle of Incidence between the incoming light from a vertex and the module's surface normal.

For a fixed module position, the AOI is computed for all vertices of the skydome. Nevertheless, given the geometry of the hemisphere, certain vertices reach the back side of the module either directly or via reflection. Due to the model's monofacial nature, only vertices that directly reach the front side are considered. This selective inclusion is achieved with the following equation:

$$AOI_D = max(cos(AOI), 0) \tag{2.8}$$

Given the vertices selectivity the AOI_D is solely determined by the module and vertex position. Figure 2.3 visualizes examples of vertices that are included or excluded in the calculation of the $S_{Dir/Dif}$ component.

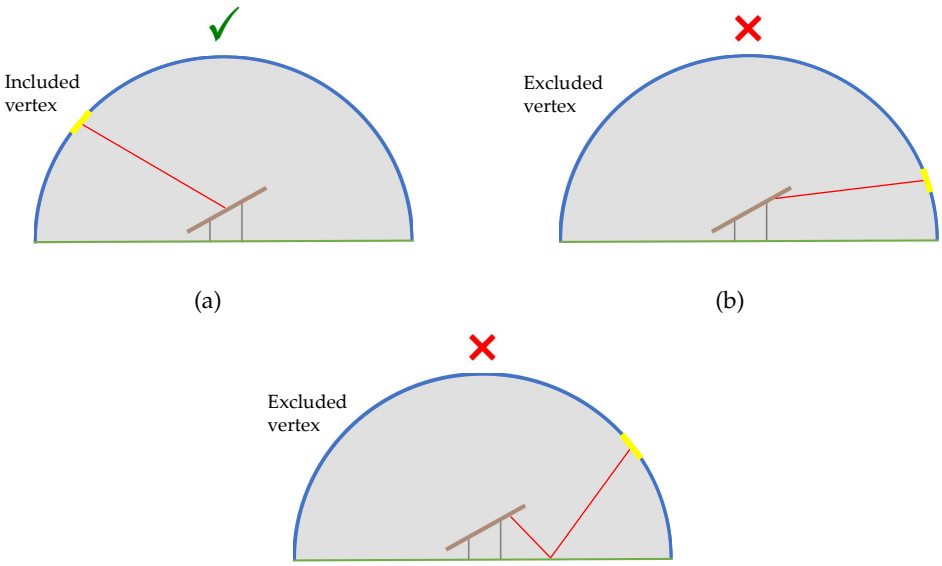

(a) (b)

(c)

Figure 2.3: Vertices that contribute or not in the $S_{Dir/Dif}$ calculation. In case (a), the vertex directly strikes the front side, while in cases (b) and (c), vertices reach the rear side of the module

2.3.2 Sensitivity of the reflected irradiance

As mentioned earlier, to simulate the light reflected from the ground, specular reflection is considered. The surface is assumed to be smooth and even, and light is reflected in a single direction at a definite angle. Despite the ease of its implementation, specular reflection may not accurately portray the conditions in actual PV fields, where the surfaces are often uneven and exhibit diffuse reflection.

To illustrate this concept, let's consider a ray originating from vertex A in the skydome, as depicted in Figure 2.4. The light bounces off the ground and directly hits the front side of the module. Specular reflection implies that the angle of incidence equals the angle of reflection. By extending the straight line to a mirrored skydome with respect to the ground, it can be seen that vertices A and B have specific properties:

$$Azimuth_A = Azimuth_B \tag{2.9a}$$

$$Altitude_A = -Altitude_B \tag{2.9b}$$

The Sensitivity related to the reflected irradiance for light coming from any vertex is modeled by using the same equation as before:

$$S_{Reflected} = albedo \cdot EQE \cdot \cos(AOI_R), \tag{2.10}$$

where the albedo factor is included. AOI_R denotes the AOI for reflected irradiance. In this case, the AOI_R for any vertex is calculated by Equation 2.7, but using the coordinates of its mirrored vertex, according to Equations 2.9a and 2.9b.

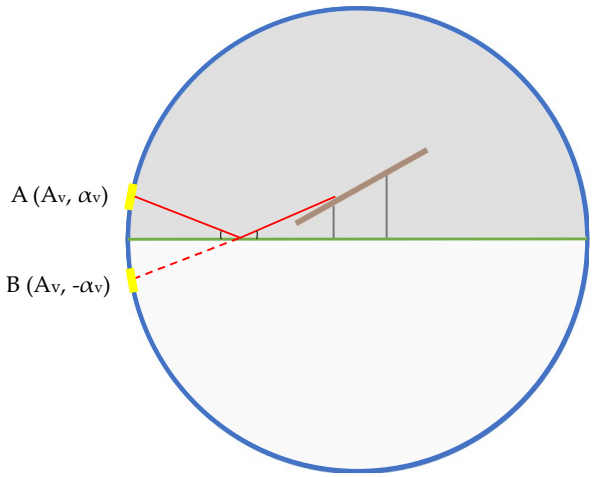

Figure 2.4: Assumptions for the $S_{reflected}$ calculation of a vertex A in the skydome. Vertices A and B are symmetrical with respect to the ground.

2.3.3 Sensitivity of the total irradiance

Overall, the complete expression of the view factor Sensitivity is given by the Equation 2.11:

$$S_{VF} = S_{Direct/Diffuse} + S_{Reflected} = EQE \cdot \cos(AOI_D) + albedo \cdot EQE \cdot \cos(AOI_R) \tag{2.11}$$

In addition, the dependency of S_{VF} on its parameters is expressed in the following formula:

$$S_{VF} = EQE(\boldsymbol{AOI_D}, \text{lay}, \lambda) \cdot \cos(\boldsymbol{AOI_D}) + \text{albedo} \cdot EQE(\text{lay}, \boldsymbol{AOI_R}, \lambda) \cdot \cos(\boldsymbol{AOI_R}), \tag{2.12}$$

$$0 \leq S_{VF} \leq 1 \tag{2.13}$$

Note that for a fixed module orientation, each AOI_D/AOI_R value corresponds to a single vertex-module position. In other words, the dependency of S_{VF} can be described by the vertex number, instead of AOI_D/AOI_R. Furthermore, light originating from one vertex encompasses all the wavelengths within the range mentioned above. Then, the sensitivity is calculated for every vertex, layer, and wavelength. In total, it can be expressed as a function of the following parameters:

$$S_{VF} = f(vertex, lay, \lambda) \tag{2.14}$$

It should be stressed that the EQE is extracted from GenPro4 using the closest AOI_D/AOI_R to the one calculated with Equation 2.7. GenPro4 could return the R, A, T values with a finer angle resolution such as 1°, instead of 3°, to better align with the calculated AOI_D/AOI_R. However, the difference in sensitivity values resulting from this adjustment is minor. Furthermore, adopting a smaller AOI resolution in GenPro4 would lead to longer simulation times, which is also taken into account. Finally, considering the overall expression of the S_{VF}, it becomes evident that its range spans from 0 to 1. This renders the view factor sensitivity comparable with the sensitivity obtained through ray tracing, as both exhibit variations within the same range.

So far, the discussion has focused on view factor sensitivity values for a fixed module orientation. However, in the case of solar tracking, the module's position should be adjusted accordingly. Therefore, the view factor model should be capable of calculating sensitivity values for any module position. With this objective in mind, let the module's azimuth and tilt vary within the range of 0° to 360° and 0° to 90° respectively. By utilizing Equation 2.7, the AOI_D/AOI_R values are recalculated for a given azimuth and tilt of the module. Subsequently, by extracting the appropriate EQE values, the overall S_{VF} is computed according to Equation 2.11. Thereby, the sensitivity values for all possible module orientations are obtained. In summary, the view factor model can effectively express the sensitivity values involving five parameters.

$$S_{VF} = f(vertex, lay, \lambda, azim, tilt) \tag{2.15}$$

An overview of the view factor sensitivity calculation method is shown in Figure 2.5. Remember that the complete S_{VF} array is computed for a total of 160 vertices, 3 layers, 46 wavelength, 360 azimuths, 90 tilt angle values.

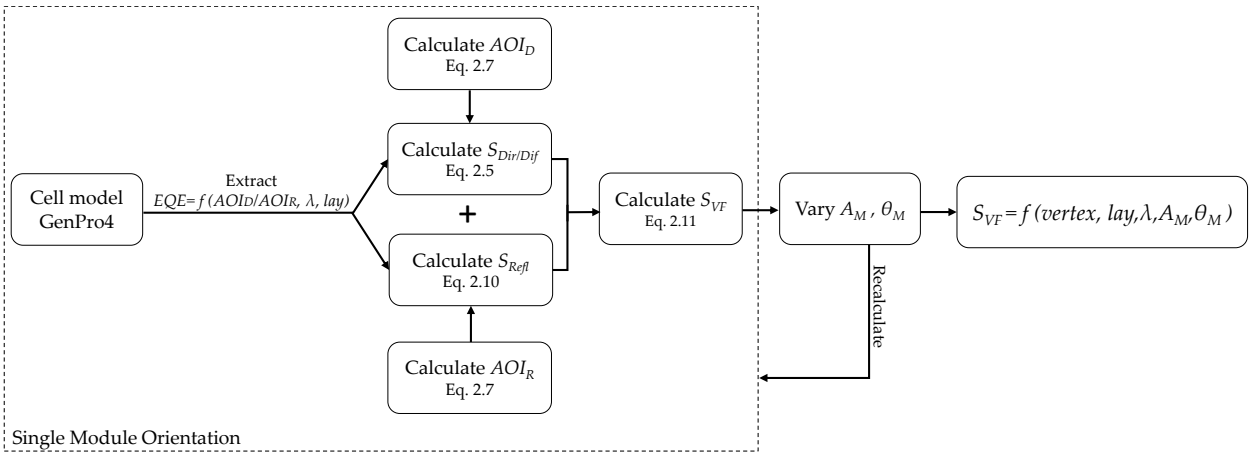

Figure 2.5: Schematic illustration of the S_{VF} calculation.

Unlike the sensitivity calculated with ray tracing, this expression does not account for any cell dependency. Nonetheless, if the average cell sensitivity option is selected for ray tracing, both expressions (Equation 2.3 and Equation 2.15) will depend on the same parameters except for the module coordinates.

2.4 Comparative analysis: view factor against ray tracing

Both ray tracing and view factor methods are used to calculate the sensitivity map, which serves as the first component in the irradiance calculation (Equation 2.1). To validate the effectiveness of the proposed new method, a comparison is conducted between the two approaches on the basis of two criteria: the time required to determine sensitivity values and the accuracy of the results.

2.4.1 Computational time comparison

Goal of the new approach is the faster computation of sensitivity values. **To better define what constitutes "faster", an upper time limit of 1s has been set for the computation of S_{VF} values for single module orientation.** This estimated time frame is considered the maximum allowable duration that would render the irradiance calculation fast enough to be incorporated into a solar tracking model.

As indicated in Table 2.1, ray tracing requires a substantial amount of time, **over 12 minutes**, to calculate sensitivity values for a single module placement. In contrast, the view factor model's runtime was found to be significantly lower **at 0.1 seconds on average** for a single orientation (Laptop: 2.8 GHz 16 GB RAM). It is worth mentioning that the recorded time starts from the moment the ray tracing or view factor model is called until they return the sensitivity values, excluding any toolbox blocks before or after them. This outcome is logical considering the complexity and magnitude of calculations in ray tracing, and a set of equations used in the the view factor model.

To further underscore the speed of the view factor approach, it takes about 1.2 minutes to calculate the sensitivity values for all possible module positions (360 azimuth x 91 tilt values combinations). As mentioned in Section 2.1.1, the corresponding time with ray-tracing is extremely big (exceeding one day of runtime). However, it should be noted that S_{VF} values for all module positions, cannot be stored in a multidimensional array-like structure, due to a considerable memory demand. Instead, they are produced for a single orientation when called.

The time measurements mentioned above, clearly demonstrate that the view factor model outperforms ray tracing and the same time remains well within the set time limit. Furthermore, the computational time for the view factor remains unaffected by a rise in tilt or albedo in contradiction to ray tracing. Overall, the view factor model presents a more time-efficient alternative to ray tracing.

2.4.2 Results comparison

Proving the fast computational speed of the view factor model is a necessary but not sufficient condition on its own to substitute ray tracing. Equally vital is to demonstrate the accuracy of the proposed model in generating sensitivity values. To establish the concept of "accuracy", ray tracing, as a more sophisticated method,

is regarded as a reference model to compare the deviation between the S_R and S_{VF} values. **Initially, a specific example with predefined values for module orientation and albedo is used for comparison. Afterwards, the findings are generalized to draw broader conclusions.**

To visualize this deviation, the sensitivity values of a single module orientation for different vertices in the skydome are selected, as depicted in Figure 2.6. Each vertex has specific coordinates in the skydome, indicated in the title. Keep in mind that the convention followed in the toolbox for the azimuth is that $A \epsilon [0°, 360°]$, with S=0°, W=90°, N=180°, and E=270°. In terms of module tilt θ, 0° corresponds to a horizontal module and 90° to a vertical module.

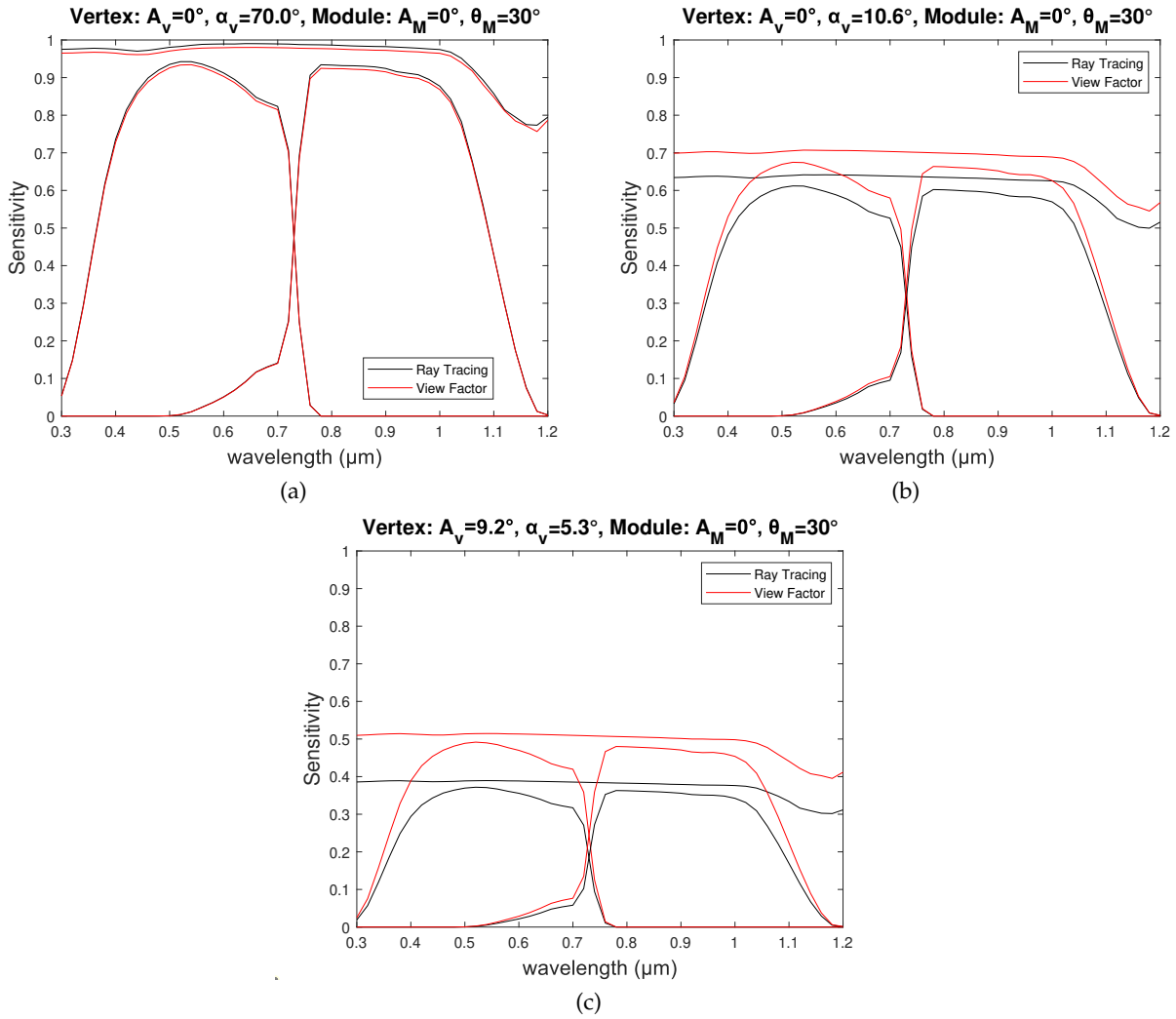

Figure 2.6: Sensitivity values against the wavelength of multiple vertices computed with ray tracing and view factor method. The values are calculated for albedo 0.2, with the tandem module facing south and tilted at 30°

In each of the subfigures above, 3 pairs of lines are presented. Each pair depicts sensitivity values against the wavelength calculated with ray tracing (black line) and the view factor method (red line). The three pairs of lines correspond to three cell layers for which sensitivity values are extracted. The curves displayed on the left correspond to the perovskite cell, while those on the right are linked to the silicon cell. Finally, the topmost curves refer to the total cell. Again the "total cell" layer refers to all the cell layers (absorber and intermediate layers). Analyzing all three layers is essential because sensitivity values from each serve as input for quantities calculated later. Values from the total cell contribute to the cell's absorbed irradiance calculations, while those from the absorber layer are used to compute the respective photocurrents.

For each layer, both S_{VF} and S_R curves follow similar trends per layer. These trends resemble the respective layer's EQE shape, depicted in Figure 1.4. This similarity can be explained by considering the formula of S_{VF} (Equation 2.11) and the fact that ray tracing utilizes the R, A, and T values as input parameters (see

Figure 1.11). The sensitivity values for the perovskite layer exist within the wavelength range, where the perovskite layer absorbs light. Similarly, the sensitivity values for the silicon layer fall within the range of wavelengths absorbed by silicon. Evidently, sensitivity for the total cell (top curve) is higher, as it "adds" up the sensitivity of the absorber and parasitic layers.

Out of the 160 vertices in the skydome, the vertices presented here are carefully chosen, such that insightful observations can be made from these graphs. The following conclusions refer to sensitivity values obtained from both methods. Initially, it is apparent that the sensitivity values depend on the relative vertex-module position. Vertices located directly above the module exhibit high sensitivity values, while those facing the back of the module show zero sensitivity.

In the case illustrated in Figure 2.6, the module is oriented towards the south and tilted at an angle of 30° or α_M=60°. The vertex shown in Figure 2.6a ($A_v = 0°$, $\alpha_v = 70°$) shares the same azimuth value and has an altitude close to that of the module. Thus, this vertex is positioned directly above the module, justifying its high sensitivity. On the other hand, the vertex in Figure 2.6b ($A_v = 0°$, $\alpha_v = 10.6°$), which is on the same azimuth but at a lower altitude, exhibits relatively lower sensitivity values on average. The vertex depicted in Figures 2.6c is misaligned with the module's azimuth and faces the southwest direction. Due to this misalignment, this vertex is, on average, less sensitive to incoming light in comparison to Figures 2.6a and 2.6b. Overall, the position of each vertex with respect to the module assigns a distinct weight to each vertex to determine its importance in the sensitivity calculation and, consequently, in the absorbed irradiance.

The graphs clearly illustrate that the difference in sensitivity values between the two methods varies depending on the vertex for a given module orientation. In addition, for a given vertex and layer, the difference fluctuates with respect to the wavelength. In the case of the perovskite and silicon layers, the difference is relatively smaller at the edges of the curves, but becomes bigger on the plateau located at the top, as observed across all instances presented in Figure 2.6. Instead, the difference in the total cell remains relatively constant across all wavelengths for all vertices.

To quantify the difference between sensitivity values of ray tracing and view factor the RMSE metric is used. In short, the RMSE measures the average magnitude of the difference between the two datasets. For a single vertex and layer the RMSE is expressed by the following equation:

$$RMSE = \sqrt{\sum_{i=1}^{N} \frac{(S_{Ri} - S_{VFi})^2}{N}}, \tag{2.16}$$

where S_{Ri} and S_{VFi} are the sensitivity values of the wavelength i for ray tracing and view factor, respectively. The variable N is the total number of wavelengths analyzed. The RMSE values for the 3 layers in the example above are shown in the following table:

Table 2.2: RMSE values per layer for the vertices discusses in Figure 2.6.

Vertex	**Layer**		
	Perovskite	Silicon	Total cell
$A_v = 0°$, $\alpha_v = 70°$ Figure 2.6a	0.006	0.006	0.010
$A_v = 0°$, $\alpha_v = 10.6°$ Figure 2.6b	0.036	0.036	0.063
$A_v = 9.2°$, $\alpha_v = 5.3°$ Figure 2.6c	0.100	0.100	0.173

For these examples, it is noticed that the RMSE value of each layer varies among vertices. Generally, the trend is that a vertex demonstrates a lower RMSE for each layer when it aligns more closely with the module position. For a specific vertex, perovskite and silicon layers exhibit the same RMSE. This pattern is observed across all the vertices. In addition, the RMSE of the total cells are smaller than the perovskite and silicon layers. This can be explained by the larger difference in sensitivity values for perovskite/silicon layers, as opposed to the total cell layer, particularly at the beginning and end of the wavelength range. **To consider whether the error for a vertex is high or small an error of 0.1 (10%) is set as a maximum acceptable value.**

The preceding example highlighted the behavior of three specific vertices. Figure 2.6c illustrates a vertex of extreme behavior, characterized by large RMSE. Conversely, Figure 2.6a showcases a vertex exhibiting ideal behavior, with a significantly small RMSE. Figure 2.6b represents an intermediate case. To get an idea of the

broader picture, Figure 2.7 represents the RMSE values for the same module orientation ($A_M = 0°$, $\theta_M = 30°$) for all "important" vertices.

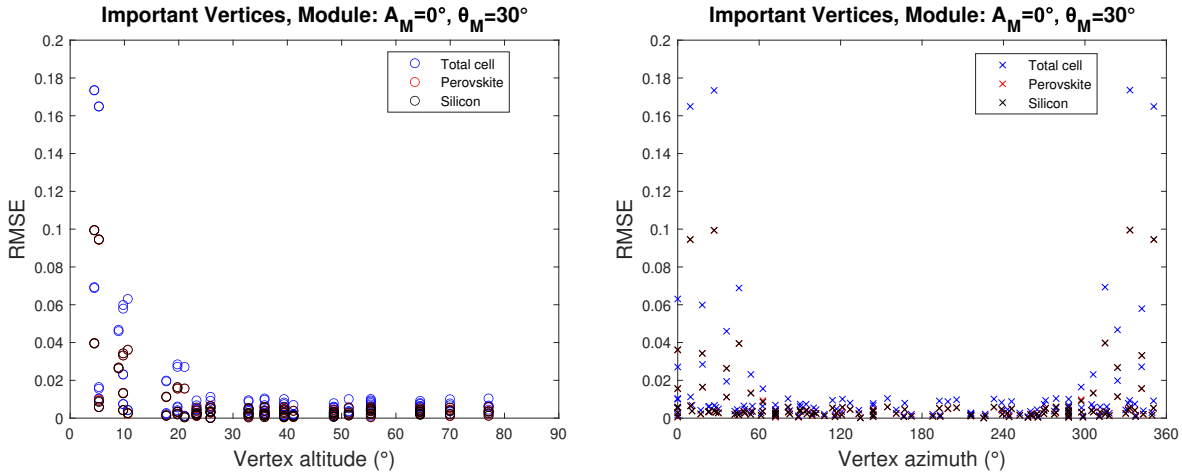

(a) (b)

Figure 2.7: RMSE values of the important vertices for the three layers for the same example discussed in Figure 2.6. Here, "important" refers to those vertices that have non-zero sensitivity values for both methods.

In Figure 2.7, it should be noted that vertices that reach the back of the module, such as those located north or/and at low altitudes, have been excluded. These vertices have zero sensitivity and therefore do not contribute to the irradiance calculation. The graph illustrates that the majority of the vertices are concentrated within an error range of 0 to 0.02. Nonetheless, there are four vertices ($A_v = 9.2°$ & $\alpha_v = 5.3°$, $A_v = 350.8°$ & $\alpha_v = 5.3°$, $A_v = 333.2°$ & $\alpha_v = 4.4°$, $A_v = 26.8°$ & $\alpha_v = 4.4°$) which exhibit the highest error ranging between 0.16 and 0.18. **These vertices, characterized by low altitudes range of $4° - 6°$, are henceforth referred to as outlying vertices.** The source of their deviation will be further examined in below. Moreover, it is noticeable that a significant portion of vertices with the highest RMSE values have altitudes below 10°.

In general, a small RMSE value indicates a smaller average difference between the S_{VF} and S_R values, suggesting a closer match between the two methods. In this case, except for the four outliers, most of the important vertices have an error below 0.1, which stands as the acceptable upper limit. This implies that the view factor method provides sensitivity values relatively close to those obtained from ray tracing. To further generalize this, the mean RMSE values of all vertices for the 3 layers are calculated in Table 2.3.

Table 2.3: Mean RMSE values of all vertices for the three layers of a single module orientation (example of Figure 2.6).

Layers	Mean RMSE
Total Cell	0.012
Perovskite	0.007
Silicon	0.007

The mean RMSE values shown here, are well below 0.1, once again confirming that the view factor method can fairly provide similar results with ray tracing. Finally, it should be pointed out that these results are specific to a particular module orientation and an albedo value of 0.2.

Outlying Veritices

This term was introduced above and concerns vertices that exhibit significantly higher error in relation to the majority of the vertices. It was found that regardless of the module's tilt angle, the vertices showing this behavior have altitudes ranging between 4° and 6°. This behaviour can be explained by the effect of surrounding modules as illustrated in Figure 2.8.

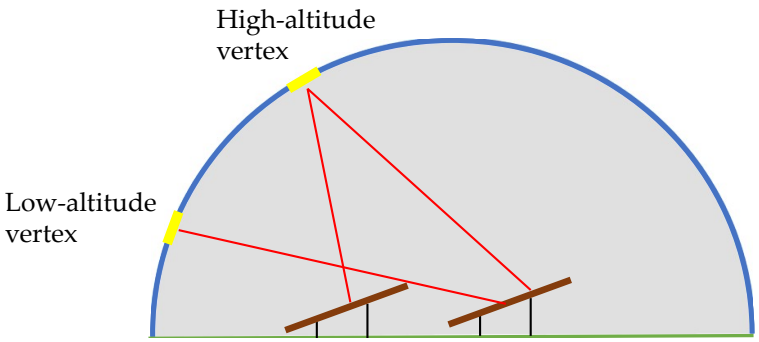

Figure 2.8: Illustration of light coming from high-and low-altitude vertices in the skydome

When LUX (ray-tracing) software computes the sensitivity values, it considers modules structured in an infinite number of arrays with infinite length. In Figure 2.8, two arrays of modules are shown. Light from a vertex that is high in the skydome can easily reach both module arrays. However, for vertices with low altitudes and especially those at 4° and 6°, the effect of the front arrays is taken into account, obstructing the light from reaching the second array, thus rendering these vertices less sensitive. In the view factor model, where the modules stand alone, this effect is neglected, and low-latitude vertices appear more "sensitive" (see Figure 2.6c), thereby increasing the error of the two methods.

2.4.3 Effect of albedo and module tilt angle

In this section, the comparison between the two methods is conducted across different module tilt angles and albedo values. The process described earlier is repeated for multiple tilt angles, ranging from 0° to 50°, while keeping A_M fixed. The RMSE values for all vertices and layers are calculated, and the mean RMSE values are determined. The results for a fixed azimuth and varying module tilt positions are presented in Figure 2.9.

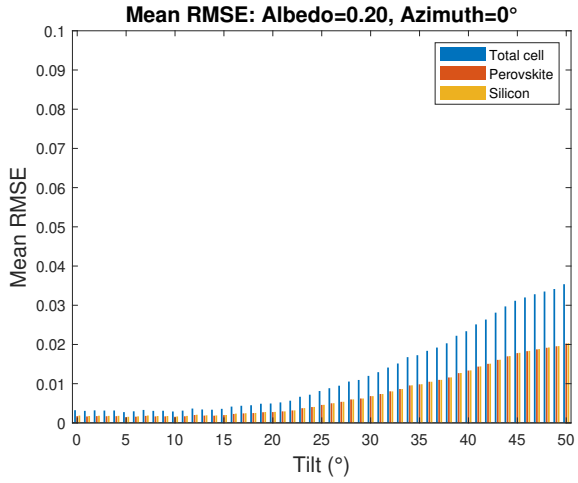

(a)

Figure 2.9: Effect of the module tilt in the mean RMSE for sensitivity values calculated with the two methods. For each graph, the module azimuth is constant, and the tilt angle varies.

It is observed that for low-tilt angles, the error between the two methods is negligible. As the tilt angle exceeds approximately 20°, the average error for all layers slightly increases with the growing tilt. One possible explanation of this behavior lies in the different approaches used to calculate the sensitivity related to reflected irradiance in the view factor and ray tracing models. With an increase in tilt angle (up to a certain point), the module becomes more exposed to ground-reflected irradiance, and, thus, more "sensitive" to it. The simplified approach used in the view factor model captures only the rays that are mirror-reflected from the ground. This approach is sufficient at lower angles but overlooks a bigger portion of irradiance reflected at varied angles from the ground as the tilt increases. In contrast, ray tracing can trace rays reflected from the ground across diverse directions that eventually reach the module. Thus, the different between the two methods increases as the tilt grows.

Another possible reason involves the assumptions used by the two methods. As stated before, the view factor model assumes the model stands alone in an open field, while LUX software considers the effects of the surrounding modules. With an increasing tilt angle, the shadow effects between arrays of modules become more prominent and influence the sensitivity values. With the view factor model neglecting these effects, the mean RMSE between the methods may increase, especially for higher tilts.

Finally, the magnitude of the error is investigated when the module is placed on a ground material with a higher albedo. Figure 2.10 depicts the mean RMSE when transitioning form an albedo of 0.2 to 0.4. It should be underlined that the albedo in both methods is constant and not wavelength-dependent.

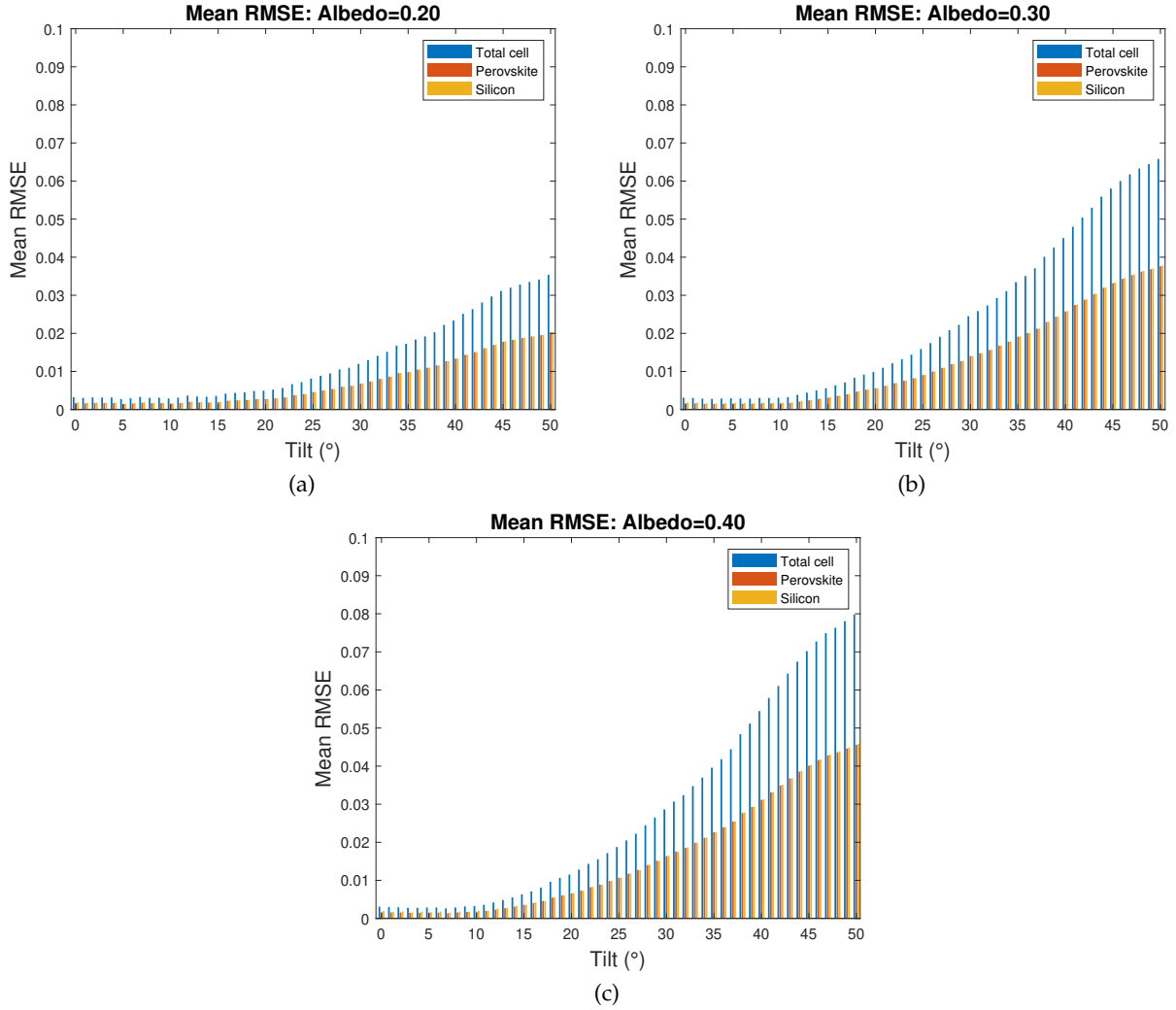

Figure 2.10: Effect of albedo in the mean RMSE for sensitivity values calculated with the two methods. The module is facing south.

It can be seen that the error is increasing with an albedo increase. A potential explanation for this occurrence is similar to the effect of the tilt. A surface with higher albedo implies a greater amount of reflected irradiance. The vertices accounting for most of the reflected irradiance are located in low-altitudes, since these do not have direct contact with the module. When LUX considers the surrounding modules, a fraction of the additional irradiance may be blocked from the front rows. Given that the view factor model doesn't account for this, the difference between them increases with albedo rise.

Overall, when varying the tilt of the module and the albedo, it was found that the mean RMSE value between the two methods does not exceed 0.1, a margin set as an acceptable limit. This entails that the view factor model can predict sensitivity values that, on average, closely align with those determined through the more complex ray-tracing method.

2.5 Conclusion

In this chapter, a new method for determining sensitivity, called the view factor sensitivity S_{VF}, was introduced. The proposed method splits the sensitivity into two terms: a direct/diffuse and a reflected component. The calculation is based on combining the EQE for three cell layers and the AOI, between each vertex of the skydome and the module surface normal. Goal of the new approach is the determination of sensitivity faster than ray-tracing, and more precisely at a time less than 1s per module orientation, as this will enable the inclusion of a tracking model in the toolbox. Results showed that the view factor method completes calculations at 0.1 seconds on average while ray tracing needs over 12 minutes. Subsequently, the difference in sensitivity values produced by the two methods was compared, when increasing module tilt and albedo values, using the mean RMSE of all vertices as a metric. While the mean RMSE showed a slight increase with increasing tilt and albedo, the mean error remained below the acceptable error of 0.1, indicating small deviations between the methods. By replacing ray tracing with the view factor model, the computational time was greatly improved, falling under the established threshold. Moreover, the results are closely aligned with those of ray tracing. With these outcomes, the second sub-objective of this thesis is achieved.

Chapter 3

Maximizing the Absorbed Irradiance: An Optimization Model

The first part of the tracking model we build is to substitute the time-consuming ray tracing method with a faster approach based on view factors and redefine the sensitivity concept. **In the subsequent steps, the new sensitivity values are employed in the calculation of the absorbed irradiance for all possible module configurations**. The second part of this model involves the core aspect of solar tracking logic: an optimization problem of locating the orientation that maximizes the absorption. To solve it, the applications of machine learning are explored, specifically the optimization algorithms. In Section 3.1 the optimzation problem is formulated, followed by the optimizations case studies in Section 3.2. Then, Section 3.3 introduces the selected algorithms for addressing this problem, and Section 3.4 provides a comparative analysis. Ultimately, given the algorithm selection per optimization case, the control strategy of the tracking model is discussed in Section 3.6, accounting also for the tracker's self-consumption (Section 3.5).

3.1 Problem formulation

The first step in any optimization problem is to formulate it mathematically. In essence, this problem aims to find the optimal module position expressed by its azimuth and tilt angle for maximum yield production. **This is equivalent to finding the optimal orientation that results in the maximum amount of absorbed irradiance as computed in the toolbox's weather block**. Therefore, the optimization process involves again the first three toolbox models. The absorbed irradiance , as calculated in the weather block, can be expressed as follows:

$$Abs = B_i \cdot S_{VF}, \tag{3.1}$$

where Abs is the module/cell absorbed irradiance (Wh/m^2), B_i the spectrally resolved incoming irradiance, and S_{VF} the new sensitivity values as computed by Equation 2.12. To be more precise, the complete irradiance absorption of the cell is maximized and thus the S_{VF} values of the total cell (1-reflection) are used. Then the problem can be described in the following way:

$$\begin{aligned} \underset{azim,tilt}{\text{maximize}} \quad & Abs\,(azim, tilt) = B_i \cdot S_{VF}\,(:, 1, :, azim, tilt) \\ \text{subject to:} \quad & azim \in \mathbb{Z}, \quad 0 \leq azim \leq 359 \\ & tilt \in \mathbb{Z}, \quad 0 \leq tilt \leq 90 \end{aligned} \tag{3.2}$$

The objective function is the absorbed irradiance, while the design variables are the azimuth and tilt of the module, which are set to take only positive integer values within that range. The columns in S_{VF} denote the other non-optimized variables of sensitivity and number 1 refers to the S_{VF} of the total cell layer which is stored in the first index of the S_{VF} matrix. The optimization is performed with a time resolution of one hour. Note that the sensitivity values remain constant over time, unlike the time-dependent nature of B_i. Thus, the optimization at hand is classified as an integer nonlinear programming problem.

3.2 Optimization case studies

To get an indication of how the absorbed irradiance profile looks like for various orientations in a day, Figure 3.1 is shown. To be consistent with the toolbox convention, the azimuth is depicted in the range of

0° to 360° with S=0°, W=90°, N=180°, E=270°. Mind also that this and the subsequent irradiance maps are generated for an albedo value of 0.2.

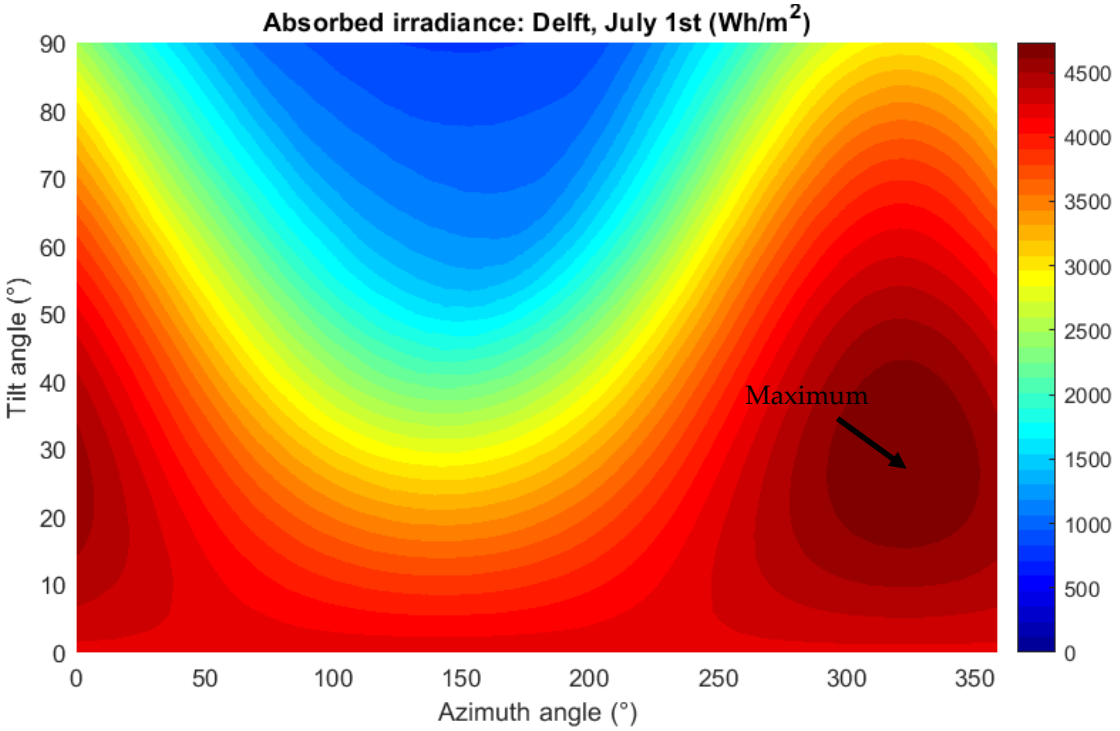

Figure 3.1: Absorbed irradiance profile in Delft July 1st.

The graph clearly indicates a daily optimum at an azimuth of 344° and a tilt angle of 29°, with a corresponding value of 4733 Wh/m^2. The irradiance absorbed suggests that the majority of the hours of this day were sunny, and apparently, as Delft is in the northern hemisphere, irradiance will reach higher levels in the southern direction. Notice that the graph is produced after running the Weather model and calculating the irradiance for all possible combinations of azimuth and tilt. Visualizing these results makes the optimum configuration readily apparent in this case. Generating these outcomes, though, is time-consuming. It takes about four hours to generate the map for a day like Figure 3.1 and around 20 minutes to make similar maps for an hour. Hence, the goal is to find the maximum value without the need to create these maps. Instead, we should detect the optimal solution, with a small amount of computational time.

In this work, a different optimization problem has to be solved every hour, taking into account the varying weather conditions that result in different irradiance profiles. The optimization method and the algorithm's convergence ability are influenced by the various weather conditions encountered. To describe these weather conditions, we refer to the Global Horizontal Irradiance (GHI) and its components: the DNI and the DHI. Based on the relative magnitude of these components, three main optimization cases can be distinguished.

3.2.1 Sunny hour - clear maximum

In this case, the sky is free of clouds. During these hours, the DNI is significantly higher compared to the DHI. In this model, all hours in which $DNI > 2\,DHI$ are characterized as sunny hours. Figure 3.2 illustrates an example of the irradiance profile during such hours.

On July 1st at 13:00, the DNI and DHI values are recorded as 813 Wh/m^2 and 243 Wh/m^2, respectively. The predominantly clear sky conditions result in an irradiance profile that exhibits a prominent peak in the south-southwest direction, particularly for tilt angles ranging from 30° to 40°. This distinct profile facilitates a gradient-based optimization algorithm in reaching the optimal solution relatively quickly, thanks to the steeper gradient on this map. It is worth noting that the region encompassing Southwest, South, and Southeast directions, which exhibit significant irradiance, represents a single global maximum rather than two separate local maxima on opposite sides of the graph. This behavior arises due to the circular nature of the azimuth angle, which wraps around from 360 degrees back to 0 degrees, forming a continuous circular pattern. While this holds true in reality, it poses a potential challenge to the algorithm's convergence. The algorithm treats the start and end points of the azimuth as boundaries and may become trapped in a local

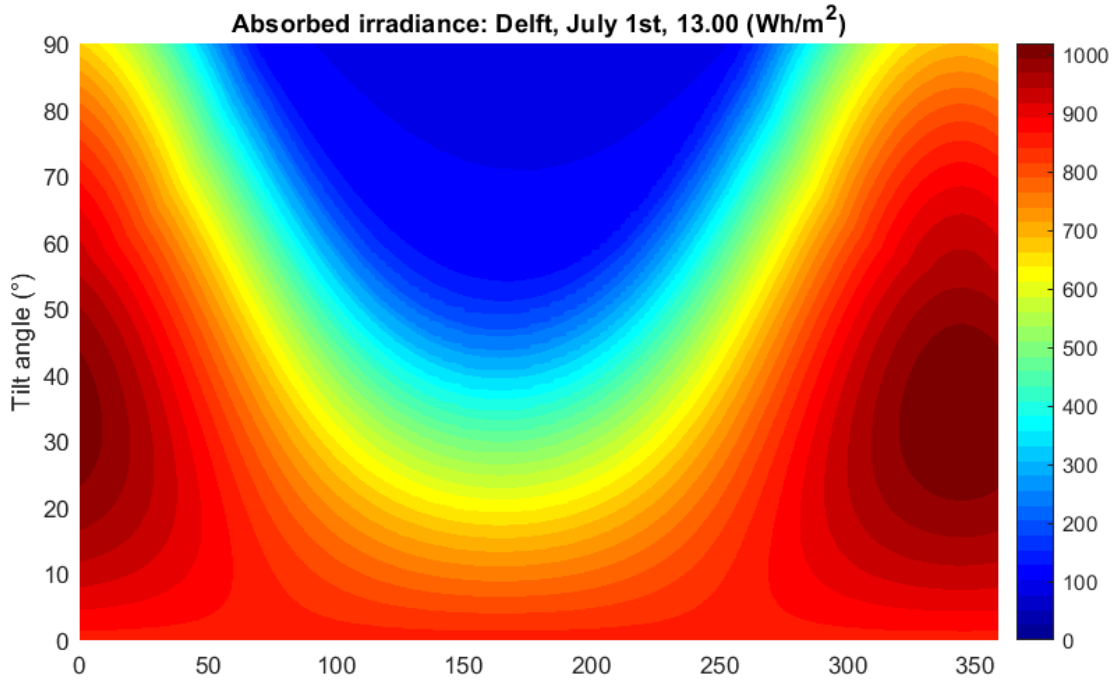

Figure 3.2: Absorbed irradiance profile in a sunny hour in Delft.

optimum because it struggles to transition to the other side where the global optimum lies.

3.2.2 Overcast hour - not clear maximum

During overcast hours, the sky is completely clouded, resulting in a uniform distribution of irradiance as depicted in Figure 3.3.

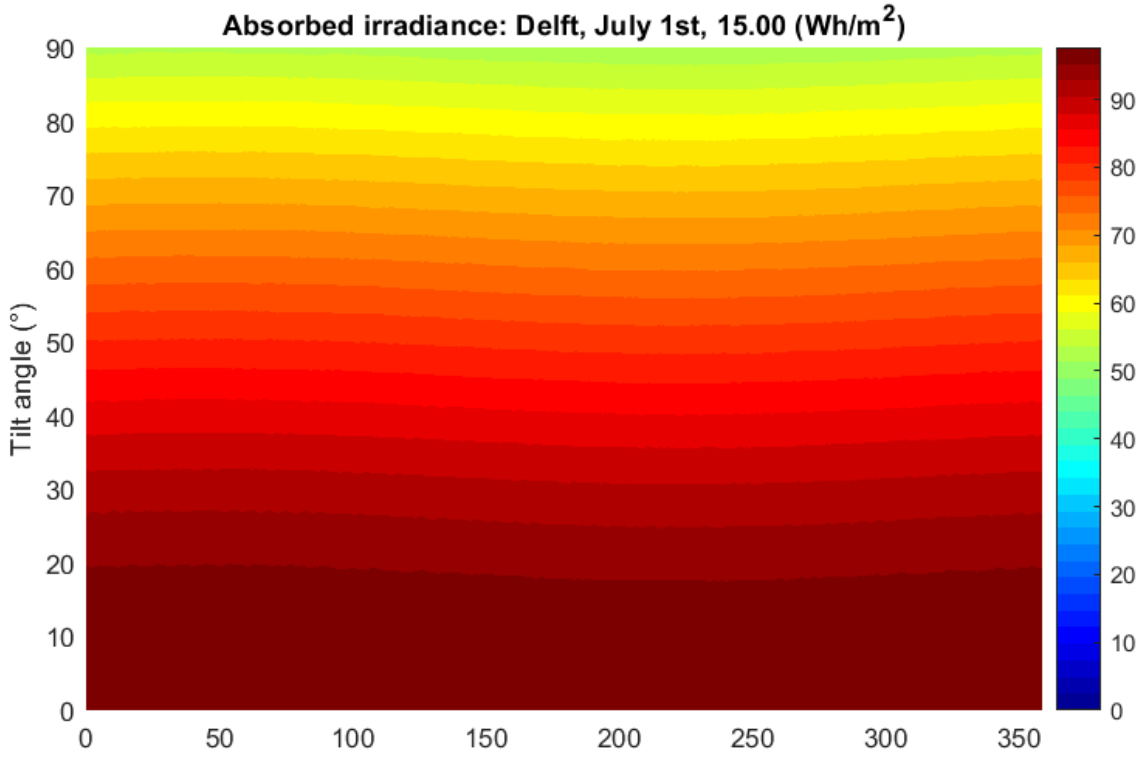

Figure 3.3: Absorbed irradiance profile in an overcast hour in Delft.

In this example, only the DHI value of 107 Wh/m^2 is present, while DNI is absent. As observed, for tilt angles below 20°, the irradiance values exhibit minimal variation across the entire range of azimuths. In other words, the irradiance values for different azimuths are very close to each other, leading to an azimuth-independent

irradiance. However, even in such cases, there is always a maximum irradiance value. Achieving convergence to the exact maximum of the objective function can be challenging due to the minor differences between adjacent values, often in the second or third decimal point. The algorithm may converge near the maximum irradiance value but with an azimuth angle that is far from the optimum, given the uniformly distributed irradiance across azimuths.

Finding the exact maximum irradiance and its corresponding coordinates requires more computational time, which is not practical when the differences between nearby values are minimal. Moreover, considering the energy required for panel rotation, it is not energy-efficient to rotate the panel from an overcast hour to the next overcast hour in pursuit of the last hour's optimum, especially when the energy gain is insignificant. In general, during overcast periods, it is recommended to position the panel horizontally, where the azimuth values become irrelevant azimuth and full advantage of DHI is taken [60]. The map here confirms that the optimum lies in small tilt angles but not necessarily on a flat alignment. In this model, hours where $DNI < 0.5\,DHI$ or DNI is non-existent are designated as overcast hours. Overall, optimizing performance during overcast hours presents a complex problem that necessitates a control strategy, as will be discussed further below.

3.2.3 Partially overcast hour - intermediate cases

The aforementioned scenarios represent the two extremes of sky conditions. Nevertheless, there are cases that fall in between these extremes, where both DNI and DHI are present and comparable. These intermediate conditions can be referred to as partially cloudy hours, encompassing all hours when $0.5\,DHI < DNI < 2\,DHI$. As a rule, the contribution of DNI in the irradiance profile is more pronounced than that of DHI's. When it dominates, it leads to a more distinct maximum in the irradiance profile like that of sunny hours. This characteristic facilitates a faster and smoother convergence of the algorithm. On the contrary, when DHI prevails, the profile tends to resemble the case of an overcast hour, posing a challenge for the algorithm to determine the optimum solution precisely.

3.3 Optimization algorithms

As mentioned previously, the process of constructing irradiance maps to identify the optimum is not a time-efficient approach, since it involves the examination of all possible orientations. This is where optimization algorithms step in, providing a more effective solution by evaluating specific points that facilitate faster convergence to the optimum. This study employs a combination of Matlab's and author-developed algorithms to deal with the optimization problem.

Matlab, as a sophisticated programming language, has introduced the Global Optimization Toolbox, offering a variety of solvers that utilize different optimization methods [61]. Some of these solvers were tested for their suitability to address the optimization problem at hand based on criteria shown in Table 3.1. To evaluate whether a solver accurately converges, the optimum value is obtained via the irradiance maps, as discussed before. It should be highlighted that this work qualitatively compares the Matlab solvers, rather than do a detailed analysis of each.

Table 3.1: Matlab's built-in optimization algorithms qualitative comparison.

			Convergence to optimum		
Algorithm	**Integer option**	**Initial guess requirement**	**Sunny hours**	**Intermediate Hours**	**Overcast hours**
Simplex (fminsearch)	No	Yes	Yes, when initial guess close to opt.	Yes, when initial guess close to opt.	Yes, when initial guess close to opt.
Surrogate	Yes	No	Yes	Yes	Yes
Pattern search	No	Yes	Yes, heavily relying on initial guess	Yes, heavily relying on initial guess	Yes, heavily relying on initial guess
Simulated annealing	No	Yes	Yes, heavily relying on initial guess	Yes, heavily relying on initial guess	Yes, heavily relying on initial guess

The primary drawbacks of algorithms such as fminsearch, pattern search, and simulated annealing are that they are not designed to work with integers and rely on an initial guess. While it is possible to force them to work with integers, by rounding the input values of the design variables, their convergence is not guaranteed. Upon testing, it was found that their convergence significantly depends on a carefully selected initial guess.

Often, these algorithms become trapped in local maxima and converge to the global when the initial guess is close to the optimum. Conversely, the surrogate optimization operates with integers, which is particularly relevant to the problem. Moreover, it does not necessarily require an initial guess to start the process, which significantly influences the convergence. After multiple tests in all three categories, it was proven to successfully locate the global optimum. Thus, it was chosen as the most suitable solver for the problem at hand and is further discussed below.

3.3.1 Surrogate optimization

Initially, a brief overview of the surrogate optimization working principle will be provided, specifically tailored to Matlab's surrogate model [61]. Generally, surrogate optimization aims to discover the global maximum of a time-consuming objective function by approximating it with a surrogate function that enables faster evaluation. The process consists of two primary phases: constructing the surrogate and searching for the minimum.

1. **Constructing the surrogate:** The algorithm initiates with this phase by generating random points within the problem's bounds, and evaluates the objective function at these points. It then utilizes these points to construct the surrogate function, which closely approximates the behavior of the objective function. To create the surrogate, various interpolation models can be used. In Matlab's toolbox, the algorithm utilizes a radial basis function interpolator [62]. Once the surrogate construction phase is complete, the algorithm proceeds to the next phase.

2. **Searching the minimum:** In this step, the algorithm samples thousands of random points within the bounds and evaluates the so-called merit function. The merit function combines two factors: the surrogate approximation on these sample points and their distances from all the points where the objective function has been previously evaluated. More details about the merit function can be found in [61]. The algorithm then identifies the point with the lowest merit function value as the adaptive point and evaluates the objective function at this location. Using this new information, the surrogate function is refined (phase 1) to better approximate the objective function, and the search process continues. Graphs illustrating the steps of each phase and the convergence procedure are provided in Figure 3.4.

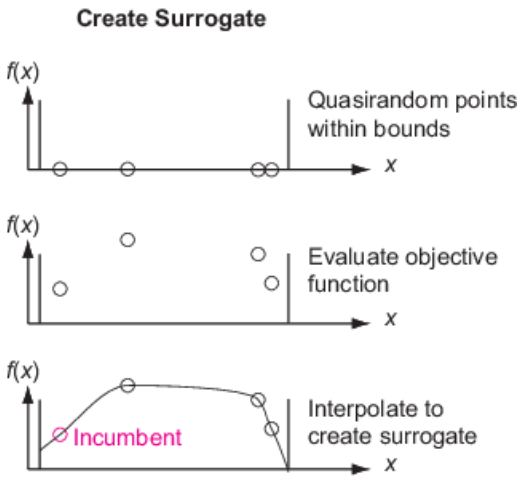

(a) Steps of constructing the surrogate phase. Incumbent refers to the point that exhibits the minimum objective function value out of all the assessed points since the most recent reset of the surrogate.

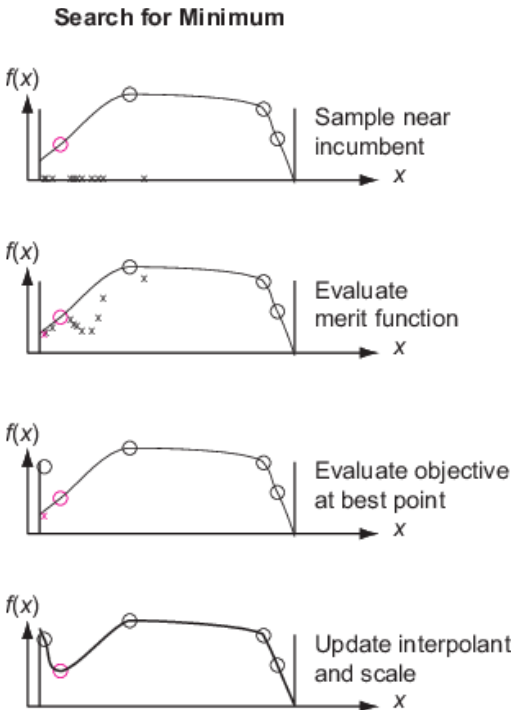

(b) Steps of searching for the minimum phase. The different sampling points where the merit function is evaluated, are represented by "x" symbols. The purple cross symbol indicates the best candidate point, also known as the adaptive point.

Figure 3.4: Surrogate's optimization phase visualization graphs. Graphs taken from [61].

The optimization process alternates between the two phases until one of the termination criteria (iterations number or time passed) is met. The lowest value at this point is regarded as the optimum. For this particular optimization problem, the iteration limit was chosen as a termination criteria.

The algorithm was evaluated under the different weather conditions outlined in Section 3.2. For all three hour-case studies, it was found that the algorithm is able to locate the global optimum. In addition, it was observed that fewer iterations are needed for sunny hours, a larger number for partially overcast hours, and even more in overcast conditions. However, it was decided to choose an overall iteration limit, that satisfies all cases. After several tests, it was proven that 80 iterations are adequate for the convergence of all three categories. Given that, the algorithm termination time on average for each case is depicted in Table 3.2. The differences are attributed to the different nature of optimization problems as described in Section 3.2. **In total, the most significant benefit of surrogate optimization is its ability to converge to the global optimum for all cases.**

Table 3.2: Performance of the surrogate optimization for the three hour-cases. Time is counted for a laptop: 2.8 GHz processor, 16 GB RAM.

Property	Sunny hours	Intermediate hours	Overcast hours
Time to terminate (80 iter.)	$\sim 0.8s$	$\sim 0.9s$	$\sim 1.1s$
Locates the global optimum?	Yes	Yes	Yes

Although the surrogate method can always locate the global optimum, the need to further reduce computation time prompts the exploration of new algorithms, such as the cross method, described below.

3.3.2 Cross method

The cross method is an author-developed algorithm made for the optimization problem at hand. The method derives its name from the way it examines the four neighboring points, forming a cross pattern. Consider the absorbed irradiance map shown in Figure 3.5. It is important to note that the design variables are integers with a step size of 1.

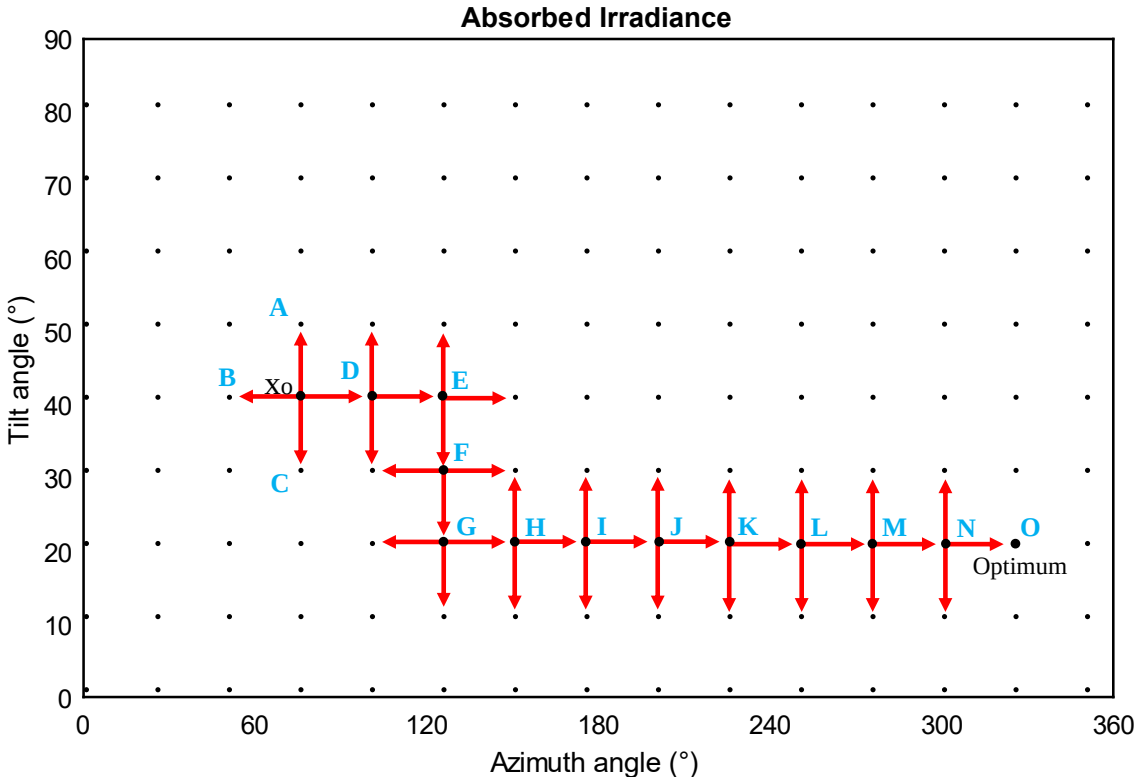

Figure 3.5: Example of the cross method convergence to the optimum.

The algorithm operates according to the following steps:

1. Let $X_o = [azim_o, titlt_o]$ be the initial guess for the azimuth and tilt. The algorithm computes the absorbed irradiance using Equation 3.2.

2. Proceed to evaluate the irradiance at the four neighboring points in each of the four cardinal directions, namely $X_o = [azim_o + 1, tilt_o]$, $[azim_o - 1, tilt_o]$, $[azim_o, tilt_o + 1]$, $[azim_o, tilt_o - 1]$. Determine the point with the highest irradiance among these neighbors and move to it.

3. Repeat the above step until you reach a point where none of the neighboring points exhibits a higher irradiance than the current point. At this stage, the algorithm exits the loop, considering the last current point as the optimal solution.

When the algorithm reaches either the rightmost side (azimuth = 0°) or the leftmost side (azimuth = 359°) of the graph, it encounters a boundary condition. To continue the search for the optimum, the algorithm is compelled to make a "jump" to the opposite side of the graph. In Figure 3.5, an illustration of the algorithm's operation is presented. The algorithm initiates from the initial guess X_o and evaluates the irradiance at the four neighboring points denoted as A, B, C, and D. Among these points, it identifies that point D exhibits the highest absorption, prompting the algorithm to move to that point. Subsequently, it progresses to point E and continues its exploration until reaching point O, which possesses the highest absorption compared to its neighboring points. At this point, the algorithm concludes its search, as it has found the optimal solution.

The performance of the cross-method varies across the three optimization case studies. However, one consistent aspect is the algorithm's swift termination, typically below 0.2 seconds for any given hour-case (laptop: 2.8 GHz processor, 16 GB RAM). Nonetheless, it does not guarantee reaching the global optimum in all situations. In particular, during sunny hours, the algorithm consistently converges to the global maximum, irrespective of the initial guess.

On the contrary, during overcast hours, the cross method fails to locate the exact optimal coordinates. This is explained by considering an irradiance profile similar to that in Figure 3.3. The algorithm starts from the initial guess and descends along the same azimuth until it reaches the tilt angle with the maximum irradiance, where it eventually halts. To put it differently, the algorithm does not move horizontally towards the global optimum due to neighboring points' similarity in irradiance values. The difference in irradiance between the local maxima, where the algorithm terminates, and the global maximum remains relatively small, with a maximum deviation observed at 2.2%. The difference, though, in the corresponding azimuth and tilt with the optimal values can be substantial.

For intermediate hours, the cross method often converges to the global optimum, although that depends on the initial guess. Once again, the deviation from the global maxima is less than 1.2%, and the corresponding design variables (azimuth and tilt) are closer to their optimal values. The better performance compared to overcast hours is a result of higher DNI present, which leads to a more distinct maximum in the irradiance profile that facilitates the algorithm to locate the optimum. In Table 3.3, the performance of the cross method in the three cases is summarized. A maximum termination time of 0.2s is shown, since the exact time depends on how far is the initial guess from the global optimum.

Table 3.3: Performance of the cross method for the three hour-cases. Time is counted for a laptop: 2.8 GHz processor, 16 GB RAM.

Property	**Sunny hours**	**Intermediate hours**	**Overcast hours**
Time to terminate	$< 0.2s$	$< 0.2s$	$< 0.2s$
Max deviation from global maximum	$< 10^{-4}$ %	1.2%	2.2%
Locates the global optimum?	Always	Most of the time	No

To summarize, despite its simplicity, the cross method offers the notable advantage of fast termination, outperforming surrogate optimization up to a factor of 4 for an optimization period of an hour. Its primary limitation lies in the overcast and partially cloudy cases, where the algorithm's convergence to the global optimum is not guaranteed. One may consider that these differences in absorbed irradiance, are relatively small for one hour and can be ignored. However, the accumulated loss due to an inaccurate panel position over the year should also be taken into account. In addition, not detecting the optimal position has an impact on the tracker's energy consumption.

In conclusion, it was found that the two algorithms perform differently for the hour-case studies. While the cross-method terminates fast but not with accuracy for all hour-cases, the surrogate optimizations consistently converge to the global optimum, albeit requiring more computational time.

3.4 Comparative algorithm analysis over an annual simulation

In the section above, the performance of both algorithms was explored on an hourly basis. Nevertheless, throughout the year, a mixture of the hour-case studies occur. Hence, in order to make a more informed decision on the final choice of algorithm, it is necessary to compare them over an annual simulation period, with the same criteria: the runtime and the convergence to the global optimum. In Table 3.4, the annual optimized absorbed irradiance is shown as the sum of the hourly optimized irradiance. In the cross-method, the optimal position from the previous hour was used as the initial guess for each subsequent hour. Of course, the runtime and annual irradiance depend on the number of sunny, overcast, and partially overcast hours annually, which in turn is location-specific. In the table below, the location of Delft was chosen. Note that the point here is not to look at the absolute numbers but to the relative difference between the algorithms.

Table 3.4: Annual simulation comparison: cross method against surrogate optimization. Time counted refers only to the optimization process. (laptop: 2.8 GHz processor, 16 GB RAM.)

Algorithm	**Time (min)**	**Absorbed Irradiance (kWh/m ^{2})**
I. Surrogate Optimization	$\sim 69min$	1591.5
II. Cross Method	$\sim 10min$	1575.5 (-1.02%)
III. Both methods Surrogate (sunny hours) Cross-method (intermediate + overcast hours)	$\sim 42min$	1589.9 (-0.11%)

As stated earlier, the surrogate method consistently converges to the global optimum for all case-hours. Thus, we consider this method's result the "accurate" standard to compare with the cross-method. Analogous to the optimization on hourly irradiance, on an annual basis, the selection between surrogate optimization and cross method can be seen as a trade-off between speed and convergence to the global maximum. The cross method terminates significantly faster but is 1.02% less accurate annually.

A third option is to combine the two algorithms, exploiting the advantages of each method on the respective case-hour. Therefore, the cross method is employed for the sunny hours and the surrogate method for intermediate and overcast hours. Results of the combined approach, are displayed in the third line of the table Table 3.4. It is shown that the both-method approach is a compromise in terms of time and accuracy compared to using only one of the two.

At this point, it is a matter of preference which of the three options to choose. It is the author's belief that losing roughly 1% of absorbed irradiance, by choosing only the cross method, is not worth the saving in time. In addition, losing only 0.11%, even though waiting more, is desirable. **In light of these, a compromised decision, weighted more towards accuracy is made and the both-method approach is selected.** This combination of algorithms is employed for the simulations to follow in Chapter 4.

3.5 Solar tracker self-consumption

A point overlooked while searching for the optimum orientation is the self-consumption of the tracker when it adjusts the panel. This energy needs to be subtracted from the overall yield to obtain the net energy gain. This section explains the selection process of a solar tracker and proposes a simplified expression to compute its energy consumption.

To select a suitable tracking mechanism, first, the degrees of freedom that dictate the movement capabilities of the solar panel should be determined. In this particular study, the objective is to construct a model for a dual-axis tracking system. In this system, the solar module can move along two dimensions: the horizontal (altitude-tilt) direction and the vertical (azimuth) direction. To link the design with the tracking techniques discussed in Section 1.3, the aim is to model a tip-tilt dual axis tracking configuration. In this regard, a dual-axis tracker mechanism primarily consists of the following mechanical parts [63]:

- Two shafts: altitude and azimuth shaft
- Altitude and azimuth gear trains
- Two DC motors, one for each dimension.

To calculate the overall energy consumption of the tracker during operation, the following equation is used:

$$E_{tracker} = P_{tracker} \cdot \eta_{tracker} \cdot \Delta t_{azim} + P_{tracker} \cdot \eta_{tracker} \cdot \Delta t_{elev} \tag{3.3}$$

where $P_{tracker}$ is the rated power of the DC motor and Δt_{azim} and Δt_{elev} denote the time required to displace the module along azimuth and elevation dimensions, respectively. Additionally, the symbol $\eta_{tracker}$ represents the overall efficiency of the tracker, which for simplicity, is assumed to be equal to the DC motor efficiency. Other losses, such as those associated with the motor's gearbox, copper, or iron losses, are excluded. The DC motors are powered by the module's energy. It is also assumed that the motors used in each direction are identical, having the same efficiency

The choice of the DC motor is based on the study of Guo et al. [64]. The authors employed a 15 W DC motor for a panel with a specified area and weight. To adapt this selection in this report, the motor's rated power is scaled up proportionally to the surface area and weight of the panel used in the toolbox. Hence, a 25 W DC motor is selected for each dimension of movement. It is assumed that the shaft maintains a constant angular speed of $0.3°/s$, with an efficiency of 95%. Furthermore, the angular displacement required to reach the next optimum orientation from the current position is obtained by the optimization algorithms. Using these parameters, the tracker's energy consumption can be computed by Equation 3.3.

Shifting the panel to its new position takes a minimal amount of time, with a maximum duration of 3 minutes, which is way shorter than the time during which the panel remains stationary (1 hour). Under these circumstances, the change in absorbed irradiance, while the module moves can be neglected. In essence, the Δt in the equation above serves to approximate the self-consumption, but for modeling purposes, the panel is assumed to move instantly. It is important to note that this approach is a simplified approximation. More information regarding the suitability of the DC motor can be found in Appendix A.

3.6 Control strategy

Efficient control of a PV system is crucial for maximizing energy production. In the proposed model, the control strategy considers both the algorithm choice based on the prevailing weather conditions and the energy consumption of the tracker. During sunny hours, self-consumption is significantly small compared to the energy gained. Yet, for two consecutive overcast hours, the irradiance profiles could be as such that there is a considerable difference between the optimum azimuth or tilt of the two hours, while the net energy gain is equal or higher for the first hour. In such situations, the panel remains fixed in the optimum position of the first hour because the self-consumption surpasses the net energy gain. Likewise, when confronted with 3 or more consecutive overcast hours, the algorithm always evaluates the net energy gain between the current and the next hour to determine whether or not to move. At the end of the day, when daylight diminishes, the panel moves to a horizontal position with the azimuth set to south for the northern hemisphere and north for the southern hemispher, in in preparation for the following day. In summary, Figure 3.6 visualizes the overall control strategy of the optimization problem discussed.

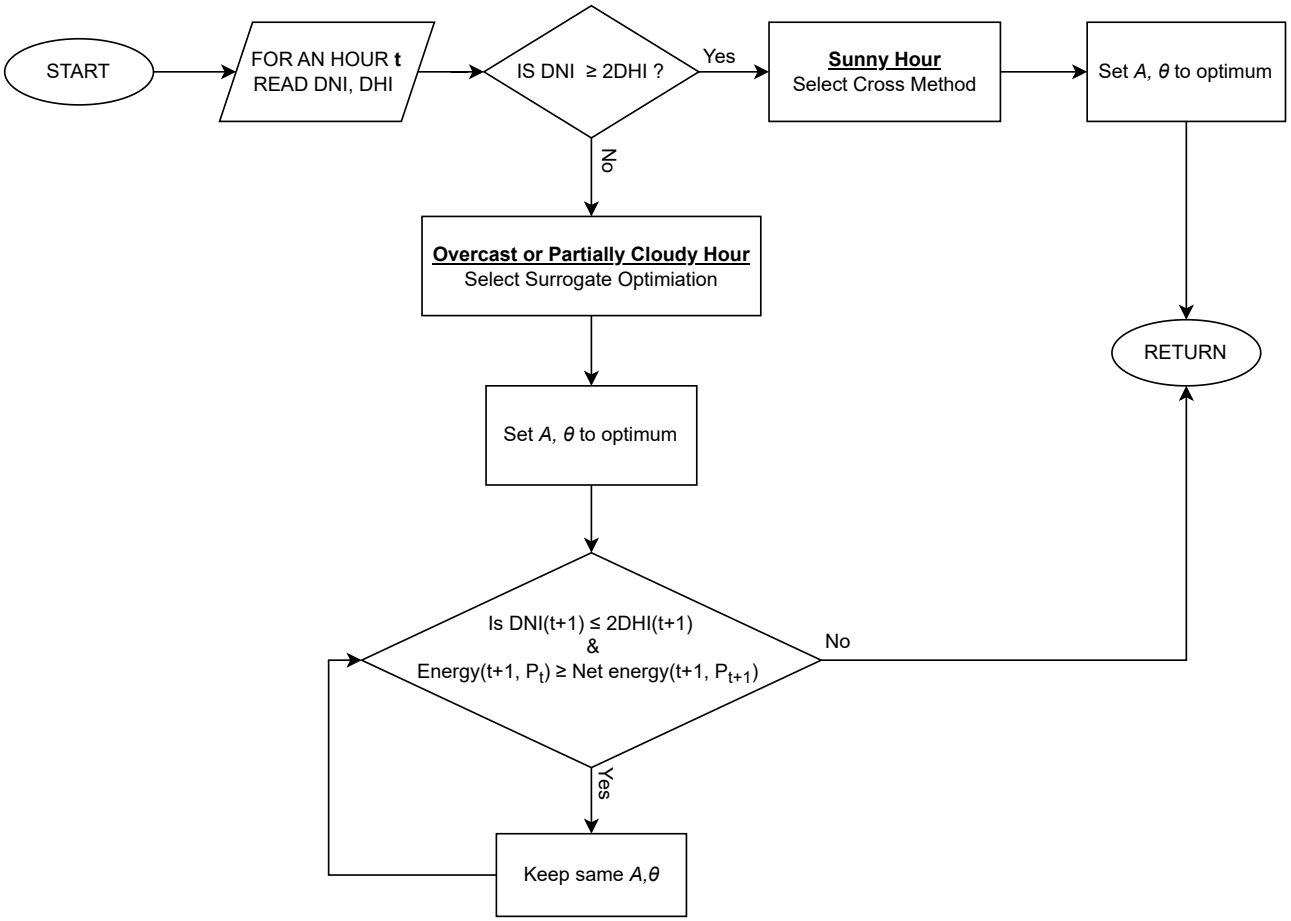

Figure 3.6: Flowchart of the control strategy of the optimization process. A and θ denote the module's azimuth and tilt angle, respectively. P_t and P_{t+1} refers to the optimal position at hour t and t+1, respectively

3.7 Conclusion

The second sub-objective of this thesis is to find the optimum algorithm(s) that maximize the absorbed irradiance. This chapter has presented various algorithms, offering a rationale to determine which is more suitable for addressing the optimization problem at hand. The various sky conditions that occur on each hour were grouped in three optimization case studies: sunny, partially overcast, and overcast hours, which exhibit different absorbed irradiance profiles. Among the algorithms tested, Matalb's surrogate solver and the author-developed cross-method were chosen for their compatibility and performance (time and accuracy). It was observed that for all three hourly-cases studies, surrogate optimization converges to the global optimum, but requires more time, while the cross-method, performs fast but accurately only for the sunny hours. Extending the optimization to an annual period, using only one of the two algorithms revealed that there is trade-off between accuracy (only surrogate) and time (only cross method). A compromised solution was chosen by selecting the cross method for sunny hours and the surrogate for overcast and intermediate hours. With this final choice, this chapter fulfilled the second sub-objective. In the next chapter, the overall tracking model is used to simulate dual-axis tracking tandem modules.

Chapter 4

Solar Tracking Under Real-World Conditions

Following the completion of the solar tracking model, it has been integrated into the toolbox to enable the prediction of the energy yield for tracking modules. This chapter presents the results of simulations performed for PST modules coupled with a dual-axis tracker at real operating conditions. To begin with, the input for toolbox simulations is provided in Section 4.1. The different climates selected are discussed in Section 4.2. Results on the energy performance of PST modules are outlined on three time bases: daily (Section 4.3), seasonal (Section 4.4), and annual (Section 4.5). This structural approach allows for the extraction of interesting findings across different periods. Ultimately, a comparison of the annual energy gain of SHJ modules of the same sub-cell with the PST modules is made in Section 4.6. The chapter closes with a brief conclusion of the findings (Section 4.7).

4.1 Input for toolbox simulations

Two important input parameters are described in this section. First and foremost, the characteristics of the cell technology used in simulations, followed by the toolbox models parameters chosen or assumptions made.

4.1.1 Modelled solar cell specifications

In this study, primarily a 2T Perovskite-silicon tandem cell is examined. The simulated cell is based on the work of Al-Ashouri et al [65]. Their work involved the construction of a monolithic perovskite/silicon 2T tandem solar cell, which demonstrated an efficiency of 29.15%. This reference cell has been implemented in the toolbox and validated optically and electrically. To ensure realistic simulations of solar modules, the original cell design was further modified as described by Vogt et al. [49]. The modifications involve the addition of an encapsulation layer and adjustments in the thickness of the absorber layers. The layers structure and thickness employed in the toolbox are derived from the study of Vogt et al. [49]. The layer structure of the perovskite-silicon tandem cell, along with the cell's electrical properties, is shown in Table 4.1. It is a monofacial 2T tandem cell where the silicon bottom cell features rear and front side texturing.

Table 4.1: 2T perovskite-silicon tandem cell specifications

(a) Layers structure

Layer	Thickness (μm)
AF2400	0.093
Porous glass ARC	0.053
Glass with iron (Fe2O3)	3200
Polyolefin-UVT	450
IZO	0.085
SnO2	0.005
C60	0.007
Perovskite 1.68 eV	0.575
PTAA	0.023
ITO	0.063
n-SiOx (n)	0.02
a-Si (i)	0.009
c-Si, bulk n-type	160
a-Si (i)	0.006
a-Si (p)	0.012
AZO	0.055
Ag	0.3

(b) Electrical characteristics per active area at STC

Parameter (STC)	Value	
	Perovskite	Silicon
Max. power P_{MPP}	187.12 W/m^2	112.31 W/m^2
Max. voltage V_{MPP}	1.06 V	0.62 V
Max. current density J_{MPP}	175.72 A/m^2	181.07 A/m^2
Efficiency	29.15%	
Module area	1.89 m^2	
Cells number	72	

4.1.2 Toolbox models input parameters

Table 4.2 provides an overview of the specifications for each toolbox block, which will be applied in the simulations to follow. These parameters remain consistent throughout all simulations unless stated otherwise.

Table 4.2: Input specifications for the Toolbox models

Toolbox model	Specifications
Cell	AOI angular intervals: 30
Module	Periodic Simulations View factor model for Sensitivity Average cell Sensitivity Albedo: 0.2 Module Area : 1.89 m^2 Number of cells: 72
Weather	Surrogate & Cross optimization method
Thermal	Cell efficiency for Temperature calculation: 0.25 Module Temperature coefficient: 0.003
Electric	Model cell parameters Non-reconfigurable modules Shading due to metalization: 2% Metal grid resistance: 0.0058 Ω
Conversion	1 string of 4 modules in series Central inverter: ABB: PVI 3.0 OUTD-S-US-Z-M-A (240 V) 240V [CEC 2014] Fixed cable losses: 0.5%

An assumption of the model is that the PV system is situated on a field with free horizon, indicating that there is no shading by surrounding objects or self-shading. Consequently, every cell within a module receives equal amount of irradiance and as a result there is no power mismatch between the modules.

4.2 Locations selection

The locations for PV modeling should be chosen in such a way as to enable meaningful comparisons regarding the impact of tracking on the energy yield. A hypothesis guiding the selection process suggests that the effect of solar tracking on energy gain is more pronounced at high altitudes, decreases at medium altitudes, and is relatively small near the equator. This hypothesis is derived from the sun's path across the year in the chosen locations. With the results obtained, this study aims to validate or reject this hypothesis.

In addition to this aim, another target is to capture a range of conditions, such as solar irradiance variations, temperature, and weather patterns, which significantly influence the module's performance. To achieve this, the climate classification scheme of KGPV is utilized [66]. This scheme divides the global climate into 12 zones with respect to temperature, precipitation, and irradiation. The KGPV classification map can be found in Appendix B. Altogether, four locations with descending altitudes and distinct climates are chosen, namely Stockholm, Athens, Bombay, and Bogota, some characteristics of each are displayed in Table 4.3.

Lastly, since solar tracking is examined, the sun's position throughout the year will help in interpreting some of the results presented later. In Figure 4.1, the sun paths of the four locations are depicted in polar charts. The radial direction corresponds to the sun's altitude while the angular to the sun's azimuth. The outer circle represents the horizon. The point where the sun enters and exits this circle every day corresponds to the sunset and sunrise, respectively. Over the course of a day, the sun moves on an arc-shaped line. Be aware that in the figure below, a different convention is used for the azimuth (N = 0°, E=90°, S=180°, and W=270°).

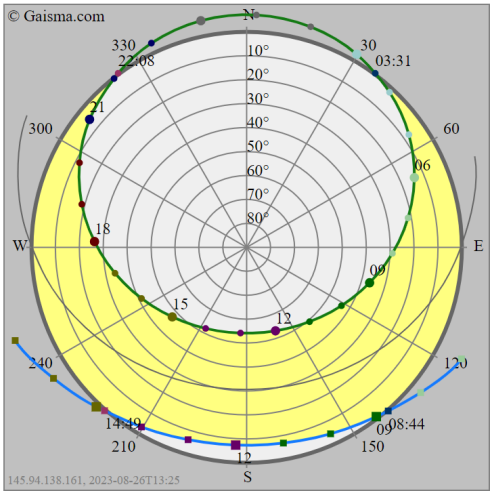

(a) Stockholm

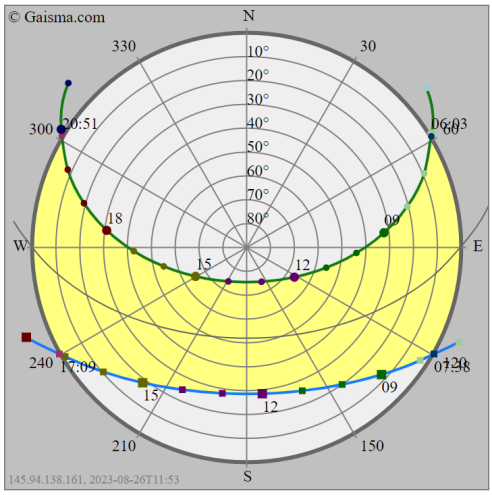

(b) Athens

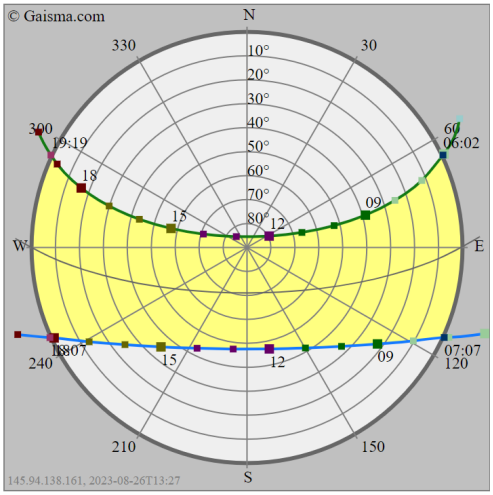

(c) Bombay

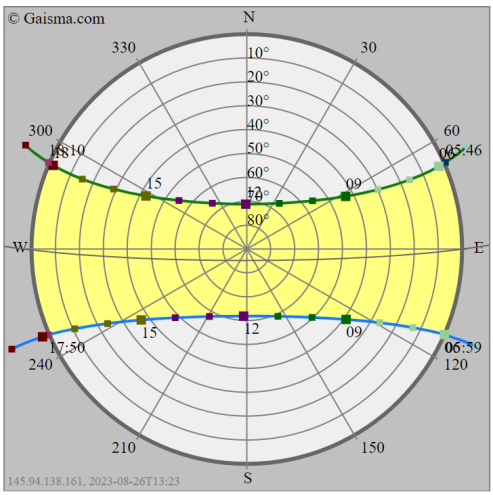

(d) Bogota

Figure 4.1: Sun paths of the four locations. The green and blue lines correspond to the sun's path at the summer and winter solstice, respectively (June 21st & December 21st). The yellow shaded area in between illustrates the annual variation of the sun's position. The light grey arc in the middle corresponds to the sun's trajectory at the equinoxes (March 21st & September 21st). Pictures are taken from [67].

Table 4.3: Locations data. GHI and optimum tilt data are taken from Meteonorm and PVsyst, respectively.

Location	Coordinates	Average GHI (kWh/m2/yr)	Equivalent Sun Hours (h/d)	Annual optimum tilt	Climate zone (KGPV)
Stockholm Sweeden	59.34 N 18.09 E	986.3	2.7	42°	Cold low irradiation
Athens Greece	38.00 N 23.73 E	1740.9	4.8	32°	Temperate high irradiation
Bombay India	18.99 N 23.73 E	2050.1	5.6	22°	Tropical high irradiation
Bogota Colombia	04.59 N 74.10 W	1781.2	4.9	7°	Tropical high irradiation

Before delving into the findings of this research, it is worth detailing how the results are grouped. Evidently, the primary advantage of a tracking compared to a fixed PV system is the increased energy production, referred to as the energy gain. Given that the energy output of PV systems exhibits diurnal and seasonal fluctuations, these variations similarly influence the energy gain. For a more comprehensive comparison of the two systems, it's important to demonstrate the energy gain time fluctuations. Therefore, the comparative performance assessment is conducted over three time-scales: the daily cycle, on a seasonal, and on an annual basis.

4.3 Results: daily PV system performance

This results section initially investigates the module orientation of the tracking PV system for days subject to various weather conditions. Following that, the energy output of the two systems is compared over a sunny day.

4.3.1 Daily optimal orientations

Figure 4.2 shows the optimal orientations of the 2-axis tracking system with respect to the sun position for the case of a sunny and cloudy day. The reader should know that Athens was taken as an example to demonstrate the module's movements, but similar conclusions can be drawn for other locations.

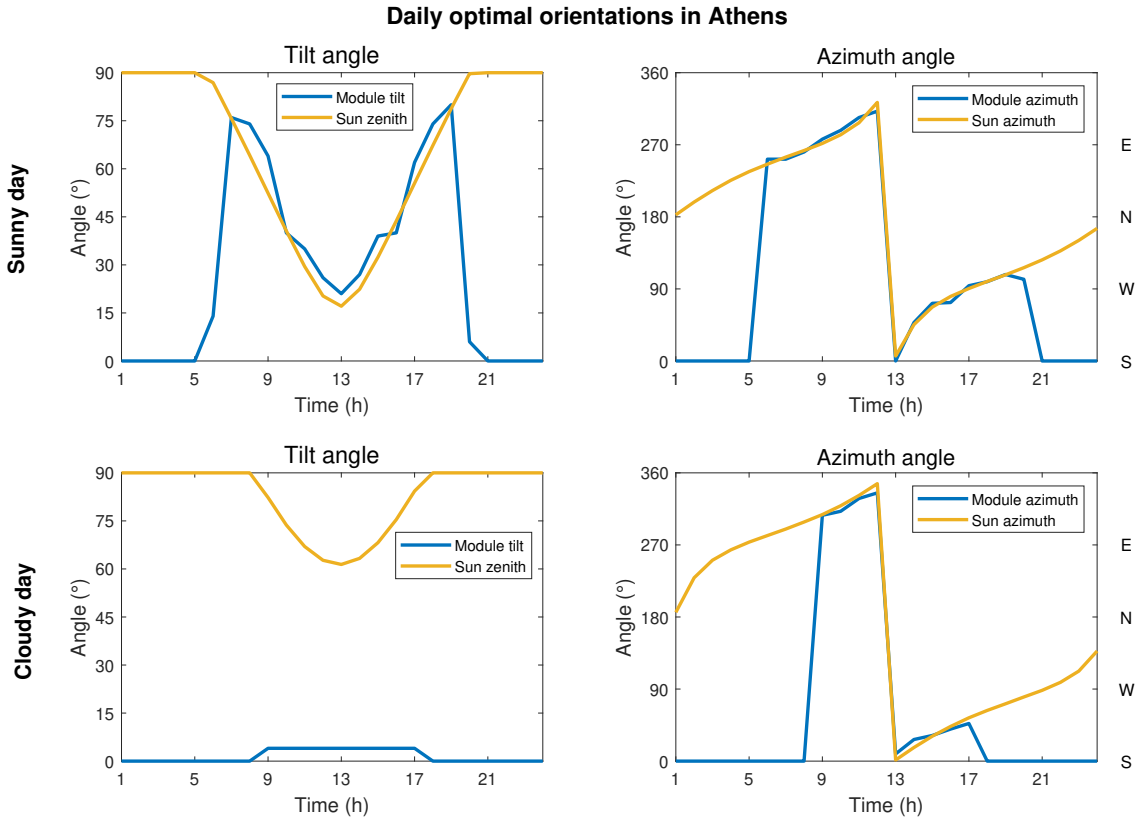

Figure 4.2: Optimal azimuth and tilt angle of 2T-tandem module for a day in Athens. The upper graph refers to the sunniest day (May 26), while the lower graph to the cloudiest day (December 23) of the year.

On a sunny day, the first daylight finds the module on a high tilt of about 75°, then decreases gradually until it reaches its lowest values at solar noon (hour of the day when the sun has the highest altitude). In the afternoon it rises back again, reaching a maximum value just before sunset. Note that in the absence of daylight, the module is preset on a zero tilt and zero (south) azimuth value. It can be seen that the module tilt follows the sun's zenith over the day. Early in the morning and late in the evening, when the sun is low on the horizon, the module aims for a steeper angle, to direct itself relative to the sun. The hour around the solar noun, when the sun is higher, the module comes with shallower angles. With respect to the module azimuth, it is observed that is almost equal to that of the sun over the day. **Mind that the sudden drop in azimuth represents the transition of the sun crossing from the south.** The module's behavior can be explained in the following way: On a sunny day, the DNI dominates and is the major contributor to the absorbed irradiance by the module. Hence, the tracking algorithm aims to extract as much as possible from the DNI, by exposing the module to direct sun's rays and thereby lowering the AOI. To do so, the module and sun azimuth should match, as this condition increases the received irradiance.

When the sky is heavily overcast, as is the case for the lower graph, the DHI prevails. As the graph shows, on such a day, the module remains relatively flat. This can be justified by the target to capture the greatest extent of DHI. Since the DHI does not have a specific direction but is rather random, a flat module can maximize the absorbed irradiance. Similarly to a sunny day, the module azimuth and the sun's are almost equal. The mismatch in the azimuth values can be attributed to the surrogate algorithm's possible failure to find the exact optimum azimuth value during overcast hours, but a value near it, due to a small iteration limit chosen. Nevertheless, it should be noted that when the module is relatively flat, the azimuth coordinate becomes irrelevant, with respect to the absorbed irradiance.

The third case is to examine the behaviour of the module on a partially cloudy day as depicted in Figure 4.3. The aim of this plot is to demonstrate the effect of the DNI component on the optimum tilt. On this day, from sunset till noon, the sky is overcast, while in the afternoon, the sky becomes clearer, as indicated by the presence of the DNI. While overcast, the optimum tilt is at almost zero degrees but from noon onwards, the module tilt surges to roughly 65° and then follows the sun's path. This behavior is in accordance with the two extremes showcased in Figure 4.2. Specifically, the first half of the day aligns well with a cloudy day, while the second half resembles the behavior of a sunny day. From this example, it can be deduced that even the presence of a small DNI amount lifts the module tilt up to values close to the sun's zenith at a given hour. Furthermore, it confirms the more prominent role, that DNI plays, as compared to DHI, in maximizing the absorbed irradiance by the module. This is evidenced by the fact that when the DNI emerges, with DHI also present, the module tends to orient itself directly toward the sun.

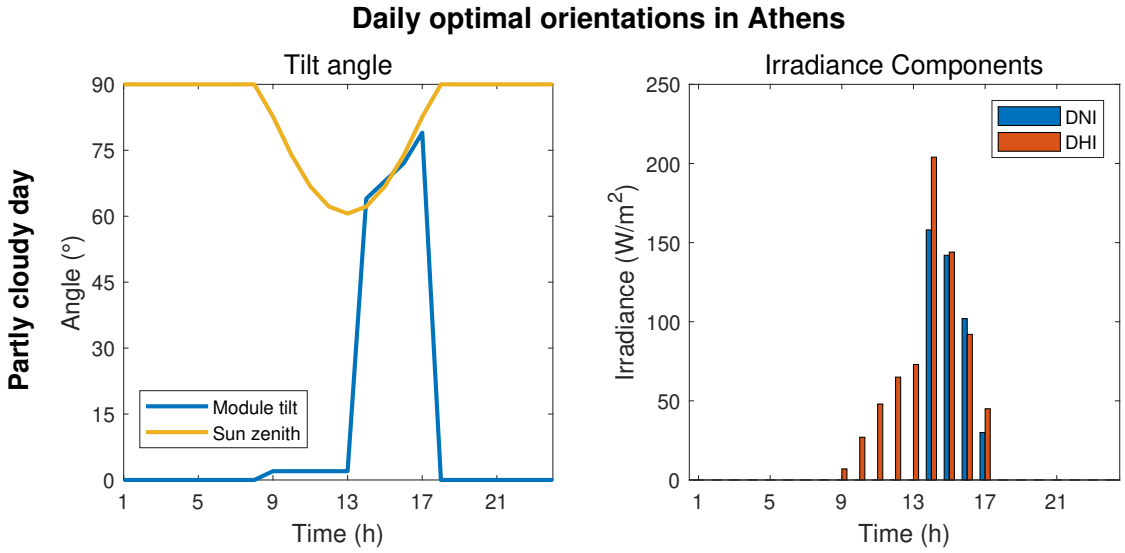

Figure 4.3: Optimal tilt angles and irradiance components of a 2T tandem module for a partly cloudy day in Athens (January 6).

Even though previously we categorize the days in sunny, cloudy, and partly cloudy days, to identify some trends, in reality, a day may consist of hours that are a mix of all these sky conditions. In that case, the existence of a relatively small amount of DNI shifts the module tilt up, closer to the sun's zenith of a given hour, whereas the presence of DHI pushes the tilt down to shallower angles. As a result, the daily optimum tilt angle will fluctuate over a day. An example of such a day is displayed in Figure 4.4. Overall, after

examining all cases, it can be concluded that the algorithm displays an enhanced sensitivity to DNI when determining the module's optimal tilt.

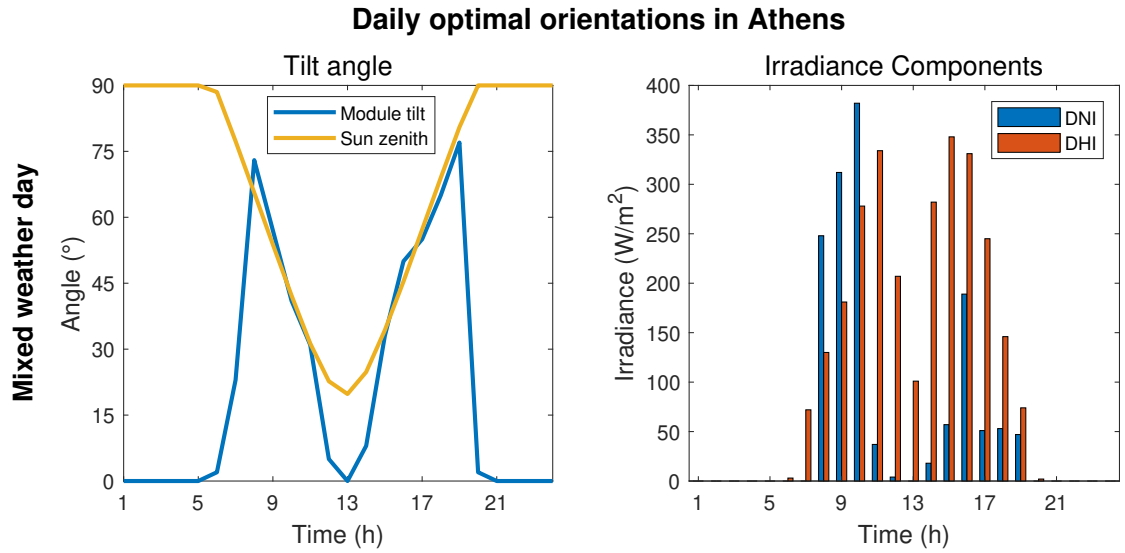

Figure 4.4: Optimal tilt angles and irradiance components of a 2T tandem module for a day with variable sky conditions in Athens (May 13).

4.3.2 Daily AC yield

The next step is to examine how the energy output is affected by the module's movements designed to track the sun throughout the day. Figure 4.5 compares the AC yield of 2T-tandem modules in a fixed and tracking system, using Athens on the sunniest day of the year, as an example. Again, the location is indicative, with the trends identified here being applicable to other locations. Note that the fixed PV systems are oriented in a southern direction and set at their annual optimum tilt, obtained by PVsyst software and validated with solar atlas [68], [44] (see Table 4.3).

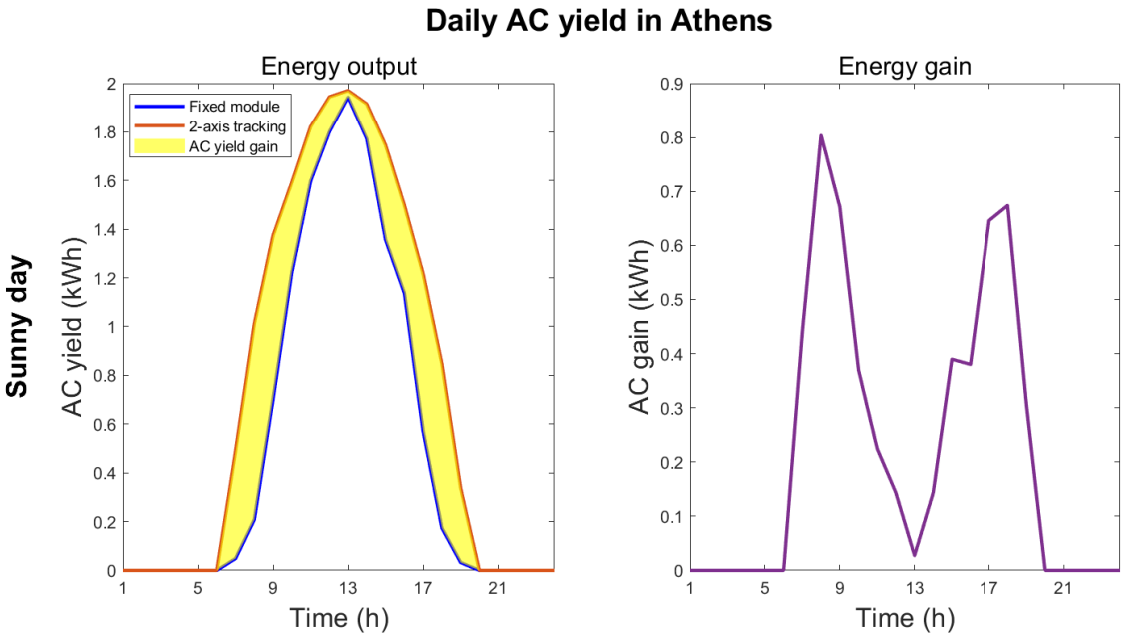

Figure 4.5: Comparison of the hourly AC yield and energy gain for the fixed and tracking PV system for the sunniest day in Athens (May 26).

At first glance, the tracking system consistently generates a higher yield than the fixed one, at almost every hour of the day. Evidently, on this sunny day, with the sky clear and the DNI prevailing, the tracking system is facing the sun directly most of the time (Figure 4.2), leading to enhanced absorption of irradiance. In turn, this leads to an increase in the DC and, subsequently, the AC yield. In total, a gain of 41.4% is achieved for this particular sunny day. Moreover, the tracker consumption for this day is 63 Wh, a quantity that can be neglected.

Table 4.4: Daily AC energy output of the two PV systems in Athens (Figure 4.5).

Yield fixed PV (kWh)	**Yield tracking PV (kWh)**	**Gain**
12.57	17.77	41.4 %

When examining it closer, it is observed that the AC gain occurs during the hours between morning and solar noon and from afternoon till the evening. On the contrary, the AC gain is minimized in the solar noon at 13 pm. In other words, the effect of tracking on the daily output is greater in the morning and the afternoon but less at noon. To explain this trend, the sun's relative position with respect to the module is considered, as this determines the AOI. As the sun rises from the east and sets in the west, the AOI for the static module (facing South) changes throughout the day. Owning to its fixed position the AOI is large in the morning and the evening enabling smaller capture of the DNI and an increase in reflection losses. In contrast, the tracking PV system keeps the AOI always minimal throughout the day, maximizing the DNI capture and therefore producing more yield. At noon when the sun is at its peak, the sun's rays hit the fixed module almost directly, resulting in the very small AOI, comparable to the AOI of the tracking system for that hour. Hence, both systems generate almost equal amounts at noon since they have the same optimal orientations at that moment.

The same behavior on the sunniest days is noticed in the other three locations. Figures referring to them can be seen in Appendix C.1. The daily relative gain on the sunniest days was found at 49.7% for Stockholm, at 44.9% for Bombay, and at 35.2% for Bogota.

The findings in Figure 4.5 exemplify that a peak in the energy output for any of the two systems at a given hour, does not necessarily mean a peak in the AC gain. To put it differently, a PV tracking system does not inherently create more energy. Instead, it exploits the available irradiance more effectively at specific periods of the day. As showcased before, these periods are the morning and afternoon till evening, but not the middle of the day. In simple terms, the peak in energy production on the left figure is broken into two peaks in terms of energy gain on the right one. With this in mind, tracking systems can become very beneficial in managing energy demand. The daily energy demand is usually high in the morning and late in the evening. As shown in Figure 4.5 the AC gain exhibits two peaks for the same periods, implying the usefulness of tracking systems in balancing supply and demand. Of course, that depends on the location, season, and sky conditions of the day. The above statement is just an indication valid mostly for sunny days. The contribution of tracking systems to the energy balance is a more complex topic, which needs further investigation.

Lastly, it is important to note that the daily AC gain depends on the hourly sky conditions. Similarly, with the energy output pattern, when clouds are present, the AC gain lessens in absolute terms, and fluctuates throughout a day, for which the sky clearness changes from hour to hour.

4.4 Results: seasonal PV system performance

Interesting conclusions can be drawn from the seasonal variations of the energy gain. Figure 4.6 depicts the absolute and relative gain in winter, spring, autumn and summer.

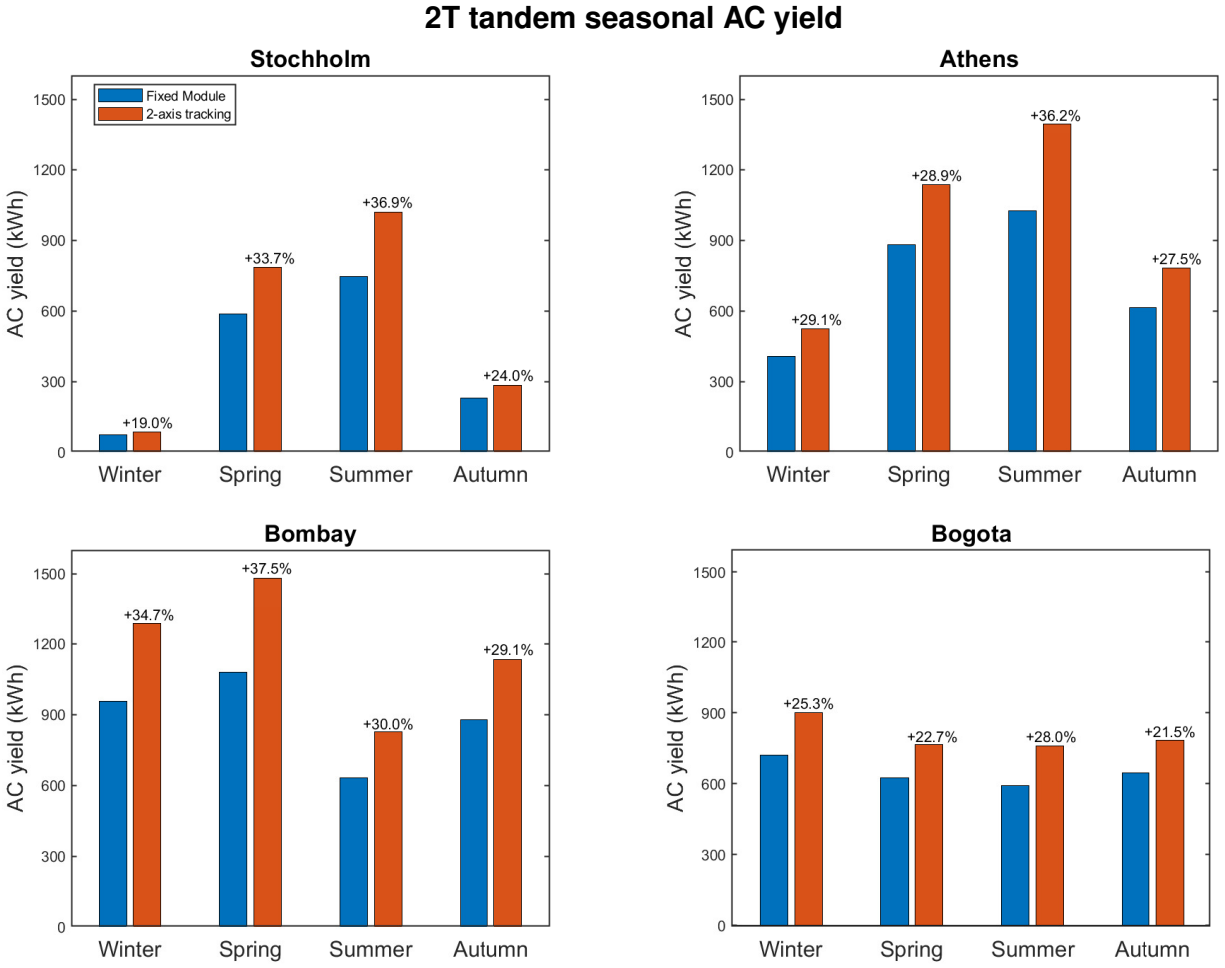

Figure 4.6: Seasonal AC gain for the two tracking systems in the four locations

The energy gain in Stockholm fluctuates between 19-36.9%, in Athens, spans from 27.5-36.2%, in Bombay from 30.0-37.5%, and in Bogota, it varies between 21.5-28.0%. In most locations, the peak in relative gain is reached in summer, except for Bombay, where it is observed in spring. To understand the seasonal changes in the energy gain, it is essential to consider the solar paths throughout the year for each location, as illustrated in Figure 4.1. In general, the further one moves from the equator (higher latitudes), the more pronounced the seasonal variability in the solar path becomes. The term ”variability” here refers to the shifts in daylight duration and the sun’s position in the sky. In Figure 4.1 that can be seen from the shape of the yellow-shaded area between the two solstices. From Figure 4.1a to Figure 4.1d (i.e. decreasing latitude), the area tends to have a more rectangular shape, which indicates a more consistent solar path over the year.

Stockholm exhibits the greatest variability in the sun’s path and, thus, is linked with the largest seasonal fluctuation in relative gain, spanning a range of 17.9 percentage units (from 19% to 36.9%). In areas with smaller latitudes, the range diminishes. Athens’s range is at 8.7 units and Bombay’s at 7.5 units. Bogota demonstrates the least variability and, therefore, the smallest range of 6.5 units. Besides, Bogota, due to its proximity to the equator (4.6°N), does not have seasons as people in the northern locations perceive them. That explains why the energy gain, absolute and relative, is very similar across all four seasons in Figure 4.1d. On the opposite side stands Stockholm (59.3°N), where the seasons are well-distinguished, in terms of daylight and irradiance levels, which explains the abrupt changes in seasonal relative gain compared to other locations.

4.5 Results: annual PV system performance

In this section, results on the annual performance of the system are presented. Initially, the energy gain is shown, followed by the computation of operational parameters over the year.

4.5.1 Annual energy yield

In Figure 4.7, the bar plot demonstrates the annual AC yield produced with both mechanisms in the four locations: Stockholm, Athens, Bombay, and Bogota. The relative AC gain is presented in Table 4.5.

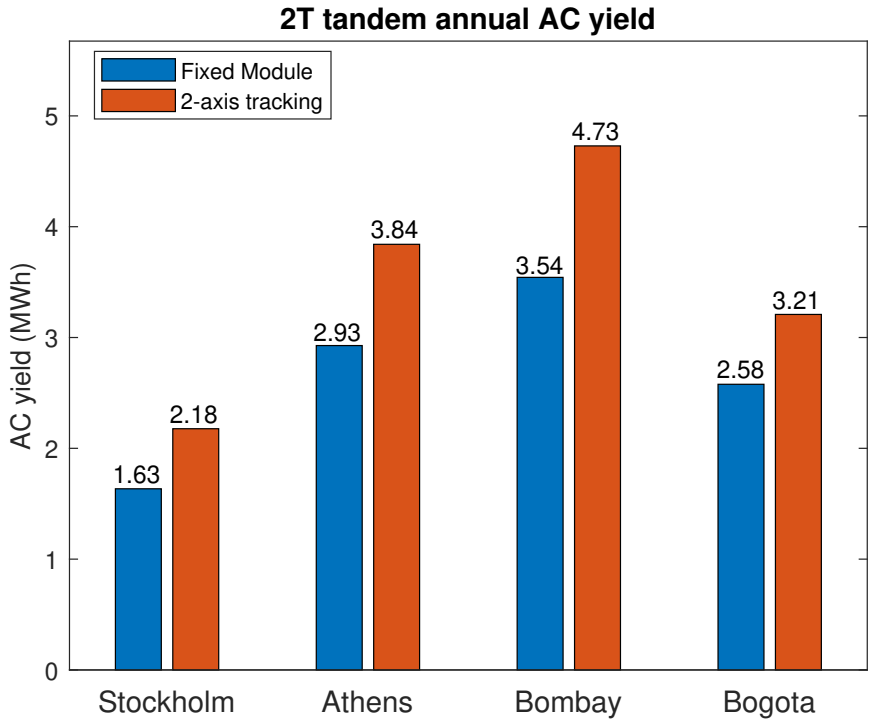

Figure 4.7: Annual AC yield produced for a 2T tandem module in the four locations. The energy output under a static and tracking topology is compared.

In absolute terms, the tracking topology shows the highest yield in Bombay, followed by Athens, Bogota, and Stockholm in descending order. The same sequence is observed for the fixed system. This order directly corresponds to the irradiation levels each location receives, as Table 4.3 highlights. Bombay's greatest AC yield can be attributed to the highest irradiation levels, while Stocklom's has the smallest yield since it experiences the lowest irradiation.

Table 4.5: Annual AC gain (%) for 2T tandem module in the four locations.

Location	AC gain (%)
Stockholm	34.0
Athens	31.9
Bombay	34.1
Bogota	24.8

Comparing the two topologies, it becomes clear that the dual-tracking mechanism outperforms the static modules across all locations on an annual basis. The AC gain in the selected locations spans from roughly 25% to 34%, with Stockholm and Bombay achieving the highest AC gain of about 34%, closely followed by Athens at 31.9%. In Bogota, the smallest AC gain is reached at 24.8%. Bogota's lower AC gain can be explained by the relative module and sun position in near-equatorial locations.

In Figure 4.1, it can be observed that Bogota has a smaller variation window for the sun's position over the year (yellow area) compared to the other regions with higher latitudes. On a typical day in an equatorial region, the sun rises steeply from the horizon, reaches the highest point at solar noon, and then descends steeply again. That implies that the sun spends most of the time in high altitudes, while in reality, it appears to be moving directly overhead. The same pattern, with small deviations in altitude, is followed for most of the days, as the narrow window in Figure 4.1d indicates. Conversely, in locations with high latitudes, the sun's path changes significantly between seasons. Therefore, the altitude change of the sun in Bogota is less pronounced compared to the northern locations. This probably explains the lower AC gain of almost 25% compared to Stockholm, Bombay, and Athens, which span from 32-34%.

Before performing the simulations, it was anticipated that while moving towards the equator (latitude decreases), the energy gain would similarly decline gradually. This assumption was based on the sun's path's prominent variability in northern regions throughout the year, as explained before. However, the results show that this trend is valid only for Bogota, in comparison with the other three locations. Stockholm, Athens, and Bombay, despite having latitudes that differ by approximately 20 degrees, displayed similar energy gains. Alkaff et al. studied the implementation of tracking topologies and, among those, a dual-axis tracker for various locations [69]. Similar ranges of energy gain were noted between the locations analyzed in this study and the sites with similar latitudes examined in Alkaff's work. However, in both of the works of Alkaff et al. and Bahrami et al., there is no clear relation between the locations' latitude above 19° (Bombay's latitude), and the respective relative AC gain [69, 70]. Other factors influencing the AC gain should be taken into account to derive a clear trend, such as the irradiation levels (direct to global and diffuse to global ratio) [71]. In the context of this present study, the analysis of merely four locations proves insufficient to discern a clear pattern. More locations are recommended to be examined for future research.

Furthermore, an important conclusion can be deduced from Figure 4.7. Regions with high latitudes, such as Stockholm (59.3°N), experience lower irradiance levels, which leads to a reduced PV potential. Nonetheless, applying solar tracking in these regions can raise the annual yield by up to 34%. This highlights the significant advantage of solar tracking, especially for areas at higher altitudes. Moroever, it can be concluded that while the annual absolute yield of the tracking is clearly influenced by the location's latitude (and other properties related to that, such as irradiation levels), the relative gain appears to not directly correlate with it.

4.5.2 Effect of tracking on cell temperature

Figure 4.8 compares the annual operating temperature of tracking and the static PV system. The temperature shown is the weighted average during the times the PV system is generating energy, calculated by the following formula:

$$T_{\text{weighted}} = \frac{\sum_i^T T_i P_i}{\sum_i^T P_i} \tag{4.1}$$

Findings reveal that the weighted temperature is 1.6-3.2° higher in tracking systems. The range of the temperature increase aligns well with findings from the literature [72]. Furthermore, it is observed that in hotter climates, such as Bombay, the operating temperature in tracking systems tends to increase more. The rise in temperature for tracking systems, compared to fixed ones, can be traced to their design principle to follow the direct component of the sun. Exposure to direct sunlight results in higher absorbed irradiance (Figure 4.9), leading ultimately to elevated operating temperatures.

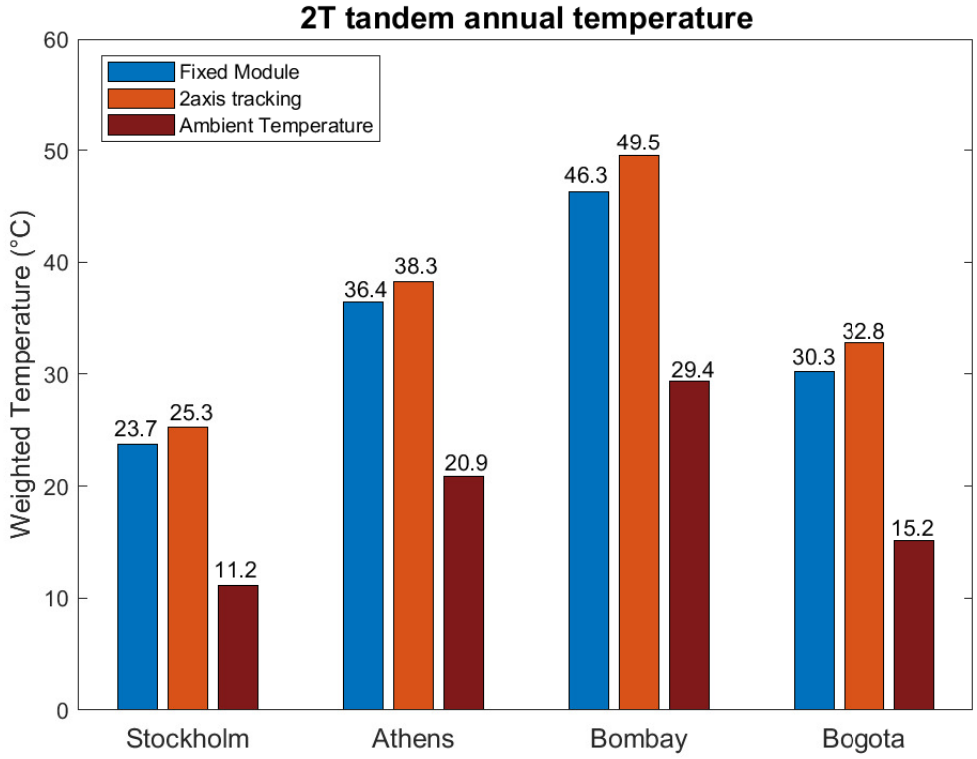

Figure 4.8: Annual weighted temperature of a 2T tandem module in the four locations for a static and tracking topology.

4.5.3 Annual irradiance gain - DC Gain - AC gain ratio

As already known, the module tracking systems receive an increasing amount of irradiance, the so-called absorbed irradiance gain. An important insight of this study is to examine how the relative irradiance gain translates into the DC gain and AC gain of the PV system. In Figure 4.9, the relative gain for the tracking system in 2T tandems is shown. Athens is taken as an example climate.

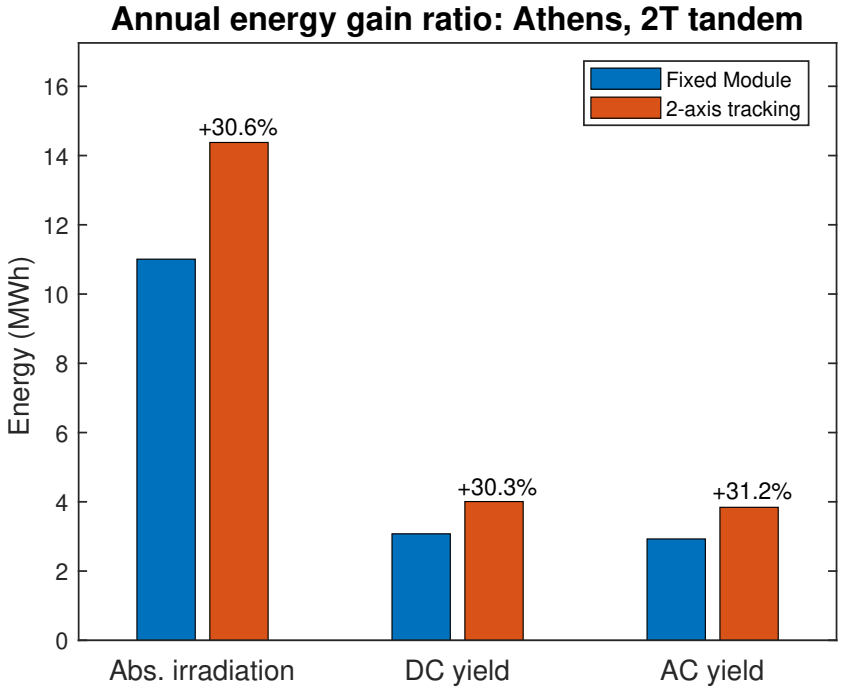

Figure 4.9: Annual gain in irradiance, DC and AC yield for the 2T tandem tracking system in Athens. Similar graphs and trends are observed for the other climates

The relative gain for absorbed irradiance, DC, and AC output was found at 30.6%, 30.3%, and 31.2%, respectively. It becomes clear that the gain is relatively the same across the three steps of power generation. In other words, it is shown that when applying tracking in PV farms, a certain increase in incoming irradiance will result in an equal enhancement of the energy power output. Thus, a direct proportionality is obtained between the gain in the absorbed irradiance, DC, and AC output with a ratio of 1:1:1. The reasoning behind this behavior is that the increased irradiance does not significantly disrupt the current matching between the cells that will subsequently cause power mismatch losses and finally a loss in the relative DC gain. This is more deeply discussed in the following section. It should be noted that the same ratio is observed in all other locations, but Athens was chosen as a representative example. Graphs for the other climates are shown in Appendix C.3.

Furthermore, the close DC and AC gain values indicate an efficient power conversion over the year. The slight increase from the DC to AC gain can be attributed to a small improvement in the inverter's efficiency. The increased DC input power to the inverter, as a result of the irradiance gain in tracking systems, leads to a slight increase in inverter efficiency [9]. Overall, the findings in Figure 4.9 illustrate the effectiveness of the tracking coupled with tandem cells to provide highly efficient PV systems.

At this stage, an interesting point to examine is the irradiance-to-energy relative gain ratio for a bifacial tandem cell and compare them with the tracking technology. Blom et al., using the PVMD toolbox, simulated the same 2T tandem cell but with bifacial features across multiple locations [73]. The results concerning absorbed irradiance and AC yield from their study are depicted in Figure 4.10.

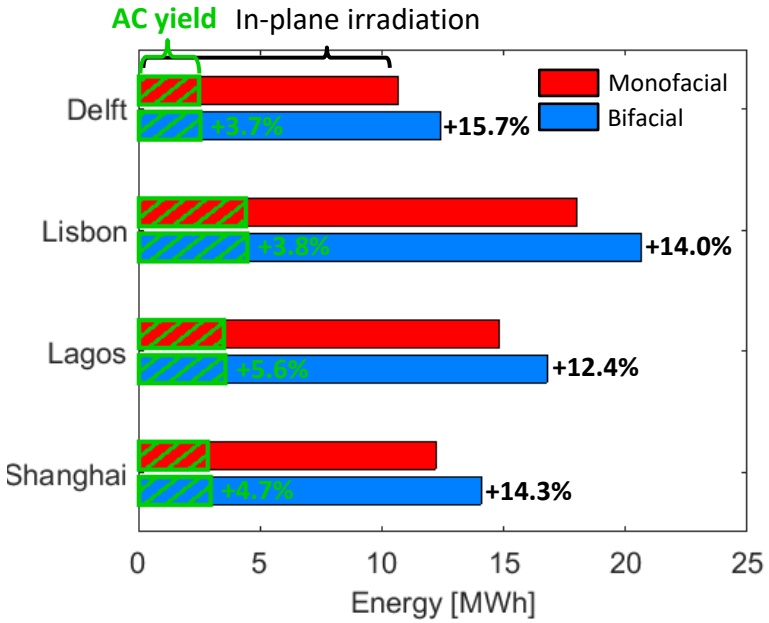

Figure 4.10: Selected results from the work of Blom et al. [73]. Comparison of thhe absorbed irradiance and the AC yield of the same tandem cell with bifacial features for different locations.

Their findings indicated that when compared with a monofacial module, a bifacial tandem exhibited a 12.4-15.7% rise in irradiance across multiple locations. Yet, this increase only translated to a modest AC yield growth of 3.7-5.6%, resulting in an average relative gain ratio of 1:3.3. The reduced AC gain was attributed to increased thermalization and mismatch losses, owing to the extra irradiation for the bottom cell. A comparison of the two ratios reveals that tracking technologies are more efficient in harvesting energy uniformly, from the absorbed irradiance to the AC yield, in contrast to the concept of bifaciality. The underlying reason is the lower mismatch losses in tracking tandem modules than in non-tracking bifacial tandems (Section 4.5.4).

Finally, given the results presented in this section, it is worth validating the tracking strategy to maximize the absorbed irradiance, instead of the DC/AC yield. The reason for not choosing to optimize the power output in the first place was the complex structure of the toolbox. Toolbox blocks are built in a serial way such that output from one block feeds into the next ones (Figure 1.11). In particular, to compute the DC output within the electric block, the module temperature -an output of the thermal block, is required. The temperature calculation, in turn, depends on the absorbed irradiance from the Weather module, which is a function of the module position. The latter determines the view factor sensitivity map obtained from the module block. The reader realizes that constructing a power profile map, equivalent to the irradiance profile

shown in Section 3.2, and moving across different points, by applying the algorithms, would involve iterative runs of all previous blocks. Eventually, such an approach would be not only computationally intensive but also present a programming challenge. Hence, the decision was made to optimize for irradiance, with the rationale that the orientation maximizing the absorbed irradiance, would maximize the power output as well. This rationale is validated by the results in Figure 4.9. It is proved that almost the same relative gain in irradiance is transferred to the DC and AC yield. This indicates that maximizing the absorbed irradiance would lead to almost the same results as maximizing the DC/ AC output. In retrospect, we proved that the initial choice was valid.

4.5.4 Effect of tracking on mismatch losses

As previously addressed, current matching is a crucial requirement for optimal operation of 2T tandem cells. When this condition is not met, the current of the tandem will be limited by the sub-cell with the lowest current. Eventually, the current mismatch will cause each cell to deliver power at a different maximum power point, limiting the overall tandem's power output. Hence, the current mismatch between the two cells will, in turn, trigger power mismatch losses. It is important to highlight that the current mismatch is increased in real-world conditions [74], as those explored in this chapter. This can be attributed to the spectral changes that frequently occur outdoors over time, which can introduce illumination conditions that result in different photo-generated currents in each cell.

Normally, an increase in absorbed irradiance due to tracking will boost the total photocurrent generated in the tandem cell. In this report, the focus lies on understanding how this increased irradiance is distributed in the two sub-cells and its effect the mismatch losses.

The mismatch losses can be quantified either by calculating the current or the power mismatch. On a tandem structure, the annual current mismatch ΔI is calculated as follows:

$$\Delta I_{annual} = \sum_{i}^{T} \frac{\left| I_{\text{ph,top},i} - I_{\text{ph,bot},i} \right|}{I_{\text{ph,bot},i}}, \tag{4.2}$$

where $I_{ph,top,i}$ and $I_{ph,bot,i}$ are the photo-generated currents of the top and bottom cells, respectively, on the hour i. The calculation is made for all daylight hours T of the year. Furthermore, the annual power mismatch losses are defined as the relative difference in annual power that a 2T tandem produces, with respect to the power produced when each cell operates at its maximum power point, as in a 4T configuration.

$$\Delta P_{annual} = \frac{P_{4T} - P_{2T}}{P_{4T}} \tag{4.3}$$

According to the literature ([74], [75]), while the current mismatch can be easier extracted from EQE measurements, the power mismatch serves as a better indicator for mismatch losses. The reason for this statement will be explained below. In Table 4.6, the mismatch losses for the two PV systems are displayed.

Table 4.6: Current and power mismatch losses

	System	Stockholm	Athens	Bombay	Bogota
Current mismatch losses (%)	Fixed	7.53	7.46	8.04	8.99
	2-axis tracking	8.10	7.64	8.29	8.88
Power mismatch losses (%)	Fixed	1.46	1.10	1.13	1.26
	2-axis tracking	1.77	1.29	1.37	1.36

Findings on Table 4.6 can provide some important insights. The first finding concerns the mismatch losses when transitioning from a fixed to a tracking system. The current mismatch of the fixed system spans between 7.46-8.99%, while for the tracking topology, it ranges between 7.64-8.88%. The comparison of the current mismatch across both PV systems reveals a small difference. As for the power mismatch, it ranges between 1.10-1.46% and 1.29-1.77% for the tracking and static topology, respectively. Once again, the difference between the two systems is equally trivial. In total, it can be concluded that the enhanced irradiance received by the tracking system has little effect on the mismatch losses. A possible explanation for this is the toolbox limitation to add spectral composition to the direct irradiance, which is expected to influence the mismatch losses. This will be further explained in the following section.

The second insight emerges when examining the fixed and the tracking systems independently and not in relation to each other. At first, for the fixed system, it is noticed that a greater current mismatch value

corresponds to a smaller power mismatch, a trend valid for all climates. The same trend is mirrored in the tracking system. This behavior is justified by the fill factor gain effect. To realize this, consider the I-V curve of two sub-cells and the tandem cell shown in Appendix C.5. When the two cells are current unmatched, the cell with the lower current determines the current in the tandem, resulting in a steeper I-V curve for the tandem in comparison to that of current-matching cells. A stepper curve implies a shapest knee, which in turn is translated to an increase in the fill factor. A higher fill factor enhances the power conversion efficiency and, thus, reduces the power mismatch losses. In practice, this means that an elevated current mismatch of 8.29 % for a tracking system in Bombay for instance, leads to a much lower power mismatch of 1.37%, because is mitigated by the fill factor gain. These findings are nicely aligned with the results of Blom et al. [75], and reinforce the suggestion of their work that the current mismatch overestimates the mismatch losses, and power mismatch should be used instead.

4.6 Comparison with the SHJ modules annual energy gain

In the last section, the annual performance of the tracking tandem modules is compared with that of the tracking SHJ modules. The single junction silicon cell corresponds to the same silicon bottom cell used in the tandem structure described by Al-Ashouri et al. [65]. The layer structure and electrical specifications of the silicon cell are provided in Table 4.7.

Table 4.7: Single junction silicon cell specifications

(a) Layers structure

Layer	**Thickness (m)**
AF2400	0.093
Porous glass ARC	0.053
Glass with low iron (Fe2O3)	3200
Polyolefin-UVT	450
ITO	0.063
n-SiOx (n)	0.02
a-Si(i)	0.009
c-Si, bulk n-type	160
a-Si (i)	0.006
a-Si (p)	0.012
AZO	0.055
Ag	0.3

(b) Electrical characteristics per active area at STC

Parameter (STC)	**Value**
Maximum power P_{MPP}	226.13 W/m^2
Maximum voltage V_{MPP}	0.63 V
Maximum current density J_{MPP}	358.64 A/m^2
Efficiency	22.6%
Module area	1.89 m^2
Number of cells	72

The cell is a monofacial crystalline silicon cell that is textured on both the front and rear sides. It is worth stating once again that both the SHJ cell and the PST simulated cells are monofacial since the employed view factor model is not suitable for bifacial cells.

Figure 4.11 displays the performance of SHJ modules for all locations, while in Table 4.8, the gains are compared. Furthermore, note that for a given location, the hourly optimal orientations are the same for both SHJ and tandem modules throughout the year.

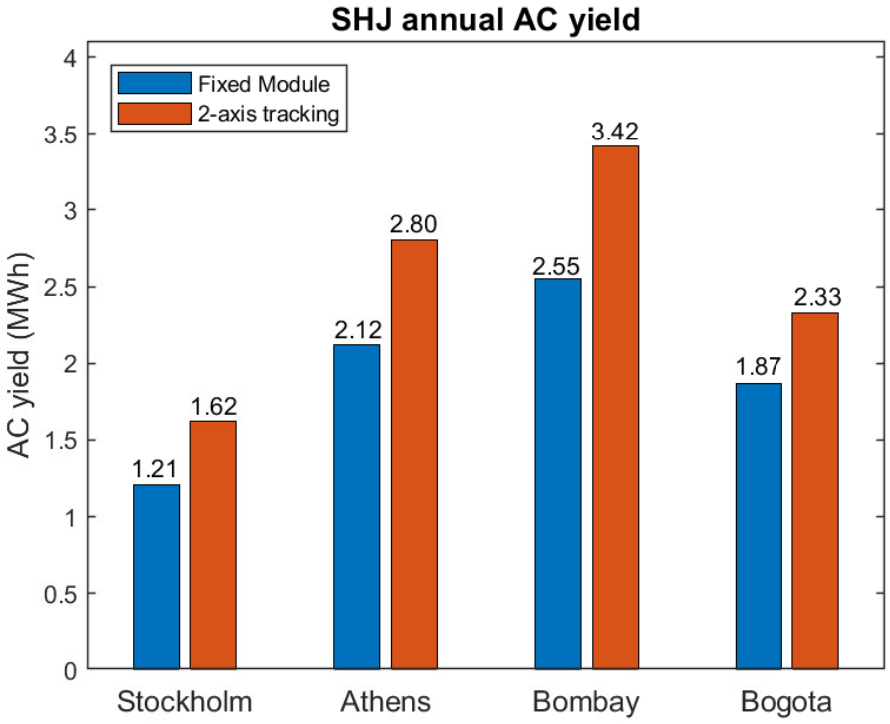

Figure 4.11: Annual AC yield for a SHJ module in the four locations

Table 4.8: SHJ and 2T tandem relative AC gain

Location	SHJ gain (%)	2T tandem gain (%)
Stockholm	33.2	34.0
Athens	31.2	31.9
Bombay	33.5	34.1
Bogota	24.5	24.8

First, when examining Figure 4.11 alongside Figure 4.7 and comparing the locations one by one, it becomes clear that the PST modules consistently produce higher yields than the SHJ in both configurations. Specifically, tandem modules yield 35-38% and 35-39% more than the SHJ modules in tracking and fixed topology, respectively. The better performance of tandem modules is well-known to the scientific community [11, 42] and is also validated here. A notable insight in this study is that across all four locations, the relative AC gain in tracking systems is very similar for SHJ and tandem cells, as Table 4.8 illustrates. A potential reasoning for this outcome will be attempted through comparison with literature.

As pinpointed in Section 1.4, and to the best of author's knowledge, the only comparable simulation found, is the work of Horantner and Snaith [42]. In their work, the relative energy gain between SHJ and 2T tandem tracking structures varied 2-6% depending on the location. The divergence in findings between the two works can traced back to the method the toolbox employs to compute the spectral composition of the irradiance incident on the module.

As explained in Section 1.5.2, the toolbox does not differentiate between the DNI and DHI spectrum composition and treats each sky element with the same spectral composition. To support this statement, in Figure 4.12, the spectral composition of the annual absorbed irradiation for the fixed and tracking topology is given. This graph is generated by summing the irradiance absorbed by the module at each wavelength, for every hour.

As the graph reveals, the tracking system absorbs significantly more than the static system for most of the wavelengths. Nonetheless, it is observed that they both have the same spectral composition per wavelength. Contrary to the toolbox's approach, in reality, diffused and direct irradiance have different spectra as the interactions with the atmosphere affect each component [76] differently. Of course, their spectra will depend on the sky conditions at each time instance. An example of these spectra can be seen in Appendix D. Clearly, the tracking PV system will receive substantially more direct light over the year, since it is designed to follow

the sun. That implies that the spectral composition of absorbed irradiance will differ considerably from the fixed module.

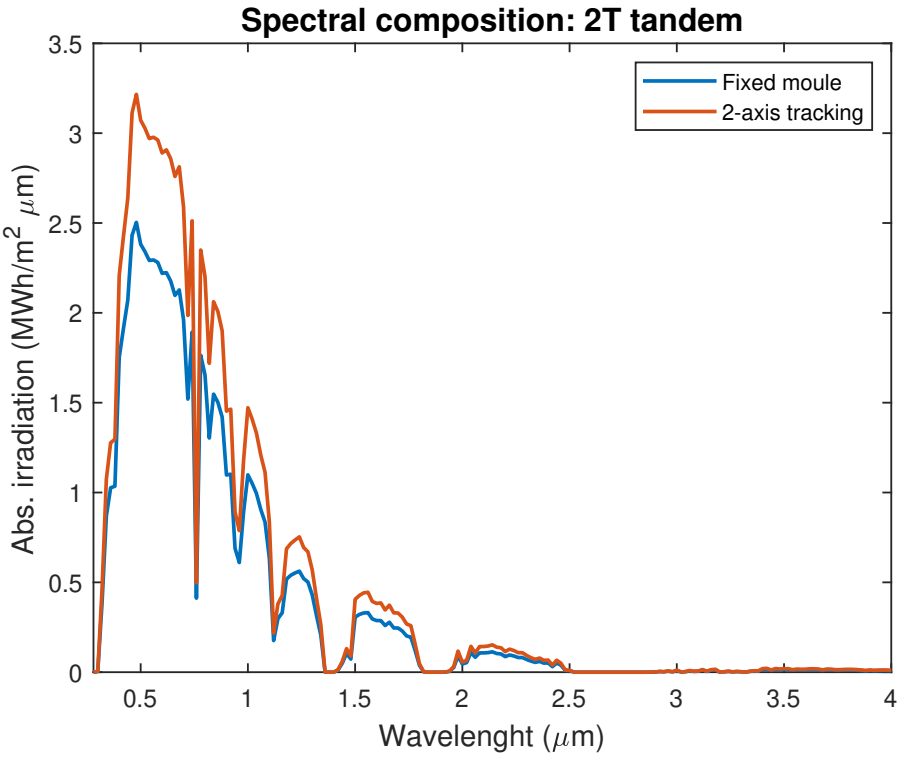

Figure 4.12: Annual spectral composition of the absorbed irradiance for a 2T tandem module in Athens (example location).

Horantner and Snaith did consider different spectral compositions for the DNI and DHI components in their calculations. The limitation of the toolbox not to distinguish the two spectrums, probably explains why the annual AC gain is very similar for tandems and SHJ modules. Ultimately, this can also be the reason why tracking in tandems does not lead to a greater current and power mismatch, as outlined in Section 4.5.4.

4.7 Conclusion

In this chapter, the dual-axis tracking model was employed to simulate tandem cells under real-world conditions, thereby answering the third sub-objective. The hourly sky conditions determine the module tilt angle changes with the module shifted upwards, close to the sun altitude when DNI dominates and being pushed down when DHI prevails. Adjusting the module positions on a daily basis can yield up to 49.7% more energy. On a broader time-scale, the seasonal analysis showed considerable energy gain fluctuations across various locations, influenced by the solar path variations in these locations. Annual results revealed an energy gain of 24.8% for Bogota and similar gains for Stockholm, Athens, and Bombay from 31.9% to 34.1%. Through all locations considered, the irradiance, DC yield, and AC yield relative gains showed a ratio of roughly 1:1:1. In terms of mismatch losses, it was found that solar tracking has no significant effect on current and power mismatch. Lastly, the annual performance of the tandem modules was compared to that of a SHJ module. With respect to relative gain, both technologies demonstrated similar values across all locations. This was attributed to the toolbox's inability to add spectral composition to the direct light component.

Chapter 5

Conclusions and Recommendations

In this final chapter, the important findings on the methods and results of this study are summarized, while conclusions are drawn in relation to the initially established thesis objectives. Subsequently, recommendations are made to guide future studies and enrich the existing work.

5.1 Conclusions

This work aimed to fulfill the following main research objective as described in Section 1.6.2:

Optimize solar tracking strategy for maximum energy yield production of monofacial tandem modules

In order to deal with this main objective, three sub-objectives were defined. Chapters 2 to 4 were each tasked with the realization of a specific sub-objective. The reflection, on whether the chapters addressed the designated sub-objectives is provided in the following sections.

1st sub-objective: Developing a method for faster determination of absorbed irradiance

The time-consuming nature of the ray-tracing method, applied in irradiance calculation, makes the toolbox impractical to support a solar tracking model. Chapter 2 proposed a faster alternative approach, thereby fulfilling the first sub-objective. The new approach presented a different way to express sensitivity values, based on a view factor model. The view factor sensitivity S_{VF} comprises two terms: one related to direct/diffuse irradiance and the other associated with reflected irradiance. Input parameters to calculate the S_{VF} are the EQE of the tandem cell and AOI between each sky element and the surface normal. In total, the S_{VF} is expressed as a function of 5 parameters: the vertex number, the cell layer, wavelength, azimuth, and tilt of the module.

The sensitivity values obtained from the view factor model and ray tracing were compared with respect to computational time and the extent of their agreement. To better define the term "faster" approach, a time goal of 1s was set for sensitivity values of a single orientation. It was found that the view factor model generates sensitivity values at 0.1s on average, while ray-tracing takes over 12 minutes. This result showed that the view factor significantly outperforms ray tracing, yet remains below the set time limit. To compare the respective values, the RMSE metric was used. At first, the difference in sensitivity values across vertices was examined for a specific module orientation. The error for the majority of vertices is concentrated to considerably low values (below 0.1), while only few vertices exhibit higher deviations, the so-called, outlying vertices. To quantify the total error from a single orientation, the mean RMSE of all vertices was used. When increasing the module tilt and albedo values, the mean error is increased. This trend can be attributed to the different assumptions used by the two methods. Primarily, because of the consideration of surrounding modules by the ray tracing method, a factor neglected by the view factor model. For the range of albedo and tilt angles tested, the mean error did not exceed the maximum allowable value of 0.1, indicating that the view factor model generates values closely aligned with ray tracing, especially for lower tilts and albedo values. Therefore, the view factor approach stands as a viable alternative to irradiance calculation, that can be integrated into a solar tracking model.

2nd sub-objective: Finding the optimum algorithm that maximizes the absorbed irradiance

The optimization problem formulated in Section 3.1, aims to find the module orientation that maximizes the absorbed irradiance. The second sub-objective of this thesis is to determine the optimum algorithm(s) that

solve this optimization problem. The sky conditions present on each hour form optimizations case studies with different characteristics: the sunny, intermediate, and overcast hours. These conditions influence the ease of achieving convergence using optimization algorithms. Two types of algorithms were explored for the three cases: Matlab's pre-existing algorithms and an author-developed algorithm.

First, a qualitative comparison of Matlab's built-in solvers was made. Algorithms such as fminsearch, pattern search, and simulated annealing showed dependency on convergence from the initial guess and could not handle integer design variables. On the contrary, surrogate optimization was found to converge to the global optimum, prompting further investigation. Second, a custom-made algorithm called the cross method was developed for this particular problem. Surrogate and cross-method were compared across the three optimization case studies. While the cross method terminates fast (below 0.2s), deviations from the global optimum, especially during overcast hours, cannot be ignored. In addition, the surrogate consistently locates the global optimum at the cost of increased computational time (0.8 - 1.1s). When extending the comparison over an annual simulation period, the same trade-off between speed and accuracy was observed. In light of the above, a hybrid approach was decided (cross method - sunny hours, surrogate - intermediate & overcast hours) as a compromise between accuracy and time. With this justified selection of algorithms, the second sub-objective was achieved. These algorithms were then integrated into a tracking control strategy, which also accounted for the tracker's energy consumption.

3rd sub-objective: Energy yield simulations of tracking tandem PV modules at real-world conditions

After the dual-axis tracking model was built, simulations were performed to examine the behavior of tandem modules mounted on it. Results presented in Chapter 4, fulfilled this goal. Four different climates were selected, representing a variety of operating real-world operating conditions: Stockholm, Athens, Bombay, and Bogota. The analysis was performed in three time frames.

Results on a daily period revealed that the module's tilt adapts dynamically to sky conditions: elevating nearly to the sun's zenith when DNI dominates, and lowering when DHI is prevalent. An important insight is the more prominent role of the DNI in optimal orientation, since a modest DNI presence surges the module upwards, even when DHI is substantially higher. Furthermore, the daily AC yield for a fixed and tracking system was compared on a sunny day. The tracking system proved to outperform the fixed system, notably during the morning and afternoon hours, but equally performed at noon. The daily energy gain for a tracking system ranges from 35.2% to 49.7% for the chosen locations.

The seasonal analysis of energy gain showed substantial fluctuations across the locations, notably dictated by the seasonal variability in solar paths. Cities such as Stockholm, located at a high altitude, demonstrated the highest seasonal changes in energy gain between 19-36.9%. Conversely, cities closer to the equator like Bogota, showed gains ranging narrowly from 21.5% to 28.0%. On an annual basis, the dual-axis tracking system produces 24.8-34.1% more energy than its static counterpart. Bogota exhibits the smallest annual gain of 24.8%, whereas Stockholm, Athens, and Bombay have similar gains above 30%, indicating that there is no straightforward correlation between latitude and relative gain for these locations.

Additionally, important operational parameters were examined. Tracking the sun increased the cell temperature by 1.6-3.2°, due to enhanced absorbed irradiance. An important insight of this study is that the tracking system demonstrated a direct proportionality in gains from absorbed irradiance to DC and AC yields, thereby achieving a 1:1:1 ratio. Compared with bifacial tandem cells, solar tracking proved more efficient in terms of uniform energy harvesting for absorbed irradiance to AC yield. Additionally, the effect of tracking technology in tandem cell mismatch losses was explored. The analysis underscored that tracking has little impact on either the current or the power mismatch.

Finally, the annual energy gain of tandem modules was compared to that of SHJ modules. Although, in absolute terms, tandem modules display superior performance, the relative gain was found to be almost the same across all locations. This finding is attributed to the toolbox's constraint in distinguishing the spectral composition of diffuse and direct light.

5.2 Recommendations

As research is a continuously evolving process, there is always room for improvement. In this section, recommendations are made to improve this work's limitations or to extend its applications. For clarity, since

a lot have been discussed so far, suggestions are made at first for the toolbox itself, then for the methodology followed (chapters 2 & 3), and finally for the performed simulations.

5.2.1 The PVMD Toolbox

Irradiance calculation method: As discussed in Section 1.5, the current version of the toolbox constructs the spectral composition of the irradiance by employing the SMARTS model [54]. This model utilizes the sun's position to compute the air mass for any given time and, based on this, approximates the composition of the incoming spectrum. By doing so, SMARTS considers the direct and diffuse irradiance to be the same. In reality, diffused and direct irradiance have different spectra, dependent on the weather conditions [77]. As a result, SMARTS might not capture spectral differences among sky elements.

In addition, an important limitation of the SMARTS model, is that it does not consider cloud coverage. A more sophisticated model should be used, such as the SBDART model [78]. The latter can handle a variety of sky conditions, including clear and cloudy skies. Given that in Section 4.3.1, we proved the great influence of sky conditions in determining the optimal orientation, the incorporation of the SBDART model into the toolbox is crucial. Besides, SBDART accounts for more factors that greatly influence the spectral composition, such as multiple scattering by cloud droplets, aerosols, ground reflectance, etc, rendering the irradiance calculation more accurate.

Toolbox expansion: With the purpose of making the toolbox commercial, more features can be added. One option is the modeling of energy storage, e.g., via batteries, to simulate stand-alone PV systems. Alternatively, energy demand data can be introduced in the toolbox to simulate, at first, the energy flows of a household powered by a small residential PV system. Another option is to include a model that simulates floating bifacial PV panels that is developed by G. Etxebarria and has yet to be integrated into the toolbox [79].

5.2.2 The designed model

Suggestions for the developed model are divided into its two sub-models: the view factor and the optimization model.

View factor model

Finer $GenPro_4$ angle resolution: When calculating the view factor sensitivity, the EQE curves are extracted from $GenPro_4$ at the closest angle to AOI_D / AOI_R (Equation 2.12). This is because $GenPro_4$ returns EQE curves at preset 30 angular intervals, which may not align precisely with the AOI_D / AOI_R values. A refinement for more accurate sensitivity values is to increase the angular intervals to 60 or 90 so that the AOI of the extracted EQE and AOI_D / AOI_R match closer.

Improved sensitivity of reflected irradiance: One of the limitations of the proposed view factor model is an increase in error with rising albedo values. This is primarily attributed to the simplicity of modeling the reflected irradiance sensitivity. The specular reflection assumed here requires smooth ground surfaces that are often not present in field applications. A more fitting approach is to model the reflected irradiance using diffuse reflectance models, such as Lambertian or Oren-Nayar reflection models [80], that more realistically simulate reflection from rough surfaces. Another suggestion is to account for the self-shading of the modules. Finally, it is recommended to use a wavelength-dependent albedo for a given ground surface, instead of a constant user-defined value.

Bifacial view factor model: Another constraint of the view factor model is that it can exclusively simulate monofacial cells. Future work may focus on expanding this model to include rear-side sensitivity. Thereby, the toolbox can model the joint effect of bifacial tandem cells and tracking technologies, on energy yield prediction. This improvement would provide valuable insights into the tandem cells' ability to boost yield production [43].

Individual cell sensitivity: Lastly, an upgrade to the designed view factor model would be to include individual cell sensitivity. Although that will require a substantial redesign of the current model, it will enable the study of shadowing of specific cells (due to surroundings objects) coupled with tracking. Moving forward, the next step is to refine the view factor model to facilitate non-periodic solar tracking simulations.

Optimization model

Algorithms improvements: The solvers chosen in this work were a combination of surrogate optimization and the cross method. For the hourly-based optimization problems, one of the two was selected based on the optimization case study in which each hour is classified. In fact, it is recommended that the cross method will be further developed to be sufficient as a stand-alone solution for all optimization case studies. There are numerous ways to improve this algorithm. One option is to search in the diagonal points so that the searching pattern will look like a star than a cross and a multiple intermediates positions will be skipped enabling faster convergence. Additionally, the starting point of the method can be improved, since the initial guess equal to the optimum of the last hour can be misleading when there are considerably different sky conditions even between two hours. It is proposed that before the start of the optimum search, a coarse grid of points (azimuth-tilt pairs) is selected (e.g. 10 values for azimuth 10 for tilt, 100 points in total). in which the absorption is determined. Then, the point with the maximum absorption is chosen as the initial guess and the iterative process starts. Thereby, it is expected that the algorithm will take the shortest route to detect the global optimum.

The challenge with the cross method emerges in overcast hours where the gradient path is not distinct in the azimuth direction as explained in Section 3.2.2. In this case, irradiance is evenly spread across azimuth, while the maximum lies in lower tilts. To overcome this, a suggestion is to commence optimizations from multiple starting points (selected on low tilts) in parallel that may end up in local maxima. Then, the global maximum can be identified as the greatest among the local maxima. Another idea is to detect at first the optimum tilt with the normal algorithm procedure and then force the algorithm to perform an azimuth exploration at regular intervals e.g. per 10° on the same tilt, in order to find the optimum across these intervals. Mind that determining the exact optimum azimuth during overcast hours is of minor importance for the absorbed irradiance, but is significant for avoiding unnecessary module movements. Locating the exact optimum will lower the tracker's consumption.

Algorithm switching criterion In Section 3.4, the criterion for switching algorithm was set between sunny hours on one side and intermediate plus overcast hours on the other. This determines which optimization method should be applied in each case. It was based on observations of the convergence ability of the solvers with respect to DNI, DHI ratios. A refinement would be to initially introduce a metric that accurately determines the sky clearness and then use it to characterize the hours in the three categories mentioned above. Afterwards, this metric can serve as a better switching creation for the two cases. It is expected that the implementation of the SBDART model will solve this problem.

Modelling the trackers: As discussed earlier, the tracker modeling was a simplified approach that served the scope of this work. Ideally, more considerations should be taken to quantify its consumption. For instance, the motor's delivered power is not constant. When it begins to move, the power is high to overcome the panel's inertia. While it moves, the power stabilizes and subsequently diminishes as the motor prepares to halt [81]. Additionally, load effects can be considered, such as wind resistance. To better quantify the tracker consumption, the voltage and current output of the motors should be determined via more complex modeling attempt, every time the tracker operates. In experimental tracking panels, this is achieved via a measurement setup [82].

Tracking mechanisms can add a significant cost to PV investment expenditures. To assess the economic viability of tracking tandem PV systems, a financial analysis can be conducted. An effective way is to calculate the Levelized Cost of Electricity (LCOE), including the tracking mechanisms in capital expenditures. The outcome will show whether the enhanced production of tracking systems will offset the high initial cost of trackers, especially in a well-promising technology such as tandem modules. Furthermore, it will address the question of which approach is more advantageous for enhancing the energy yield, from LCOE point of view: integrating tracking systems with a set number of modules or simply adding more modules without tracking.

In this study, a tracking mechanism was employed for each module. Clearly, implementing this approach in a PV farm, the investment cost will rise considerably. A feasible alternative is to apply multi-point drive tracking systems. In these systems, the orientation of PV modules on a string or the entire farm is controlled simultaneously, using driving forces that transmit the motion to all modules [83]. This coordinated movement is subject to centralized control. From a financial point of view, this solution is more cost-efficient. It reduces the number of components needed such as light sensors, drivers, controllers, and most notably motors, which typically account for the greatest cost of the overall mechanism. Specifically, in the case study at hand, where simulations are periodic (all modules receive equal irradiance), the optimal orientation is the same for all modules, and thus the central multi-drive tracker is an advantageous choice. Such mechanisms

are commercially available for single-axis tracking systems [84], but to the best of the author's knowledge, have yet to be realized for dual-axis tracking.

Time interval of optimization problems: The optimization problems of this work were solved on an hourly basis. The time interval was naturally designated by the toolbox design, as it is built to operate with hourly data sourced from Meteonorm. Nevertheless, an hourly-optimized irradiance is less realistic for tracking systems, since sky conditions are subject to changes on much smaller time resolutions, such as 20 or 10-minute intervals. An improvement to the proposed model would be to optimize the irradiance for a time scale of 10 minutes. This adjustment better captures the rapid change in irradiance profile over time. Certainly, this modification necessitates weather data at 10-minute intervals and would inevitably increase the computational time for the annual simulation. However, the expected result is a more precise prediction of the energy yield.

Optimizing the power output: The strategy for solar tracking followed at hand, aimed to find the optimum module positioning that maximizes the module's absorbed irradiance. Reasons for choosing this approach were explained in Section 4.5.3. Future improvements on the toolbox, could optimize the DC power output of the modules, as this holds greater significance in the long run. Doing so is a rather programming intensive task due to the complex structure of the toolbox. Nonetheless, implementing this will eliminate unnecessary movements of the panels. Specifically this occurs, when the absorbed irradiance, although small, suggest a panel shift but the produced DC yield in the new position is zero, due to losses in between the energy conversion steps.

5.2.3 The performed simulations

Tandem Cell architectures: This study focused on the effect of solar tracking in 2T perovskite-silicon tandem cells. Future research can shed light on tracking systems under other tandem structures, such as the 4T and 3T cells. Interesting insights can be gained on how the 3T or 4T tandems handle the increased irradiance due to tracking compared to the 2T cells and how this is influences energy output.

Single-axis tracking: This work was limited to the design of a dual-axis tracking mechanism. To make the analysis more comprehensive, single-axis trackers can be explored, for instance, a horizontal single-axis tracker following the east-to-west sun's direction. In this case, the optimization algorithms should be adjusted to one degree of freedom: the module tilt. Applying the surrogate optimizations becomes straightforward here since the design variable would be set to one. The cross method, however, needs suitable modifications for this context. With only one parameter varying, the pattern search instead of a cross becomes a "line search". Starting from a random initial point, the algorithm can explore adjacent points in both directions, moving towards the one with higher irradiance. If neither neighboring point has a higher irradiance, then the maximum is located. The 1D pattern search is depicted in Figure 5.1. Note that the function of absorbed irradiance against the tilt angle has a single maximum that enables this search pattern.

Given the relatively small range of the tilt, both algorithms are expected to converge faster than the dual-axis tracking algorithms. Yet, for single-axis tracking, utilizing just the modified cross method is sufficient to detect the optimum under any sky conditions. This is justified by the simplicity of the optimization problem, when one variable is considered. Ultimately, a comparison of the energy output of the single and dual tracking systems would reveal which system performs better, during specific periods and locations.

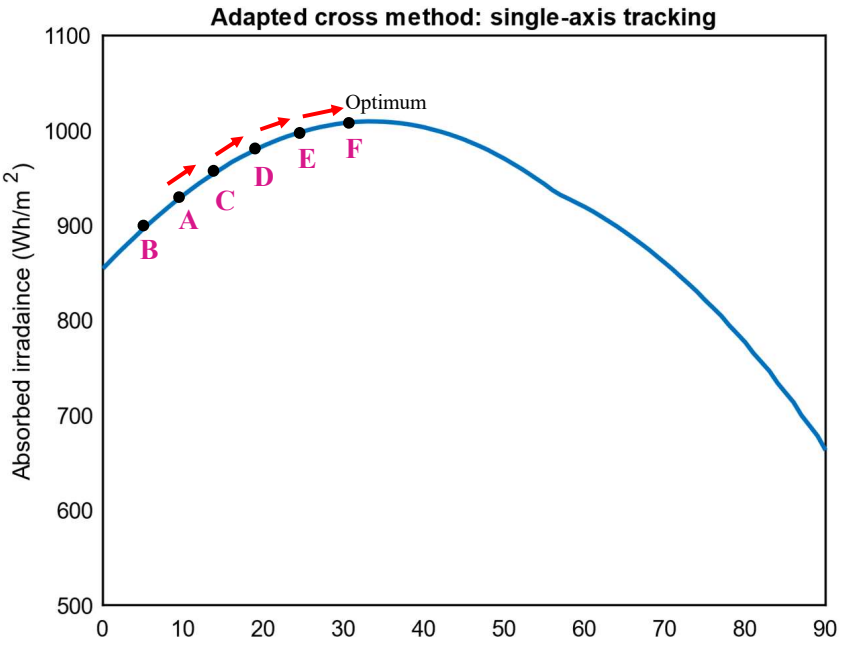

Figure 5.1: Adapted cross method search pattern for single-axis tracking. Starting from point A, the solver checks the adjacent points C and D, then moves to D. The process is repeated, transitioning through points D and E, until it stops at the optimum F.

Annual energy gain-latitude relation: This study could not obtain a clear relationship, between the relative annual gain and the location's latitude. It is expected that this would also be a function of other parameters such as annual DNI, DHI received, or cloud coverage. Further research can be on that made by examining a greater number of locations with various latitudes.

Degradation of tracking PV systems: A study by Piotrowski et al. showed an increased accumulated degradation at the end of the lifetime of a solar tracking module compared to a static topology [85]. A potential cause is that the prolonged exposure to greater amounts of solar irradiation (because of tracking) results in higher operating temperatures, which in turn can reduce the panel's expected performance [86]. Recently, the toolbox has been upgraded with the addition of a degradation model [87]. An interesting research area would be to investigate the impact of tracking topologies on the degradation of PV modules, particularly for tandem structures.

Appendix A

DC Motor Selection

To ensure effective rotation of the solar panel along the desired dimension, the rated power of the DC motor must be sufficient. It is assumed that in the dual-axis tracking system, both rotational axes pass through the center of mass of the panel. Treating the solar module as a rectangular solid body, the moment of inertia can be calculated using the formula:

$$I_{module} = m \cdot \left[\frac{(l^2 + w^2)}{12} \right], \tag{A.1}$$

where l and w represent the length and width of the panel, respectively, and m denotes the mass of the panel along with the mounting structure. Assuming the module rotates with an angular acceleration α_{module}, the torque required to rotate it along one axis can be estimated by the equation below.

$$T_{module} = I_{module} \cdot \alpha_{module} \tag{A.2}$$

Finally, assuming a maximum angular velocity ω is reached, the power requirement is

$$P_{required} = T_{module} \cdot \omega_{module} \tag{A.3}$$

As a result, a DC motor with a rated power output exceeding this power requirement (calculated by Equation A.3) is chosen. In this work, a 25W DC motor is selected for each dimension of movement. To validate that this DC motor can rotate the panel effectively, the power requirement is calculated using the equation above and input values provided in the following table.

Table A.1: Input parameters of the solar module used in toolbox simulations

Parameter	Value
Module length	193 cm
Module width	98 cm
Module area	1.886 m^2
Module weight (incl. mounting structure)	21 kg
Angular velocity	0.3 deg/s
Angular acceleration	0.05 deg/s^2
Power required	19.4 W

The result indicates the chosen DC motor's suitability. Again, it's important to highlight that this is a simplified approach taken considering the scope limitations of this report. In reality, motors require higher torque during start-up to overcome the inertia, which means an increased energy consumption. Moreover, dynamic load variations caused by external factors such as wind forces, snow, or dust are not taken into account.

Appendix B

Global Climate Classsifcation

The Köppen-Geiger-Photovoltaic climate classification map is illustrated below:

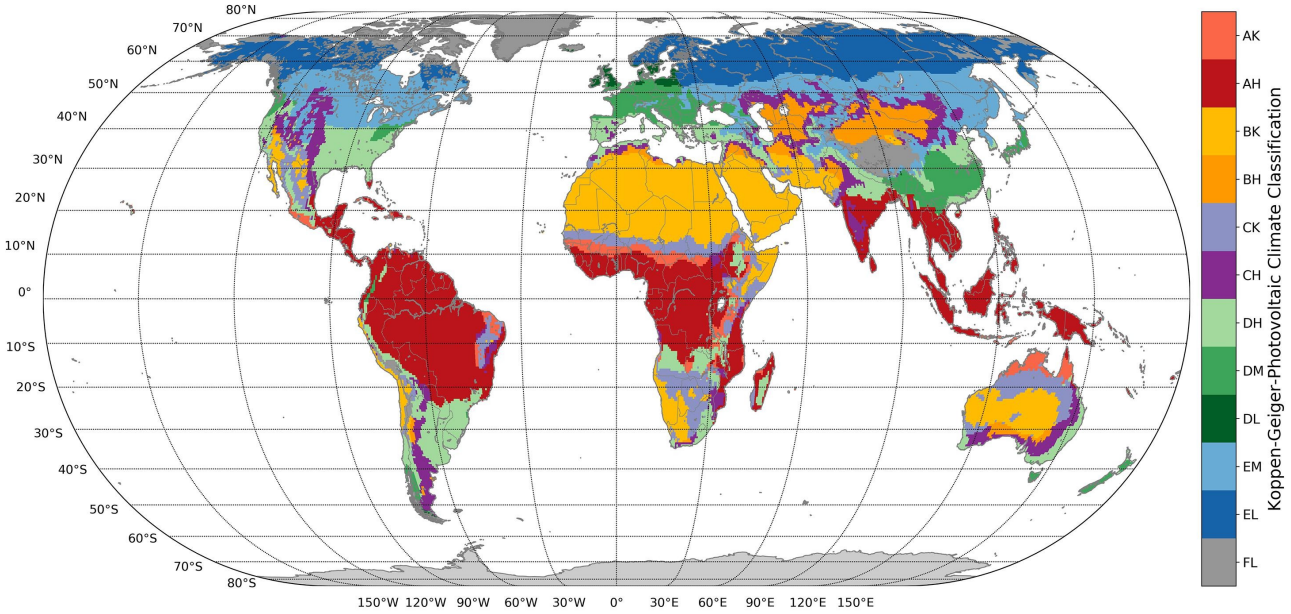

Figure B.1: Climate zone classification map of the KGPV scheme [66].

The colorbar letters indicate the climate zones, where the first letter represents the temperature-Precipitation zones: A-Tropical, B-Desert, C-Steppe, D-Temperate, E-Cold, and F- Polar while the second letter corresponds to the irradiation zones: K-Very High, H-High, M-Medium and L-Low irradiation.

Appendix C

PV system performance

C.1 Daily AC yield results

The daily AC yield of the sunniest days for the four locations is presented in Figure C.1. The same pattern across all locations can be noticed, with the energy gain occurring mainly in the morning and afternoon and dipping to nearly zero at noon. The gains for Stockholm, Athens, Bombay, and Bogota are 49.7%, 41.4%, 44.9%, 35.2%, respectively.

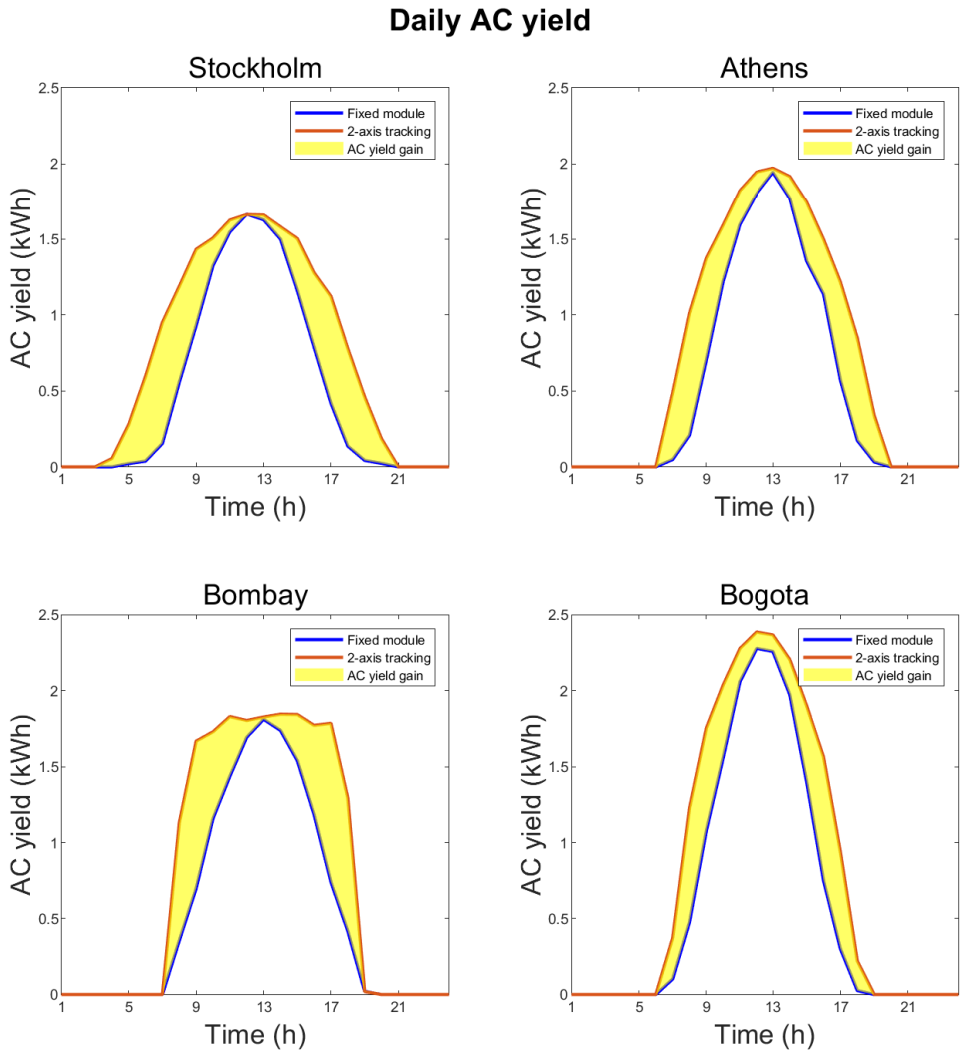

Figure C.1: Comparison of the hourly energy output and gain for the fixed and tracking 2T tandem PV system for the sunniest day in Stockholm (July 10), Athens (May 26), Bombay (May 3), Bogota (April 18).

C.2 Monthly AC yield results

The monthly AC yield gain for the four locations is presented in Figure C.2. The monthly gain variations are 17-40% for Stockholm, 24-39% for Athens, 24-42% for Bombay, and 24-29% for Bogota.

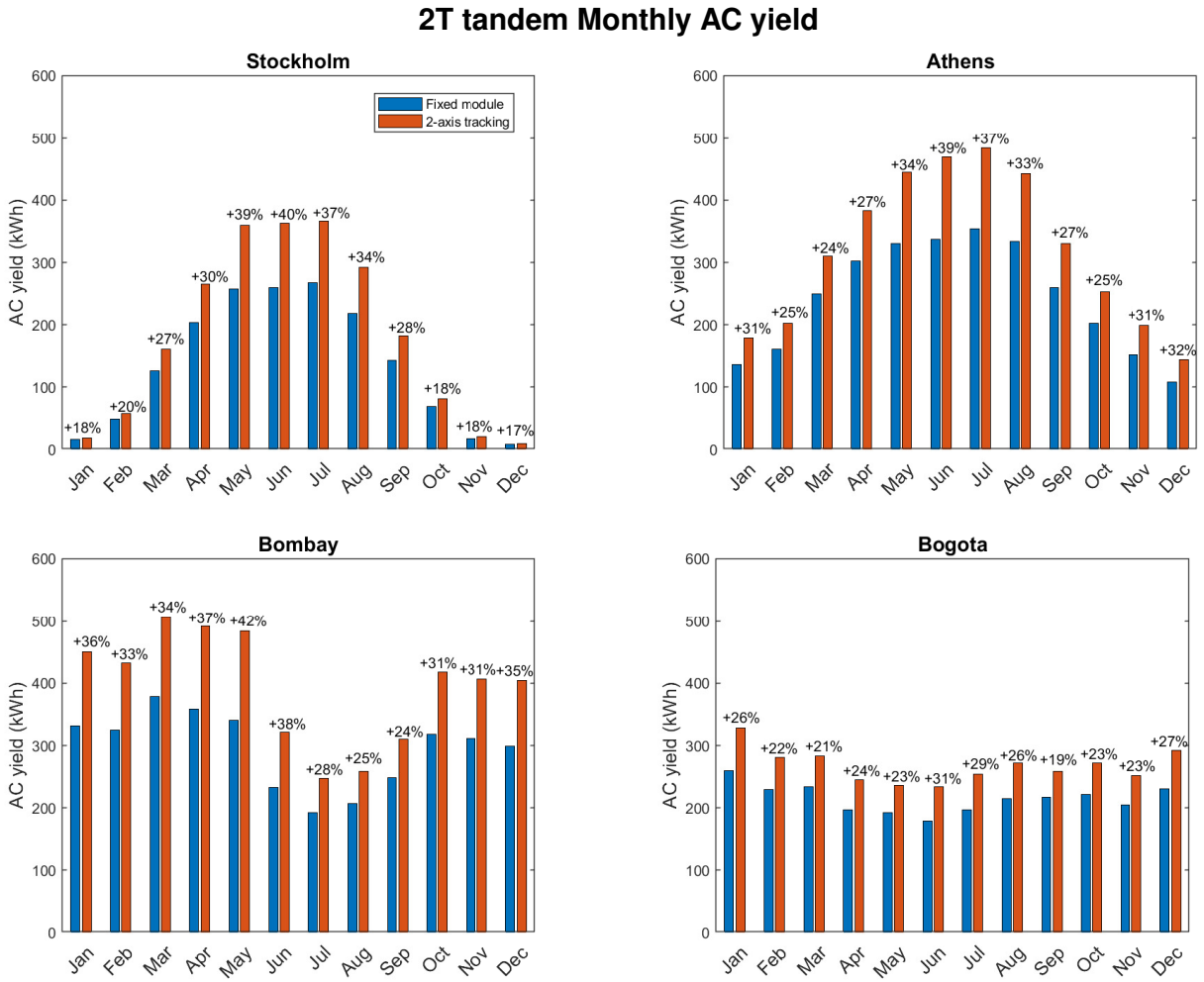

Figure C.2: Monthly AC yield of the 2T tandem PV system in the four locations. The findings of a static and tracking topology are compared. The relative AC gain is depicted on top of the bars

C.3 Energy gain ratio

The energy gain across the steps of energy conversion is shown in Figure C.3. As highlighted in Section 4.5.3 a similar ratio of about 1:1:1 is achieved across all locations.

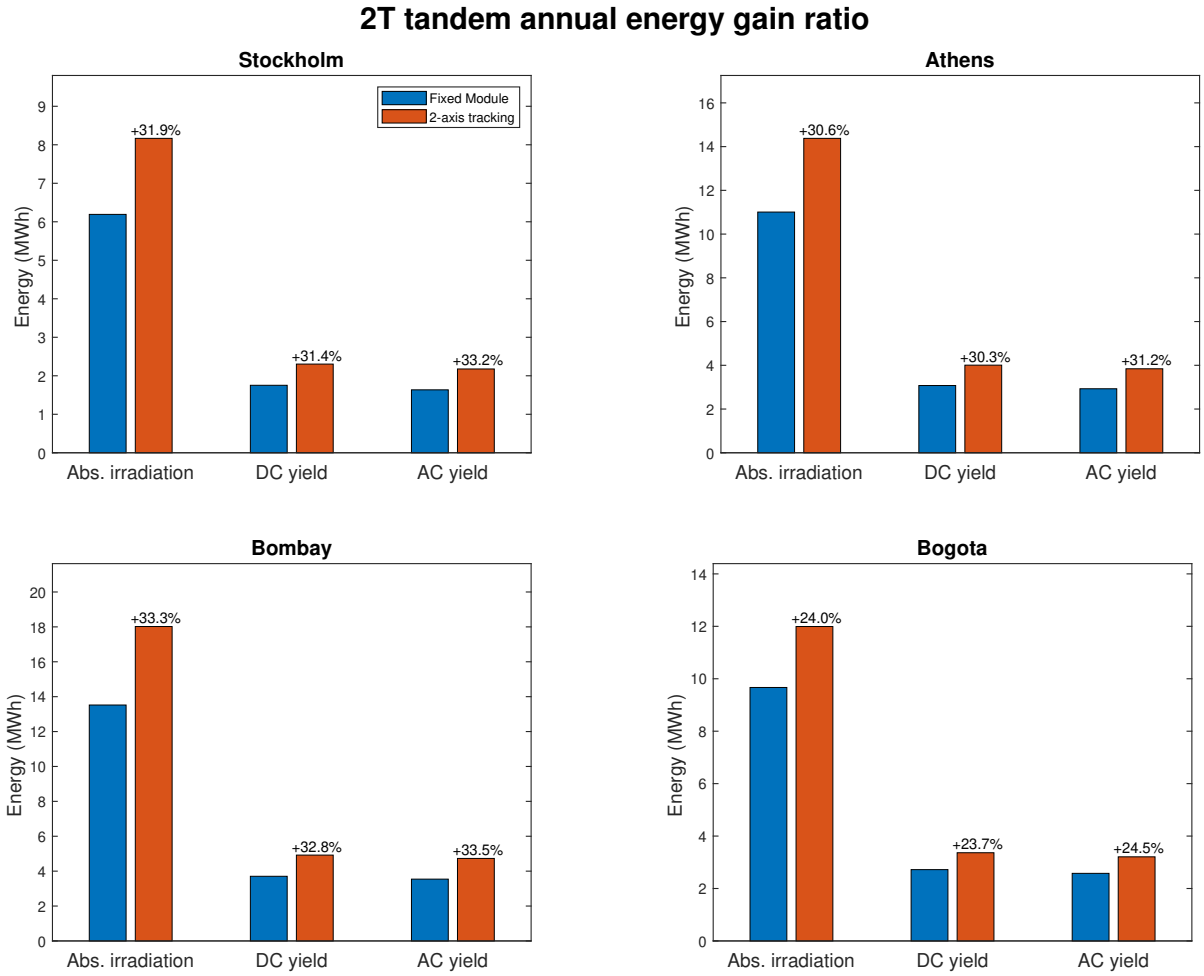

Figure C.3: Energy gain ratio of irradiance-DC yield-AC yield for the tandem tracking PV system

C.4 Hourly optimum tilt angle histogram

For all daylight hours of the year per location, the hourly optimum tilt angles are plotted in a histogram shown in Figure C.4.

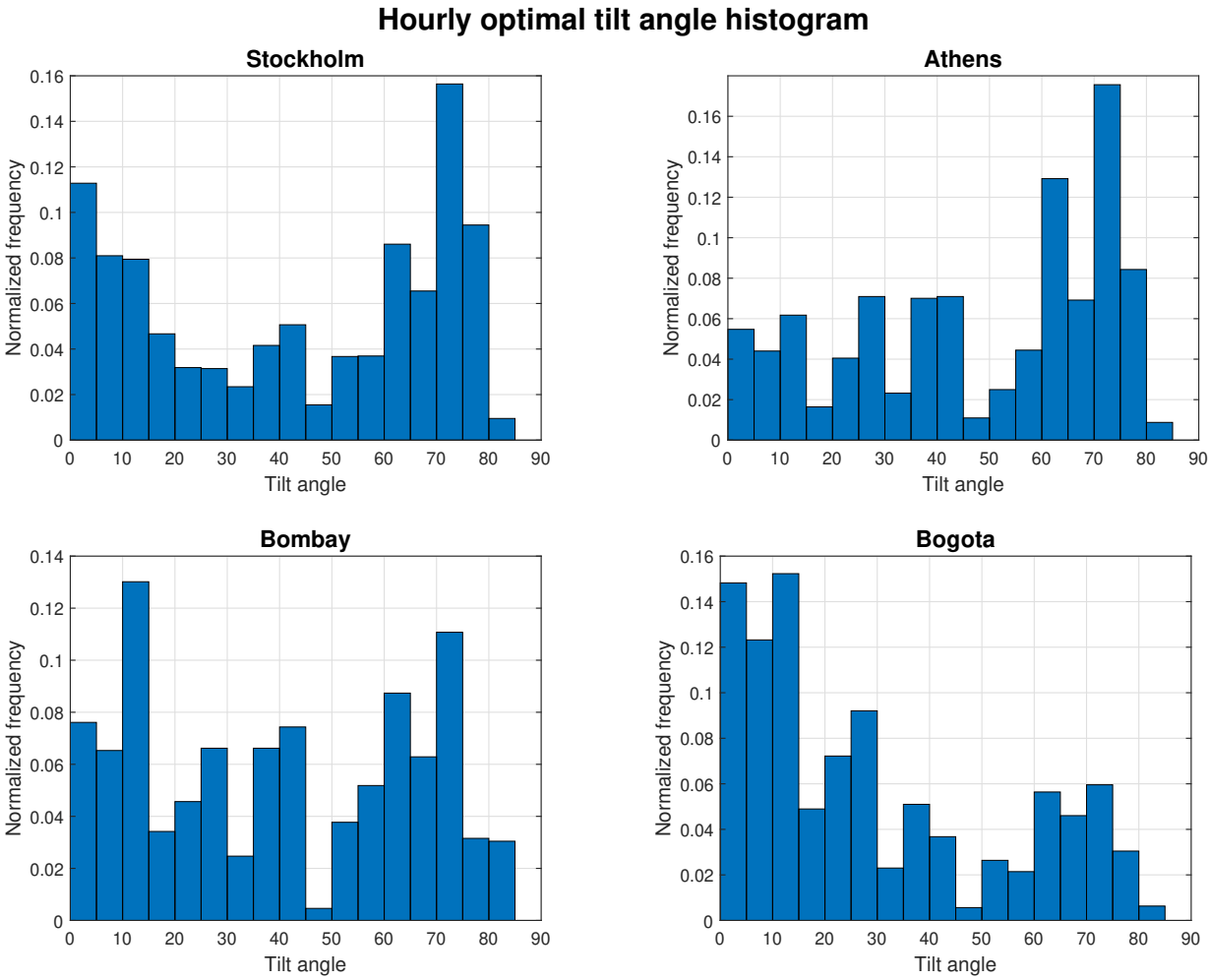

Figure C.4: Optimum tilt angle histogram of the tandem tracking PV system. The bin size is set to 5. Only the daylight hours throughout the year for each location are considered.

C.5 Fill factor gain effect

The figure below explains the fill factor (FF) gain effect. The IV curves of the sub-cells and the tandem cell are shown in Figure C.5a and C.5b. In Figure C.5b, where the current from the two sub-cells is unmatched, the sharpest knee in the tandem cell I-V curve indicates a higher FF compared to the current matching conditions (Figure C.5a). In Figure C.5c, the FF and current mismatch over a day can be seen. At high values of current mismatch over the day, the FF exceeds its STC value (where the current is matched), showing the FF gain. This FF increase leads to a lower loss with regard to power output.

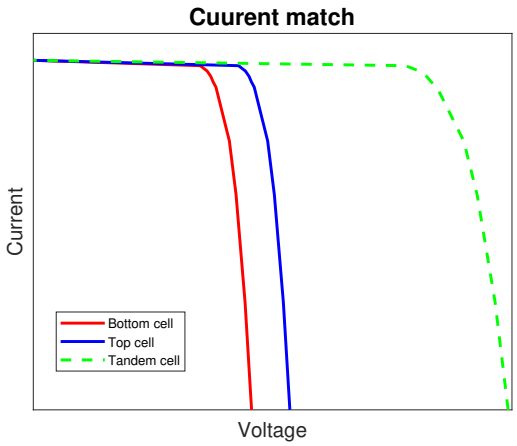

(a) IV curves when current is unmatched

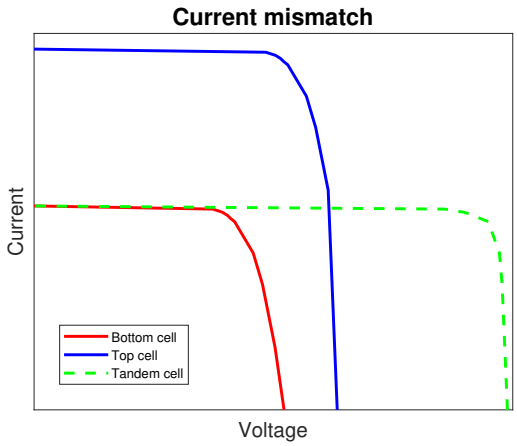

(b) IV curves when current is unmatched

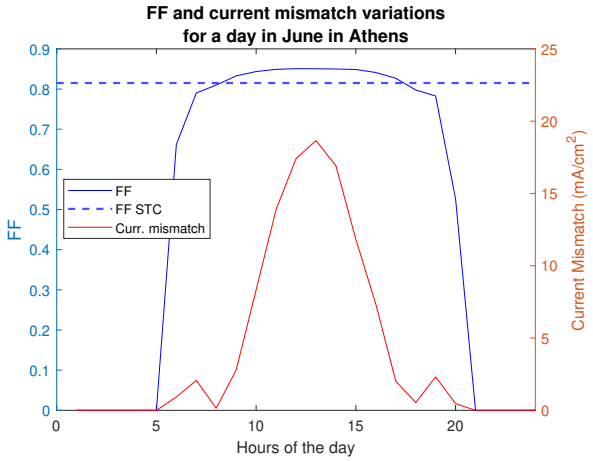

(c) Example of FF gain when there is current mismatch during a day. The horizontal line corresponds to FF at STC when the current is matched.

Figure C.5: The FF gain effect explanation

Appendix D

Spectral Irradiance

For any air mass, the total solar radiation on a surface is the combined amount of beam and diffuse radiations. As shown in Figure D.1 the two components have different spectral compositions.

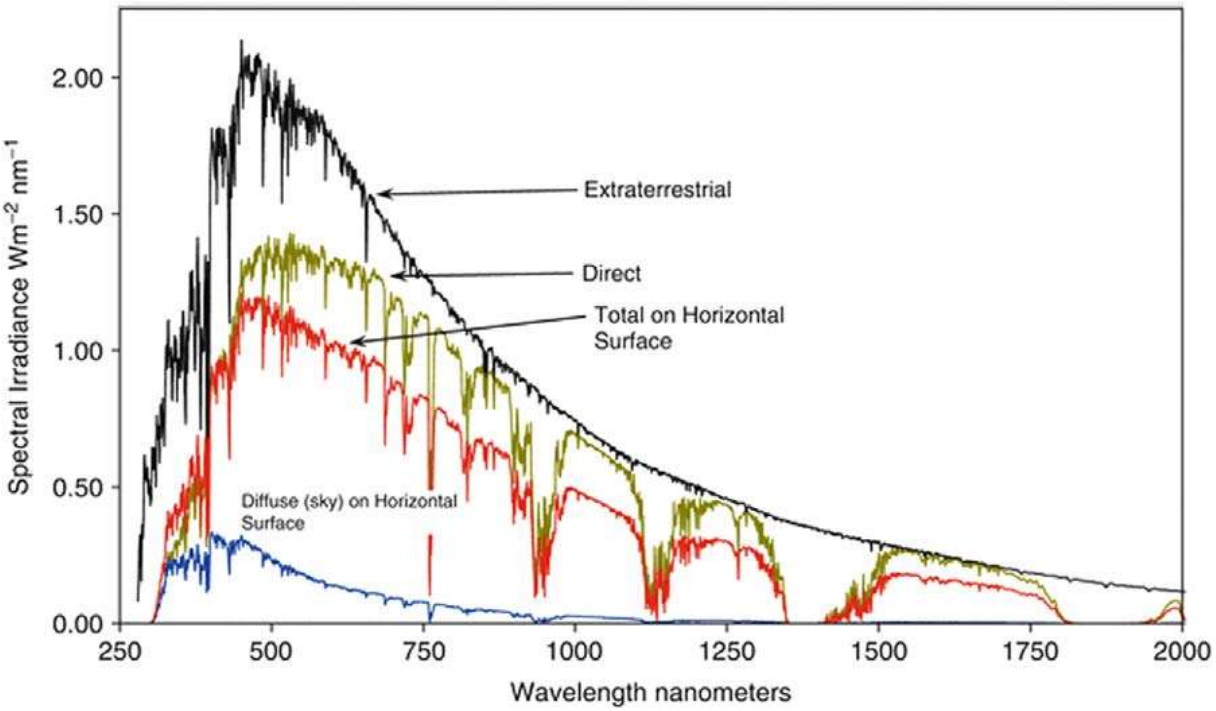

Figure D.1: Spectral distribution of the irradiance components [76].

Bibliography

[1] United Nations Framework Convention on Climate Change (UNFCCC). The paris agreement, 2016. URL https://unfccc.int/sites/default/files/resource/parisagreement_publication.pdf.

[2] U.S. Energy Information Administration (EIA). International energy outlook 2021, 2021. URL https://www.eia.gov/outlooks/ieo/narrative/introduction/sub-topic-01.php.

[3] Chiara Candelise, Mark Winskel, and Robert JK Gross. The dynamics of solar pv costs and prices as a challenge for technology forecasting. *Renewable and Sustainable Energy Reviews*, 26:96–107, 2013.

[4] International Energy Agency Photovoltaic Power Systems Programme . Trends in photovoltaic applications 2022, 2022. URL https://iea-pvps.org/wp-content/uploads/2022/09/PVPS_Trend_Report_2022.pdf.

[5] International Energy Agency . Solar pv, 2022. URL https://www.iea.org/reports/solar-pv#.

[6] NREL. Best research-cell efficiency chart, 2023. URL https://www.nrel.gov/pv/cell-efficiency.html.

[7] Akshay Rao and Richard H Friend. Harnessing singlet exciton fission to break the shockley–queisser limit. *Nature reviews materials*, 2(11):1–12, 2017.

[8] Alexis De Vos. Detailed balance limit of the efficiency of tandem solar cells. *Journal of Physics D: Applied Physics*, 13(5):839, 1980.

[9] Arno HM Smets, Klaus Jäger, Olindo Isabella, René ACMM Swaaij, and Miro Zeman. *Solar Energy: The physics and engineering of photovoltaic conversion, technologies and systems*. UIT Cambridge, 2015.

[10] S Akhil, S Akash, Altaf Pasha, Bhakti Kulkarni, Mohammed Jalalah, Mabkhoot Alsaiari, Farid A Harraz, and R Geetha Balakrishna. Review on perovskite silicon tandem solar cells: Status and prospects 2t, 3t and 4t for real world conditions. *Materials & Design*, 211:110138, 2021.

[11] Marko Jošt, Lukas Kegelmann, Lars Korte, and Steve Albrecht. Monolithic perovskite tandem solar cells: a review of the present status and advanced characterization methods toward 30% efficiency. *Advanced Energy Materials*, 10(26):1904102, 2020.

[12] Jérémie Werner, Bjoern Niesen, and Christophe Ballif. Perovskite/silicon tandem solar cells: marriage of convenience or true love story?–an overview. *Advanced Materials Interfaces*, 5(1):1700731, 2018.

[13] Ehsan Raza and Zubair Ahmad. Review on two-terminal and four-terminal crystalline-silicon/perovskite tandem solar cells; progress, challenges, and future perspectives. *Energy Reports*, 8:5820–5851, 2022.

[14] Olivier Dupré, Bjoern Niesen, Stefaan De Wolf, and Christophe Ballif. Field performance versus standard test condition efficiency of tandem solar cells and the singular case of perovskites/silicon devices. *The journal of physical chemistry letters*, 9(2):446–458, 2018.

[15] Ahmed-Ali Kanoun, Souraya Goumri-Said, and Mohammed Benali Kanoun. Device design for high-efficiency monolithic two-terminal, four-terminal mechanically stacked, and four-terminal optically coupled perovskite-silicon tandem solar cells. *International Journal of Energy Research*, 45(7):10538–10545, 2021.

[16] Masafumi Yamaguchi, Kan-Hua Lee, Kenji Araki, and Nobuaki Kojima. A review of recent progress in heterogeneous silicon tandem solar cells. *Journal of Physics D: Applied Physics*, 51(13):133002, 2018.

[17] Michael Rienäcker, Emily L Warren, Manuel Schnabel, Henning Schulte-Huxel, Raphael Niepelt, Rolf Brendel, Pauls Stradins, Adele C Tamboli, and Robby Peibst. Back-contacted bottom cells with three terminals: Maximizing power extraction from current-mismatched tandem cells. *Progress in Photovoltaics: Research and Applications*, 27(5):410–423, 2019.

[18] Michael Rienäcker, Emily L Warren, Manuel Schnabel, Henning Schulte-Huxel, Raphael Niepelt, Rolf Brendel, Pauls Stradins, Adele C Tamboli, and Robby Peibst. Back-contacted bottom cells with three terminals: Maximizing power extraction from current-mismatched tandem cells. *Progress in Photovoltaics: Research and Applications*, 27(5):410–423, 2019.

[19] Rudi Santbergen, Hisashi Uzu, Kenji Yamamoto, and Miro Zeman. Optimization of three-terminal perovskite/silicon tandem solar cells. *IEEE Journal of Photovoltaics*, 9(2):446–451, 2019.

[20] Fabrizio Gota, Malte Langenhorst, Raphael Schmager, Jonathan Lehr, and Ulrich W Paetzold. Energy yield advantages of three-terminal perovskite-silicon tandem photovoltaics. *Joule*, 4(11):2387–2403, 2020.

[21] Suneetha Racharla and K Rajan. Solar tracking system–a review. *International journal of sustainable engineering*, 10(2):72–81, 2017.

[22] Kok-Keong Chong and Chee-Woon Wong. General formula for on-axis sun-tracking system. *Solar Collectors and Panels, Theory and Applications*, 444, 2010.

[23] Anshul Awasthi, Akash Kumar Shukla, Murali Manohar SR, Chandrakant Dondariya, KN Shukla, Deepak Porwal, and Geetam Richhariya. Review on sun tracking technology in solar pv system. *Energy Reports*, 6:392–405, 2020.

[24] C Chang. Tracking solar collection technologies for solar heating and cooling systems. In *Advances in solar heating and cooling*, pages 81–93. Elsevier, 2016.

[25] Aurélio Gouvêa Melo, Delly Oliveira Filho, Maury Martins Oliveira Junior, Sérgio Zolnier, and Aristides Ribeiro. Development of a closed and open loop solar tracker technology. *Acta Scientiarum. Technology*, 39(2):177–183, 2017.

[26] Vladislav Poulek. New low cost solar tracker. *Solar energy materials and solar cells*, 33(3):287–291, 1994.

[27] Shashwati Ray and Abhishek Kumar Tripathi. Design and development of tilted single axis and azimuth-altitude dual axis solar tracking systems. In *2016 IEEE 1st International Conference on Power Electronics, Intelligent Control and Energy Systems (ICPEICES)*, pages 1–6. IEEE, 2016.

[28] AZ Hafez, AM Yousef, and NM Harag. Solar tracking systems: Technologies and trackers drive types–a review. *Renewable and Sustainable Energy Reviews*, 91:754–782, 2018.

[29] Sebastijan Seme, Bojan Štumberger, Miralem Hadžiselimović, and Klemen Sredenšek. Solar photovoltaic tracking systems for electricity generation: A review. *Energies*, 13(16):4224, 2020.

[30] George Cristian Lazaroiu, Michela Longo, Mariacristina Roscia, and Mario Pagano. Comparative analysis of fixed and sun tracking low power pv systems considering energy consumption. *Energy Conversion and Management*, 92:143–148, 2015.

[31] Emmanuel Karabo Mpodi, Zeundjua Tjiparuro, and Oduetse Matsebe. Review of dual axis solar tracking and development of its functional model. *Procedia Manufacturing*, 35:580–588, 2019.

[32] Rajesh Singh, Suresh Kumar, Anita Gehlot, and Rupendra Pachauri. An imperative role of sun trackers in photovoltaic technology: A review. *Renewable and Sustainable Energy Reviews*, 82:3263–3278, 2018.

[33] Suneetha Racharla and K Rajan. Solar tracking system–a review. *International journal of sustainable engineering*, 10(2):72–81, 2017.

[34] International Energy Agency. *Special Report on Solar PV Global Supply Chains*. OECD Publishing, 2022. URL `https://www.iea.org/reports/solar-pv-global-supply-chains`.

[35] Azhar M Ghazali and Abdul Malek Abdul Rahman. The performance of three different solar panels for solar electricity applying solar tracking device under the malaysian climate condition. *Energy and environment Research*, 2(1):235, 2012.

[36] SA Sharaf Eldin, MS Abd-Elhady, and HA Kandil. Feasibility of solar tracking systems for pv panels in hot and cold regions. *Renewable Energy*, 85:228–233, 2016.

[37] JCAY Rizk and Y Chaiko. Solar tracking system: more efficient use of solar panels. *World Academy of Science, Engineering and Technology*, 41(2008):313–315, 2008.

[38] Thomas Huld, Marcel Šúri, and Ewan D Dunlop. Comparison of potential solar electricity output from fixed-inclined and two-axis tracking photovoltaic modules in europe. *Progress in photovoltaics: Research and Applications*, 16(1):47–59, 2008.

[39] Benjamin Lipovšek, Marko Jošt, Špela Tomšič, and Marko Topič. Energy yield of perovskite solar cells: Influence of location, orientation, and external light management. *Solar Energy Materials and Solar Cells*, 234:111421, 2022.

[40] Marc Steiner and Gerald Siefer. Translation of outdoor tandem pv module i–v measurements to a stc power rating. *Progress in Photovoltaics: Research and Applications*, 2023.

[41] Ramez Hosseinian Ahangharnejhad, Adam B Phillips, Ilke Celik, Zhaoning Song, Yanfa Yan, and Michael J Heben. Cost analysis of thin film tandem solar cells using real world energy yield modelling. In *2019 IEEE 46th Photovoltaic Specialists Conference (PVSC)*, pages 1260–1263. IEEE, 2019.

[42] Maximilian T Hörantner and Henry J Snaith. Predicting and optimising the energy yield of perovskite-on-silicon tandem solar cells under real world conditions. *Energy & Environmental Science*, 10(9):1983–1993, 2017.

[43] Maxime Babics, Michele De Bastiani, Ahmed Hesham Balawi, Esma Ugur, Erkan Aydin, Anand S Subbiah, Jiang Liu, Lujia Xu, Randi Azmi, Thomas G Allen, et al. Unleashing the full power of perovskite/silicon tandem modules with solar trackers. *ACS Energy Letters*, 7(5):1604–1610, 2022.

[44] Mermoud Andre and Wittmer Bruno. Pvsyst user's manual, 2014. URL `https://d3pcsg2wjq9izr.cloudfront.net/files/73830/download/660275/100.pdf`.

[45] Youri Blom. Energy loss analysis of tandem pv modules under realistic operating conditions, 2022. URL `https://repository.tudelft.nl/islandora/object/uuid:92c54633-57d0-4aee-9a53-794159484500`.

[46] Rudi Santbergen, Tomomi Meguro, Takashi Suezaki, Gensuke Koizumi, Kenji Yamamoto, and Miro Zeman. Genpro4 optical model for solar cell simulation and its application to multijunction solar cells. *IEEE journal of photovoltaics*, 7(3):919–926, 2017.

[47] Robert Siegel. Net radiation method for transmission through partially transparent plates. *Solar Energy*, 15(3):273–276, 1973.

[48] R Santbergen, VA Muthukumar, RME Valckenborg, WJA van de Wall, AHM Smets, and M Zeman. Calculation of irradiance distribution on pv modules by combining sky and sensitivity maps. *Solar Energy*, 150:49–54, 2017.

[49] MR Vogt, C Ruiz Tobon, A Alcaniz, P Procel, Y Blom, A Nour El Din, T Stark, Z Wang, E Garcia Goma, JG Etxebarria, et al. Introducing a comprehensive physics-based modelling framework for tandem and other pv systems. *Solar Energy Materials and Solar Cells*, 247:111944, 2022.

[50] Zeman, Miro and van den Heuvel, Joost and Pieters, BE and Kroon, M and Willemen, J. Asa opto-electronic simulator for amorphous and crystalline semiconductor devices. user's manual 6.0, 2019. URL `https://asa.ewi.tudelft.nl/storage/asa_manual.pdf`.

[51] Meteonorm. Meteonorm software worldwide irradiation data, 2021. URL `https://meteonorm.com/en/`.

[52] Richard Perez, Robert Seals, and Joseph Michalsky. All-weather model for sky luminance distribution—preliminary configuration and validation. *Solar energy*, 50(3):235–245, 1993.

[53] Garcia Goma E. Development of cell to system annual energy yield toolbox for bi-facial modules, 2018. URL `https://repository.tudelft.nl/islandora/object/uuid%3A255ac731-b59b-453a-b899-1ff5dec1add2?collection=education`.

[54] Christian A Gueymard. Parameterized transmittance model for direct beam and circumsolar spectral irradiance. *Solar Energy*, 71(5):325–346, 2001.

[55] Martin K Fuentes. A simplified thermal model for flat-plate photovoltaic arrays. Technical report, Sandia National Labs., Albuquerque, NM (USA), 1987.

[56] Amit Jain and Avinashi Kapoor. Exact analytical solutions of the parameters of real solar cells using lambert w-function. *Solar Energy Materials and Solar Cells*, 81(2):269–277, 2004.

[57] William Earl Boyson, Gary M Galbraith, David L King, and Sigifredo Gonzalez. Performance model for grid-connected photovoltaic inverters. 9 2007. doi: 10.2172/920449. URL `https://www.osti.gov/biblio/920449`.

[58] Tim Stark. Modeling and monitoring of a floating photovoltaic pilot system, 2020. URL `https://repository.tudelft.nl/islandora/object/uuid:8a04400d-8e96-46f4-a048-769d954674d4`.

[59] Calcabrini Andres, Cardose Ruben, Gribnau David, Babal Pavel, Manganiello Patrizio, Zeman Miro, and Isabella Olindo. Time-varying, ray tracing irradiance simulation approach for photovoltaic systems in complex scenarios with decoupled geometry, optical properties and illumination conditions. *Progress in Photovoltaics: research and applications*, 31(2):134–148, 2023.

[60] MHM Sidek, N Azis, WZW Hasan, MZA Ab Kadir, S Shafie, and MAM Radzi. Automated positioning dual-axis solar tracking system with precision elevation and azimuth angle control. *Energy*, 124:160–170, 2017.

[61] MathWorks. Global optimization toolbox user's guide, 2023. URL `https://nl.mathworks.com/help/pdf_doc/gads/gads.pdf`.

[62] H-M Gutmann. A radial basis function method for global optimization. *Journal of global optimization*, 19 (3):201–227, 2001.

[63] Kok-Keong Chong and Chee-Woon Wong. *General formula for on-axis sun-tracking system*, chapter 13, page 282. Sciyo London, UK, 2010.

[64] Yizhu Guo, Wei Liu, Jianzhong Cha, and Yaobin Tian. A system modeling method for optimization of a single axis solar tracker. In *2010 International Conference on Computer Application and System Modeling (ICCASM 2010)*, volume 11, pages V11–30. IEEE, 2010.

[65] Amran Al-Ashouri, Eike Köhnen, Bor Li, Artiom Magomedov, Hannes Hempel, Pietro Caprioglio, José A Márquez, Anna Belen Morales Vilches, Ernestas Kasparavicius, Joel A Smith, et al. Monolithic perovskite/silicon tandem solar cell with >29% efficiency by enhanced hole extraction. *Science*, 370(6522): 1300–1309, 2020.

[66] Julián Ascencio-Vásquez, Kristijan Brecl, and Marko Topič. Methodology of köppen-geiger-photovoltaic climate classification and implications to worldwide mapping of pv system performance. *Solar Energy*, 191:672–685, 2019.

[67] Matti Tukiainen. Sunrise, sunset, dawn and dusk times around the world, 2023. URL `https://tandempv.conexio-pse.de/program/daily-program`.

[68] Solargis, ESMAP, World Bank Group. Global solar atlas, 2023. URL `hhttps://globalsolaratlas.info/map`.

[69] Saqaff A Alkaff, Nikesh H Shamdasania, Go Yun Ii, and Vinod Kumar Venkiteswaran. A study on implementation of pv tracking for sites proximate and away from the equator. *Process Integration and Optimization for Sustainability*, 3:375–382, 2019.

[70] Arian Bahrami, Chiemeka Onyeka Okoye, and Ugur Atikol. The effect of latitude on the performance of different solar trackers in europe and africa. *Applied energy*, 177:896–906, 2016.

[71] Arian Bahrami and Chiemeka Onyeka Okoye. The performance and ranking pattern of pv systems incorporated with solar trackers in the northern hemisphere. *Renewable and Sustainable Energy Reviews*, 97:138–151, 2018.

[72] Ibrahim Khalil Almadani, Ibrahim Sufian Osman, Nasir Ghazi Hariri, Muhammad Saleem, and Nagmeldeen AM Hassanain. Investigating the effects of solar tracking systems on thermal profile of photovoltaic modules. *International Journal of Renewable Energy Research (IJRER)*, 11(4):1561–1569, 2021.

[73] Y. Blom, C. M. Ruiz Tobon, M. R. Vogt, R. Santbergen, O. Isabella. Detailed comparison of loss distribution in mono- and bifacial 2t perovskite/silicon tandem pv systems. TandemPV workshop 2023, Chambery, France, 2023. URL `https://tandempv.conexio-pse.de/program/daily-program`.

[74] Eike Köhnen, Marko Jošt, Anna Belen Morales-Vilches, Philipp Tockhorn, Amran Al-Ashouri, Bart Macco, Lukas Kegelmann, Lars Korte, Bernd Rech, Rutger Schlatmann, et al. Highly efficient monolithic perovskite silicon tandem solar cells: analyzing the influence of current mismatch on device performance. *Sustainable Energy & Fuels*, 3(8):1995–2005, 2019.

[75] Youri Blom, Malte Ruben Vogt, Carlos M Ruiz Tobon, Rudi Santbergen, Miro Zeman, and Olindo Isabella. Energy loss analysis of two-terminal tandem pv systems under realistic operating conditions—revealing the importance of fill factor gains. *Solar RRL*, page 2200579, 2023.

[76] R. Eke, T.R. Betts, and Gottschalg R. Spectral irradiance effects on the outdoor performance of photovoltaic modules. *Renewable and Sustainable Energy Reviews*, 69:429–434, 2017. ISSN 1364-0321. doi: https://doi.org/10.1016/j.rser.2016.10.062. URL `https://www.sciencedirect.com/science/article/pii/S1364032116307079`.

[77] Blaz Kirn and Marko Topic. Diffuse and direct light solar spectra modeling in pv module performance rating. *Solar Energy*, 150:310–316, 2017.

[78] Paul Ricchiazzi, Shiren Yang, Catherine Gautier, and David Sowle. Sbdart: A research and teaching software tool for plane-parallel radiative transfer in the earth's atmosphere. *Bulletin of the American Meteorological Society*, 79(10):2101–2114, 1998.

[79] Garro Etxebarria. Toolbox for the design and simulation of a floating bifacial pv plant with reflectors, 2018. URL `https://repository.tudelft.nl/islandora/object/uuid%3Aa86fd44c-379c-48f8-a737-2c0b01086384?collection=education`.

[80] Lawrence B Wolff, Shree K Nayar, and Michael Oren. Improved diffuse reflection models for computer vision. *International Journal of Computer Vision*, 30:55–71, 1998.

[81] ET El Shenawy, M Kamal, and M Mohamad. Solar tracker modelling. *J. Appl. Sci. Res*, 8(8):3898–3907, 2012.

[82] Salsabila Ahmad, Suhaidi Shafie, and Mohd Zainal Abidin Ab Kadir. Power feasibility of a low power consumption solar tracker. *Procedia Environmental Sciences*, 17:494–502, 2013.

[83] C Alexandru and C Pozna. The optimization of the tracking mechanism used for a group of pv panels. In *International Conference on Renewable Energies and Power Quality, ICREPQ*, volume 9, 2009.

[84] Powerway. Powerway upgrades the multi-point drive tracker — powerfit-blade, 2021. URL `https://pvpowerway.com/news_74/387.html`.

[85] Leonardo Jonas Piotrowski and Felix Alberto Farret. Feasibility of solar tracking and fixed topologies considering the estimated degradation and performance of photovoltaic panels. *Solar Energy Materials and Solar Cells*, 244:111834, 2022.

[86] SA Sharaf Eldin, MS Abd-Elhady, and HA Kandil. Feasibility of solar tracking systems for pv panels in hot and cold regions. *Renewable Energy*, 85:228–233, 2016.

[87] Abhishek Velpuru. Pv lifetime energy yield, 2021. URL `https://repository.tudelft.nl/islandora/object/uuid:72a496a8-b589-4d5b-bf57-dc067624acee?collection=education`.